# Università degli Studi di Napoli *Federico II*

DOTTORATO DI RICERCA IN

**FISICA**

**Ciclo XXXIII**

Coordinatore: prof. Salvatore Capozziello

# Research and development of graphene-based supercapacitors through Graphene Oxide

Settore Scientifico Disciplinare FIS/03

**Dottorando**
Achille Damasco

**Tutore**
Prof. Giancarlo Abbate

Anni 2018/2021

# Acknowledgements

I would like to thank Prof. Giancarlo Abbate, which is not only my supervisor, but also a founder of the start-up and academic spin-off *CapTop*. I tried to learn by his initiative spirit before by his knowledge of Physics and Scientific writing. If he were not a so versatile person, this Ph.D. project would never exist.
I would like to thank all *CapTop* society too. A special thank is for Raffaele Amico, co-founder of CapTop and founder of the high-tech company *O.C.I.M.A.*. *O.C.I.M.A.* hosted me for the industrial aspects of my Ph.D. project, teaching me Amico's belief that "every occasion holds opportunity for a great venture". Amico made available for me the incredible know-how of a team of engineers and technicians of automation, which carry on always-different work at high levels.
In *O.C.I.M.A.* team, I found an important help thanks to Eliana and Giorgio Amico, Antonio Palmiero, Tommaso Fera, Giuseppe Marino, and Benedetto Tedesco. I thank all of them for let me feel the spirit and mentality of working in a great company.
In *CapTop* team, I thank engineers Eugenio Saraceno and Sergio Bassino for their contribution about supercapacitor applications and high power technology; these are fields where I was a novice student. As channel between *CapTop* and the rest of the "world", I acknowledge Dr. Claudio D'Angelo.
I would like to thank Dr. Tao Wu of *S.P.S.* co., for an unforgettable journey to China and a very interesting visit to a leading supercapacitor factory.
I do not know how to thank Prof. Francesco Ruffo, which not only co-founded *CapTop* and guided me in his laboratory of Department of Chemistry, but he was like a second supervisor. He gave me an endless number of tips and instilled me his passion for chemistry. Ruffo's team is like a family, so I am glad to thank also Prof. Maria Elena Cucciolito, Dr. Roberto Esposito (which is actually a professor), PhD student Alfonso Annunziata and researcher Massimo Melchiorre, the green-electrolyte-man and my colleague in the mission for innovative supercapacitors. For helping me even if they did not even remotely be obliged to do it, I thank Dr. Vincenzo Benessere, Valeria Prokopenko, Carmen Scamardella, Rossella Di Guida, Arianna De Stefano, and Caterina Verde. In other words, the "METOR" group (Metal-Organic Chemistry).
A crucial help came from Industrial Chemistry team, so I would like to thank Prof. Martino Di Serio, which is also another *CapTop* co-founder. Then I acknowledge the help of Prof. Rosa Vitiello, of Ph.D. students Francesco Taddeo and Carmelina Rossano, then of Tommaso Cogliano.
Other three chemists gave me crucial help, so I would like to thank them: PhD student Ilaria Stanzione (for the use of the probe sonicator), Prof. Alessandro Vergara (Raman Spectroscopy), and Prof. Prospero Di Pierro (Zeta Potential Analysis).
I am very glad to thank Prof. Carlo Altucci and Ph.D. Manjot Singh: they involved me in a strongly interdisciplinary work (inside Physics, Chemistry, and Biology). I suggest following their progresses.
My period abroad in UK, in the cute city of Bath, had an incalculable importance for me, so I would like to thank Prof. Michele Meo for this opportunity. However, I found in Bath a friendly slice of Italy thanks to Marco, Stefano, Francesco F., Fabrizio, Francesco R., Michele, Giulia, Ivana, Sara,

and in an indescribable way Mario Rapisarda. Mario is a very brilliant Ph.D. student of Chemical Engineering, and I am sure he will have a great career. Moreover, I acknowledge Prof. Frank Marken, Dr. Elena Madrid, and Budi Riza Putra Putra of the Department of Chemistry of the University of Bath for their hospitality and advice. I acknowledge also in the same university Dr. Salman Shahid of the Department of Chemical Engineering for sharing his experiences about carbon and surfactants. Finally, I acknowledge the Material and Chemical Characterisation Facility (MC2) at the University of Bath for technical support and assistance in this work.

Coming back in Italy, I would like to thank *Laminazione Sottile* co., a leader company in the aluminium field. In particular, I acknowledge Dr. Ciro Sinagra (head of R&D section), and Dr. Francesco Bravaccino. They teached me very important subjects of my project: aluminium etching, aluminium coating, and relative binders.

I would like to thank Dr. Alessandro Lampasi and prof. Lorenzo Caputi for their important suggestions to furtherly improve this thesis.

Even if not all the possible lines of research succeed to produce a paper, this does not mean they cannot give me helpful know-how. For this reason, I would like to thank Prof. Eugenio Notomista and Dr. Marialuisa Siepi for their work about carbon nano-tubes with lysozyme, and then I thank Prof. Paola Manini and Dr. Alessandro Pezzella for their work on melanin-based micro-SCs.

Usually the hardest part of a work is its beginning. If it is so, then I would like to thank also Dr. Annalisa Acquesta (Department of Material Engineering of my university), for my first steps about electrochemical analysis; then I acknowledge Dr. Pierpaolo Prosini's team, in particular Annalisa Aurora, for important experiences in the *E.N.E.A.* centre of research in Rome. For helping me to get out of the academic bureaucracy, I thank Michele Scarpati and prof. Vincenzo Canale.

Finally, I would like to thank my parents, my sister, and "my" Sara for being on my side during all my ups and down; then I am very glad to thank a light beam that made happier the darkest year 2020: Giovanni, my son.

# Contents

# List of figures

# Introduction

A *supercapacitor* (SC) or *ultracapacitor* is an energy storage device which stores energy through electrostatic movement of charges as a normal capacitor, but it is called "super-" because overcome the capacitance of a normal one (μF-mF) till to 6-9 orders of magnitude (thousands of Farad). We can give a more rigorous definition only in terms of specific performances, i.e. if we consider capacitance or energy with respect to the mass or volume of a device. All energy storage devices (capacitors, SCs, electrochemical batteries and fuel cells) can be easily described by a plot "Power Density vs Energy Density" called *Ragone plot*, as shown in Figure 1 [1]: SCs are also called *Electrochemical Capacitors* and we can consider in this way every capacitor with energy density above $3 \cdot 10^{-1}$ Wh/kg.

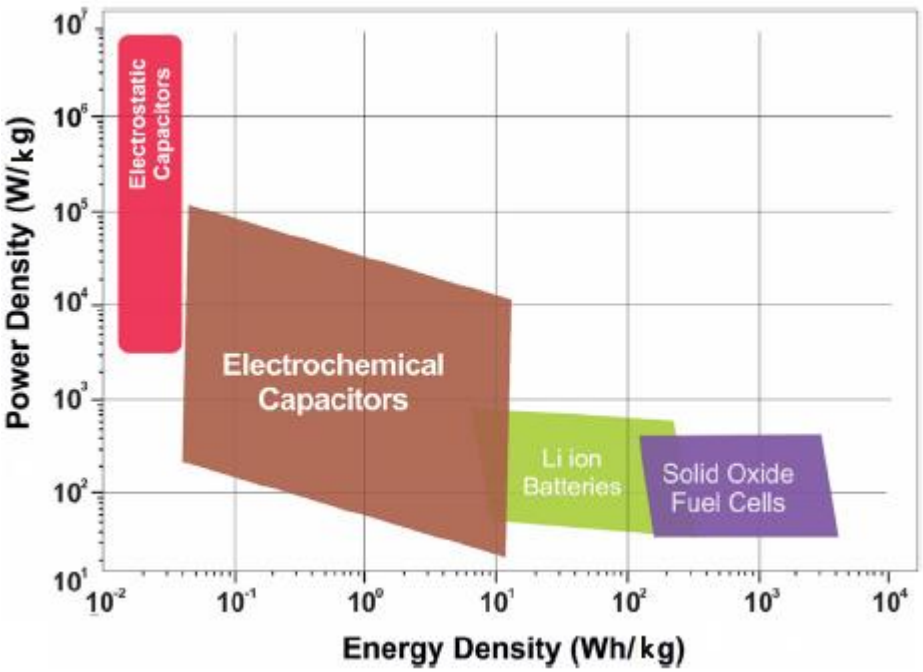


**Figure 1:** Ragone plot of main energy storage devices.

SCs are complementary to the electrochemical batteries: batteries have huge energy density (until 210 Wh/kg) so they are used everywhere in our life (smartphones, laptop computers, cars, remote telecontrols, and so on). Instead, a SC should be 10 times bigger (in mass) to store the same energy of a battery but it can manage 100-1000 times the power (current) of a battery with the same mass. If a battery warms up too much during a charge or discharge, in the same condition SCs carry the same current without detectable effect, so they are used in all devices and machines that need high currents for a short period of time (for example 300 A for 10 s).
For all these reasons SCs belong to a very specific class of applications and in the next future they will probably couple with electrochemical batteries. However, all the lines of research about SC aim

to improve them in term of more energy density, without or with small decrease in power density, to find a new device with the advantages of both batteries and SCs. Other aspects of SC technology can be improved as ecology and scaling up, so this Ph.D. thesis tries to offer a possible path in this sense.

In the first chapter we are going to explain how and in how many ways a SC works and what are the current lines of research about it; this overview is largely based on a chapter, co-authored by myself recently appeared on an Elsevier book [2]. The second chapter deals with a graphene precursor, Graphene Oxide (GO), interesting material not only because it can be transformed in a graphene-like materials, but also because it facilitates almost every manufacturing steps for a SC. Since GO is useful also for biotechnological applications and the analysis techniques are the same of our subject, the second chapter will in part follow a research paper in the biotechnology field, which I published during my Ph.D.-course [3].

The third chapter is about an experimental application of the expertise about GO for a potential new kind of graphene-based SC [4, 5].

# Chapter 1
# State of the art

## 1.1 Multiple purposes

This Ph.D. thesis explains in the first chapter how many possibilities of improvements there are in the research works about SCs. In the fields of Physics, Chemistry and Materials Science, there is simultaneously a wide literature about GO and its applications. GO is studied due to its versatility and workability.
The main subject of our works is the optimization of SCs, due to their features, which we can briefly summarize. SCs are energy storage devices offering excellent performances when charge and/or discharge speeds are crucial [2], so their research is of huge and growing interest. Moreover, SCs can work at low temperatures and carry out many charge and discharge cycles (until 1 million). Examples of SC applications are emergency opening systems in buses and planes, UPS systems, KERS and stop-start technology in cars (especially hybrids), and the partial replacement of batteries in trucks [2]. They also operate in energy intermittence protection systems in wind or solar power generation plants [6, 7], in the energy recovery apparatus of overhead cranes and hoists, in the rail transportation industry [8], and, recently, also in mobile devices, for powerful flashes and Wi-Fi [9, 10].
Before going into the state of the art in this field, we should disclose the importance of a multi-function material, reduced Graphene Oxide (rGO). rGO is a graphene-like material produced from a reduction reaction of GO [11, 12]. The latter is a functionalized graphene sheet having oxygen functional groups such as hydroxyl, carboxyl, or epoxide. These groups disrupt the conjugated network of $sp^2$- hybridized carbon atoms, which is the peculiarity determining the great electronic and thermal properties of pristine graphene [13, 14]. Through the process of reduction, these groups can be stripped away and the hexagonal lattice of carbon atoms can be recovered. For this reason, rGO is a good electrical conductor, even if not fully comparable with pristine graphene [15]. In fact, the removal of the oxygen-containing groups causes topological defects affecting the electrical and thermal properties [16]. There are however different methods to improve the reduction process and to prevent topological defects in the wide literature about rGO [17, 18].
Nowadays, one of the most common ways to obtain graphene-like materials relies on the oxidation of graphite to obtain graphite oxide (GtO) [19, 20]. From GtO, sheets of GO can be produced as intermediates thanks to mechanical exfoliation [13]. Besides, the direct rGO production is possible [21, 22]. In numerous works, the choice of GO arises from its already discussed important advantages. GO is readily soluble in water, and it can be reduced in both physical, providing energy with heat or laser [22, 17], and chemical ways [18]. However, due to the presence of oxygen functionalities, GO is an electric insulator and, therefore, the effectiveness of the reduction process becomes crucial. Otherwise, rGO cannot be used in energy storage devices as SCs.
Since all kinds of commercial or experimental SCs have a high specific power, the main aim of current scientific research focuses on the improvement of the amount of stored energy. Nowadays, such energy is about 1/10 of the energy of a battery with the same mass [23]. Nonetheless, the stored energy is not the only margin of improvement. The manufacturing process and in particular, its cost, scalability, and environmental impact are important to give to new SCs a concrete

impingement on the technological progress. Furthermore, the final weights of the devices may be crucial for applications in the automotive and aerospace fields, as well as in portable electronics. In an SC electrode, the "active material" needs to adhere to a current collector. An active material is a material responsible for electrical charge storage, and it usually consists of porous carbons characterized by a high specific surface area, like activated carbons (AC) and CB powders. A current collector is a material allowing electrical current flow and usually consisting of aluminium (Al) sheets. Active materials adhere on current collectors by use of a binder.

In most cases, especially in commercial SCs, the binder is a glue consisting of polymers such as polytetrafluoroethylene and polyvinylidene fluoride [24, 25]. They both provide good adhesion and electrochemical stability. However, being electrically insulating polymers, present binders also represent a high resistance component in the electrode. In addition, such polymers are expensive and dangerous for the environment. This problem is aggravated by the use of organic solvents, which are required to obtain homogeneous slurries for the coating of current collectors. Organic solvents are in turn expensive and not ecological.

Binders therefore represent a dead mass that is convenient to be reduced. An alternative to common binders is identified in conductive polymers such as polyaniline nanofibers, which can be used to fabricate freestanding electrodes or as a support for carbon nanotubes [26]. Their practical use is however limited by their manufacturing method, the electrospinning. This method is not readily scalable to industrial processes.

In the work of Galhena et al. [27], rGO was adopted as an alternative binder with good results. However, as in other studies [28, 29], the use of toxic and expensive organic solvents was still necessary, especially for the electrical double layer capacitors (EDLCs). EDLC is a type of SC relying only on electrostatic charge storage. An alternative of them are hybrid SCs (HSCs). An HSC is a type of SC consisting of a battery-like Faradaic electrode and an EDLC-like non-Faradaic electrode. In recent works about HSCs, an aqueous electrolyte was used for an rGO-based nanocomposite electrode [30, 31]. For the latter, the Faradaic electrode can be made with a metal−organic or metal−sulfidic nanostructure, while the EDLC electrode can be made with carbon nanotubes evenly distributed in graphene sheets [30, 31]. As the reported HSCs show promising performances, they are valuable for the future of SCs. Moreover, thanks to their hybrid nature, they can also benefit from newly developed electrodes for EDLCs based on rGO, as the aim of this thesis.

# 1.2 Types of supercapacitors

There is a "family tree" for SCs that joins them according to the use of purely electrostatic charge


**Figure 2**: SCs family tree **[32]**.

storage or with a contribution of red-ox chemical reactions or both. They are the Electric Double Layer Capacitors (EDLCs), the pseudocapacitors and hybrid capacitor. From the point of view of a Ragone plot like Figure 1 [33], EDLC are the closest to the normal capacitor zone while the others occupy the side near the batteries. In any case, there is a trade-off between specific energy and specific power. Figure 2 shows the SC family tree with a further subdivision according to the kind of electrode material.

## 1.2.1 EDLC

EDLCs are the most common kind of commercial SCs and the subject of the experimental part of this research. In a normal capacitor, the electrodes are a couple of conductive surfaces (typically metals, as for instance aluminium) with a very simple geometry and a dielectric separator between them. The capacitance *C* is given by equation (1)

$$C = \varepsilon \frac{A}{d} \qquad (1)$$

in which $\varepsilon$ is the dielectric constant of the material between the electrodes, *A* is their area and *d* their distance. In an EDLC the electrodes are made with a highly porous conductive material, so that the surface is the results of a network of inlets (see Figure 3); between the electrodes there is an electrolyte with dielectric constant $\varepsilon$ but also ions that go inside the pores during SC charging and vice versa. In this configuration, the distance *d* is the separation between the charges in the

electrode and the ions near them, as shown in Figure 3 [34]. An EDLC follows in first approximation equation (1) but with a higher $A$ (at least 1000 $m^2/g$) and with a $d$ of the same order of magnitude of an inter-molecular distance (about some Angstroms). For these two reasons, an EDLC can be considered as a SC. Actually, after a charge every EDLC is formed by two couple of capacitors: each capacitor is formed by a sort of layer of charges in the electrode and a layer of ions of the opposite sign near it, and the same happens with opposite signs on the other electrode. Finally, in an EDLC a couple of aluminium sheets are used as current collectors, which the electrodes are glued to, while a dielectric porous separator (usually a sheet of paper) avoids electric contact between the electrodes.

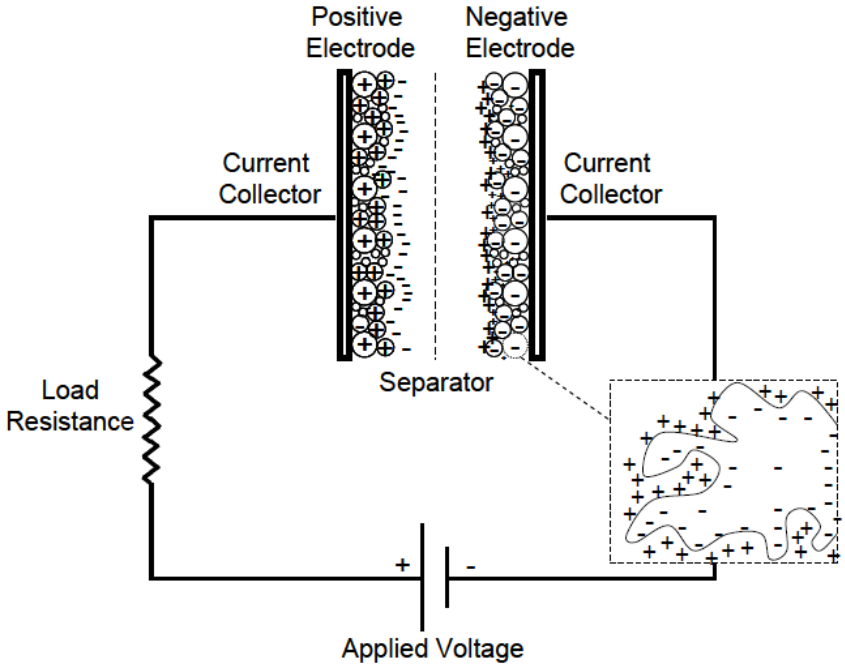


**Figure 3:** Schematic representation of an EDLC in a circuit.

Like in a normal capacitor, there is a maximum value for the allowed applied voltage that depends on the dielectric rigidity of the materials between the electrodes, in this case the electrolyte itself. If this voltage is $V$, the maximum energy stored in a SC, (as in each capacitor) is

$$E = \frac{1}{2}CV^2 \qquad (2)$$

To describe the maximum working power of a SC, we need some schemes. Figure 4 shows models for a SC with a gradual increment of realism [34]. Figure 4.a is the ideal capacitor, 4.b is a capacitor with the internal resistance $R_S$, also called *ESR* (Equivalent Series Resistance). ESR is a term that includes (at least in principle) all the sources of resistance: the current collectors, the binder, the electrodes, the electrolyte, and the entrance of the ions in the pores. In a well-made SC, only the last one is the factor that affects ESR.

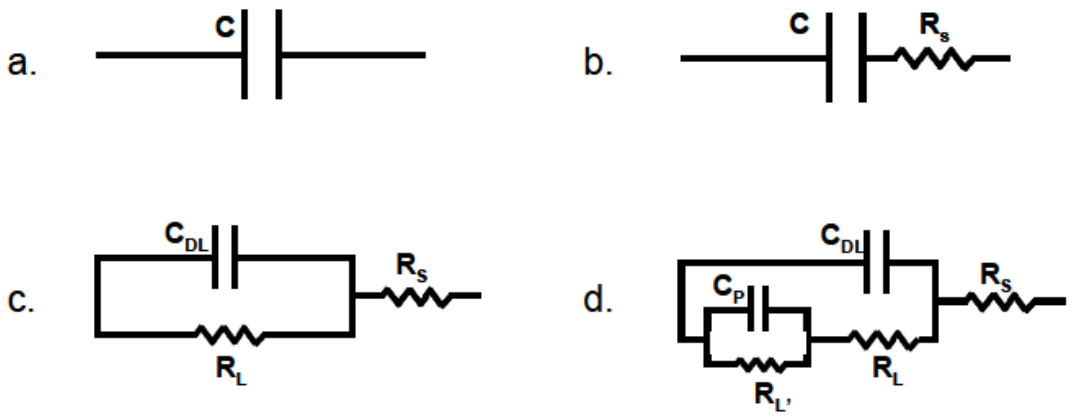


**Figure 4:** Circuital description of a SC with only the capacitance (a), then adding the internal resistance (b), then the leakage resistance (c), and then the effect of the porous nature of the electrodes (d).

Given the ESR and the applied voltage, the maximum power that a SC can emit is

$$P = \frac{V^2}{4 \cdot ESR} \qquad (3)$$

The factor 4 in the denominator has this origin: the maximum power is calculated in the case in which there is a load with the same resistance of the SC, so this power is I·V, where I = V/(2·ESR) (we have two resistors in series, both with resistance equal to ESR),while the voltage on the load is half the voltage on the SC, so (V/2), hence there are two factors 2 in the denominator that make the factor 4 in the (3).

Figure 4.c adds a resistor in parallel to the capacitor with resistance $R_L$ to include the leakage phenomena: a charged SC, in an open circuit, tends to spontaneously lose its charges in a self-discharge. Moreover, charge and discharge are slower than predicted by (3) due to $R_L$. A good SC should have ESR as small as possible and $R_L$ as high as possible. A commercial SC has ESR of the order of mΩ but the self-discharge is faster than in batteries.

In Figure 4.c the capacitance is called $C_{DL}$ because it represents the main contribution for SC capacitance, i.e. the formation of the double layer. Eventually, there is a second contribution due to red-ox reactions in the pores (so, a non-electrostatic charging). This kind of capacitance entails a second circuit in parallel with another leakage resistance and it takes place in the so-called pseudo-capacitors or in EDLCs with unwanted reactions due to impurities.

Summarizing and simplifying, we can improve SC performances by searching an electrode material with higher specific surface (higher *C*) and a new electrolyte that can sustain a higher voltage *V*, according to the (1) and (2). Actually, *C* does not depend only on *A* nor in a linear way by it, while *V* is affected also by the electrode material and not only by the electrolyte. These are typical behaviours of EDLCs that we can notice only if we go beyond the schematisation of a SC as simply a "big capacitor".

The capacitance is not simply proportional to the surface because in an EDLC there are usually three kinds of pores: *micropores* (diameter under 2 nm), *mesopores* (2-50 nm), and *macropores* (over 50 nm). Not all kind of pores are helpful for ions of a certain electrolyte, because if they are too wide the SC will have good power density but low energy density, vice versa for too small pores there is wider specific area (so higher specific capacity) but there is less accessibility in the pores and so a lower power density. This phenomenon is illustrated in Figure 5 [35].

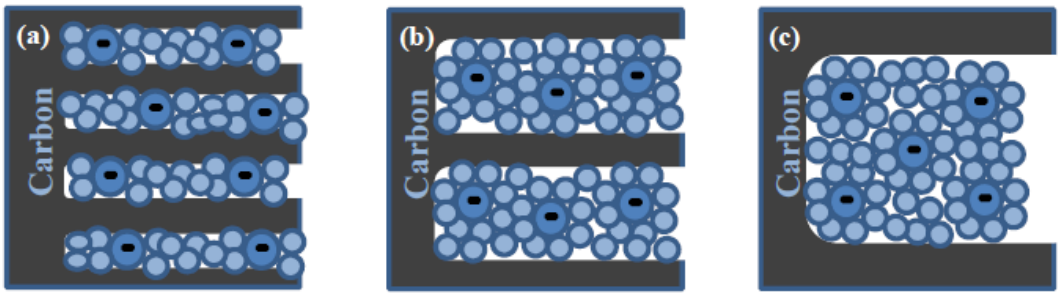


**Figure 5:** Scheme for the pores of an EDLC: they may be (a) too small, (b) fitted or (c) too wide for the ions of the electrolyte.

Figure 5 shows that every ion is surrounded by a solvation sphere made with the solvent molecules, so the ideal electrode should be made with pores slightly larger than ions diameter. Consequently, if an electrode material has huge specific area but it is like in Figure 5.a or 5c, it could not make a capacitance better than a material with lower specific area but fitted pores, so that we should use in the (1) not the total geometric area *A* but only the actual charged area. Moreover, this trade-off between large and small pores is one of the main reasons there is a trade-off between energy density and power density in the lines of research about new SCs.

In the formula (2) voltage *V* depends on the breakdown voltage of the solvent so we can briefly say that it depends on the electrolyte, but we should do an in-depth analysis. When we apply a voltage to a solvent over its breakdown value, it decomposes in other ions as in the case of the water electrolysis: water produces hydride ion and hydroxyl ions. Then the former produces molecular hydrogen near the cathode while the latter forms water and oxygen near the anode. These products of re-dox reactions make the electrodes impure and attack them at every charge-discharge cycle. The electrodes will lose porosity and stability until the SC cannot work. However, at least in principle we can realize an electrode material that can make the time for this breakdown as long as possible during charge-discharge cycles over the maximum voltage. This is the case of a seamless mesoporous carbon sheet consisting of continuous graphene walls [36], which was coupled with a common electrolyte ($Et_3MeNBF_4$ in propylene carbonate or PC): the maximum voltage for PC is 2.5 V, but a SC with this innovative electrode worked till to 4.4 V. This work is however an exception, because researchers prefer to work on new electrolytes that can sustain higher working voltage to realize SCs with very long life cycle or they prefer to make the so-called AEDLC, where the "A" means "asymmetric". This device is an EDLC where the positive electrode is made with more carbon, and the respective capacitor has a larger capacitance than the negative electrode. This is made because some positive ions can sustain, before degradation, a greater voltage than negative ones and the voltage drop distribution across the two capacitors in series is no more symmetric, resulting inversely proportional to the respective capacitances. Eventually, the overall Electrochemical Stability Window (ESW, the maximum voltage that can be applied to a SC) is enlarged, sometimes up to 1 V wider. This phenomenon is depicted in Figure 6 [37], where w+/w- is the mass ratio between the two electrodes, which is proportional to the capacitance ratio.

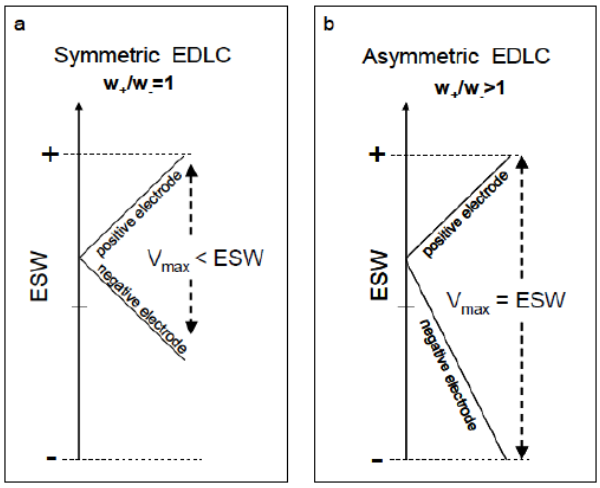


**Figure 6**: Diagram of the potential excursion in the symmetric (a) and asymmetrical configuration (b), where ESW is the Electrochemical Stability Window.

## 1.2.2 Pseudo-capacitors

A pseudo-capacitor is a SC whose charging process occurs thank to reversible red-ox reactions between the electrolyte and the electrode. This kind of charging is called "faradic" (and vice versa, the EDLC is called non-faradic). The main purpose of this kind of SC is to achieve higher specific energy with a contained loss in power performance.

Many reactions are known involving oxides and sulphides of transition metals, such as $RuO_2$, $IrO_2$, $TiS_2$ or their combinations. These reactions are accompanied by electro-adsorption and intercalation processes.

Let us recall what a red-ox reaction consists of. An oxidant (suffix -ox) and a reductant agent (red-) react according to the form $ox + ze^- \leftrightarrow red$.

In addition to a red-ox reaction, an ion adsorption takes place, i.e. accumulation of ions to form a single layer on the electrode substrate. This is a reversible process that results in a faradic charge transfer and gives rise to a pseudo-capacitance, without breaking or forming of chemical bonds.

In Figure 7, we show a comparison between the operating mechanisms of an EDLC and of a pseudo-capacitor [38]. In particular, we can notice the different mechanism of charge separation.

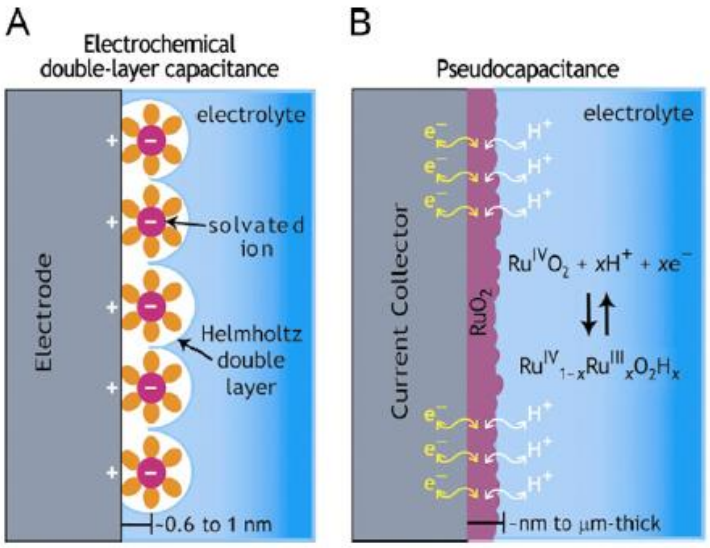


**Figure 7**: Scheme of the charge conservation mechanisms in an (A) EDLC and in a (B) pseudo-capacitor.

The charge transfer process in a pseudo-capacitor is much faster than that of batteries but slower than the double layer forming in EDLC, thus its specific power is less than the EDLC one but still much greater than that of batteries.
On the other side, the specific energy of the pseudo-capacitors is less than the battery one, but much greater than that of the EDLC. Present pseudo-capacitors exhibit specific energy values between 10 and 50 Wh/kg, and specific capacitance between 300 and 1000 F/g [39].
Again, due to its physical working mechanism, intermediate between those of EDLCs (pure electrostatic charge transfer) and of batteries (chemical reactions involving mass transfer at the electrodes) a pseudo-capacitor has intermediate life cycle duration. It can attain a life cycle of the order of 100,000 cycles, which is about 10 times less than that of EDLCs and 100 times greater than that of a battery [40].
Pseudo-capacitors can be made with several types of electrodes, in particular with conducting polymers or metal oxides.
Conducting polymers are one of the main research focuses of modern electrochemistry. Generally, polymers are insulators, but we can make electrochemical reactions occur in double-bond systems, such as polyaniline, polythiophene, and polyacetylene. These reactions can be reversible; thus they can be used in SCs. It is possible to make a conductive polymer thanks to processes called "electrochemical doping of polymers" by anions or cations, in analogy with semiconductors.
Conducting polymers have a relatively high capacitance and conductivity, and a relatively low ESR. Moreover, their cost is comparable to carbon-based materials. The downside is their limited stability limits after many charge and discharge cycles, due to mechanical stress on the conducting polymers during red-ox reactions. Hence, the reduced life cycle with respect to EDLC, as above reported.
Alternative materials for pseudo-capacitors electrodes are metal oxides. Because of their high conductivity, metal oxides have been deeply studied as possible materials for pseudo-capacitor electrodes. The most relevant scientific works concern ruthenium oxide ($RuO_2$), because it shows the highest specific capacitance.
The excellent capacitance of ruthenium oxide (1358 F/g) and its good electrical conductivity ($3 \cdot 10^2$ S/cm) are obtained through the insertion and removal or intercalation of protons in its amorphous structure, according to the following reaction [1]:

$$RuO_2 + xH^+ + xe^- \leftrightarrow RuO_2(OH)_x \qquad (4)$$

where $0 \leq x \leq 2$. In the hydrated form ($RuO_2 \cdot xH_2O$), its capacitance (720 F/g) still exceeds those of carbon-based materials and conductive polymers. In addition, also the ESR of hydrated ruthenium oxide is better performing than that of other electrode materials. Furthermore, in the tubular arrangement of porous structures of $RuO_2 \cdot xH_2O$, an even higher specific capacitance value (1300 F/g) can be achieved [39].
Unfortunately, the success of ruthenium oxide has been limited by its prohibitive costs. A cheaper alternative is represented by manganese oxide ($MnO_2$). It has a theoretical specific capacitance of 1370 F/g, a low cost and a good environmental compatibility. The charge conservation mechanism for pseudo-condensers with $MnO_2$ is based on cation surface adsorption (for example $K^+$, $Na^+$ or $Li^+$, generally indicated with $C^+$) as well as the incorporation of protons according to the following reaction:

$$MnO_2 + xC^+ + yH^+ + (x+y)e^- \leftrightarrow MnOOC_xH_y \qquad (5)$$

However, the theoretical capacitance is rarely reached in the experiments, mainly due to the low electrical conductivity of the manganese oxide (~ $10^{-6}$ S/cm) which limits the working speed for high power performances and therefore hinders its applications in energy storage systems.
Metal oxide electrodes can only be used with aqueous electrolytes, thus limiting the voltage applicable to the cell. The gain in power density coming from the lower resistance is then offset by the loss due to the lower working voltage.
To summarize the discussion on electrodes for both EDLC and pseudo-capacitors, Figure 8 shows the specific capacities achieved by various materials [39].

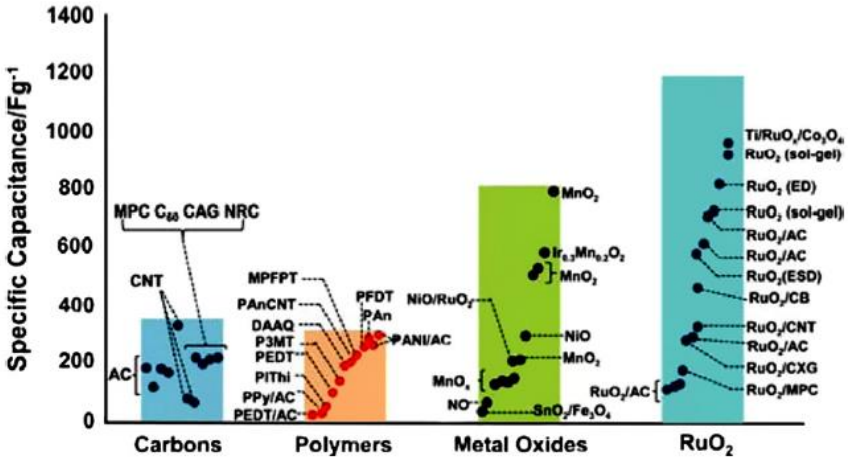


**Figure 8**: Capacitance performance for both EDLC with carbon electrodes and pseudo-capacitor electrodes (including transition metal oxides and conductive polymers).

## 1.2.3 Hybrid SCs

Hybrid SCs are SCs where carbon and faradic electrodes are combined to increase the specific energy. The scientific base for the transition to a hybrid SC was presented in a work on conducting polymers by a research group of the University of Bologna [41]. It was found that a high concentration of polymer cannot be achieved at the negative electrode, but a positive electrode can be effectively realized with the conductive polymer. Thus, a hybrid structure was realized with activated carbon at the negative electrode and conductive polymer at the positive one. The obtained device can be thought like a double-layer capacitor with a pseudo-capacitor in series.
The results of this work are summarized in the Ragone plot of Figure 9: the triangles represent the hybrid SC, while the circles represent the EDLC (carbon) one. The numerical values written on the side of the points are the electric current density in $mA/cm^2$. We notice the large improvement in specific energy thanks to the transition to the hybrid solution.

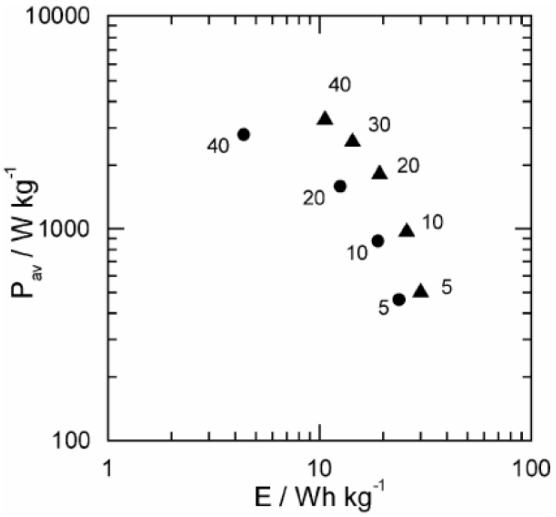


**Figure 9**: Ragone plot of a hybrid (triangle) and of a carbon-based (circle) supercapacitor. Numerical values on the side of the points are the respective electric current density in mA/cm$^2$.

The much higher storable energy is therefore the main advantage of the hybrid SCs with respect to the EDLCs, and then their specific energy goes up to 10-20 Wh/kg. This is a net gain because also the power density is greater than that of the EDLC (see Figure 9). The drawback, due to the presence of the faradic component, is the reduced number of life cycles, which however still remains much higher than that of batteries going up to 100,000. A further advantage over batteries is the easier manufacturing process.

Depending on electrode configuration, hybrid SCs are divided into composite, asymmetric and battery-type.

Composite electrodes integrate carbon-based materials with conductive polymers or metal oxides and incorporate both physical and chemical charge-storage mechanisms into a single electrode. An interesting example of composite electrode is given by nanostructured hybrid materials. In the structure formed by carbon nanotubes and conducting polymers, the strong nanotube interweaving reduces the mechanical stress caused by the insertion and removal of the ions in the conducting polymers, thus preserving the quality of the electrode surface. This results eventually in life cycle stability comparable with that of the EDLCs.

It is also possible to make hybrid ternary structures formed by conductive carbon (e.g. carbon nanotubes), pseudo-capacitive metal oxides and conductive polymers. Figure 10 shows a scheme of a ternary material consisting of a carbon nanotube skeleton, coated with manganese oxide and then with a conductive polymer, PEDOT-PSS [42].

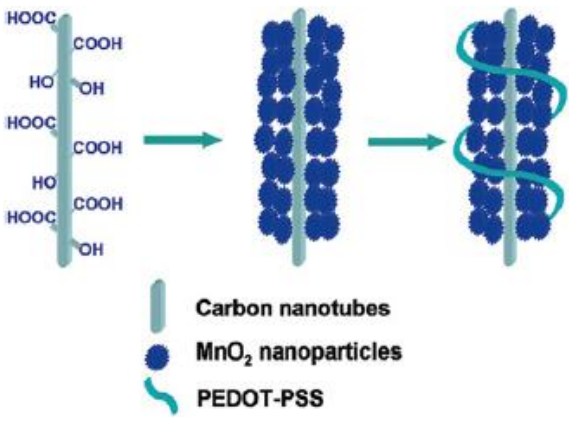


**Figure 10**: $MnO_2$/CNTs/PEDTO-PSS ternary structure.

The key advantages of nanostructured materials therefore include short electron and ion transport paths, large area surfaces exposed by the electrode to the electrolyte, and new reactions which are not allowed in the bulk material. In few words, the specific capacitance of the hybrids is greater than the sum of those of the individual components. The main disadvantages include the increase of unwanted reactions at the electrode-electrolyte interface, among those allowed by the large area, and more complex synthesis processes, with corresponding higher manufacturing costs.
Asymmetric hybrids combine faradic and non-faradic processes by coupling an EDLC electrode with a pseudo-capacitor one. These capacitors mitigate the contrast between achieving greater specific energy and power, generally observed in a Ragone plot, being in a region to the right (more energy) but not lower (not less power) than the EDLC one. Furthermore, they have better cyclic stability than pseudo-capacitors.
Finally, the third category of hybrid SCs is the battery-type. Like the asymmetric hybrids, the battery-like hybrids couple two different electrodes, the first being an EDL and the second that of a battery. Researchers have focused mainly on using nickel hydroxide, lead dioxide, or LTO ($Li_4Ti_5O_{12}$) for one electrode and activated carbon for the other.
Despite initial promising results, the general opinion is that more research is needed to achieve the full potential of battery-type hybrids. The future trends are described in the last paragraph of this chapter.

# 1.3 SC characterization

A SC is well characterized if are known at least its capacitance (F), stored energy (J or Wh) and the maximum power with which its energy is stored or emitted (W) or, in the last case, the ESR (so the maximum power according to Equation 3). Actually, a SC has not only one value for its capacitance as Equation (1) indicates for normal capacitors, instead a SC has a range of capacitances in which the highest one corresponds to a relatively low charge-discharge rate and vice versa. For this reason, there is another parameter for a SC characterization, the ratio between the capacitance at high charge-discharge rate and the maximum capacitance of the same SC that is called *coulombic efficiency*. Moreover, after many charge and discharge cycles, SC performances tend to fall (less capacitance and higher ESR, i.e. less power). The number of cycles after that these parameters changes by a given percentage is called "life cycle". For example, if the capacitance of a SC falls to 95% of its initial value after $10^5$ cycles, then $10^5$ is the life cycle.

In the scientific literature, these five parameters are sufficient to understand the performance of a new electrode or electrolyte or both. In the case of commercial SCs other features are helpful to a full description of an industrial device, which it is not only a combination "electrode and electrolyte" but a cell with specific applications. Some of these features are [43]:

- Maximum continuous current: the maximum constant current (A) a SC can sustain without an increase of its internal temperature exceeding a given number of degrees (for example, 100 A for 10 s and a temperature span of 15 °C). In this case, the temperature is a constraint because a SC electrolyte has not to reach its boiling point.
- Maximum peak current: the maximum current a SC can receive or give in a very short time (for example 1000 A in 1 s).

- Self-discharge: it is the percentage of voltage that a SC naturally loses after it is fully charged and then left in an open circuit (for example 5% after 72 h from the full charge).
- Leakage current: it is the leakage of current that a SC releases in a circuit even when fully charged (for example 3 mA after 72 h from the full charge).

A very important difference between scientific and industrial characterization is the reference mass by which all the performances are reported. For a commercial SC specific capacity, energy and power refer to the total mass of a device (electrode and electrolyte but also current collector, separator, cell box, connections, and label). However, in scientific literature is reported only the mass of the active material (the electrode). Even if the first choice is more intuitive, there is a reason for such difference. A commercial SC is an electric device (so, a complete system), while experimental SCs are physical-chemical systems, in which the main purpose is a new material, for example a new electrode material studied also with other kinds of characterization (electronic microscopy, spectroscopy and so on). Thus, the electro-chemical characterization of this experimental system cannot depend on secondary circumstances as the current collector (when it is not the research focus), the material of the cell and other auxiliary parts.
A separate case are the so-called mini-SCs, a kind of SC made to be very thin and flexible for electronic applications; in this case the performances refer to the area of the electrode, so specific capacity, energy, and power are measured in $F/cm^2$, $mJ/cm^2$ and $mW/cm^2$, as reported in the work of P. Kumar et al. [44].
The main properties of a SC can be characterized using one of the following procedures: Cyclic Voltammetry (CV), Galvanostatic Cycle (GC), and Electrochemical Impedance Spectroscopy (EIS). The experimental apparatus for CV and GC is called *potentiostat-galvanostat*, while an instrument that can perform all the electrochemical analysis is called *electrochemical station*.

### 1.3.1 Cyclic Voltammetry

In a CV, a voltage difference is applied on a SC to read its current response: the voltage changes with time in a linear way as in Equation 6, where $v$ is the scan rate (V/s) and $V_i$ is the initial voltage difference:

$$V(t) = V_i \pm \nu t \qquad (6)$$

When $V(t)$ reaches a final value $V_f$, the scan rate changes its sign, $V(t)$ comes back to $V_i$ and the CV completes a cycle. In an ideal case, during a charging of a SC with capacitance $C$ with a positive scan rate starting from 0 V, the current $I$ (circulating in the system formed by the SC and the potentiostat) can be obtained from the stored charge in the SC,

$$Q = C \cdot V(t) = C \cdot \nu \cdot t \qquad (7)$$

after a time derivative that changes Equation 7 in Equation 8:

$$I = C \cdot \nu \qquad (8)$$

A more realistic SC is like a capacitor coupled with a resistor in parallel with it (with resistance $R_L$, the leakage resistance, as shown in Figure 4c), such that the current is

$$I = C \cdot \nu + \frac{V(t)}{R_L} = C \cdot \nu + \frac{\nu \cdot t}{R_L} \quad (9)$$

During SC discharge, Equations 7 and 8 change only for the sign of the scan rate from $+\nu$ to $-\nu$, so a CV should look like the first and second plot in Figure 11 respectively [35]:

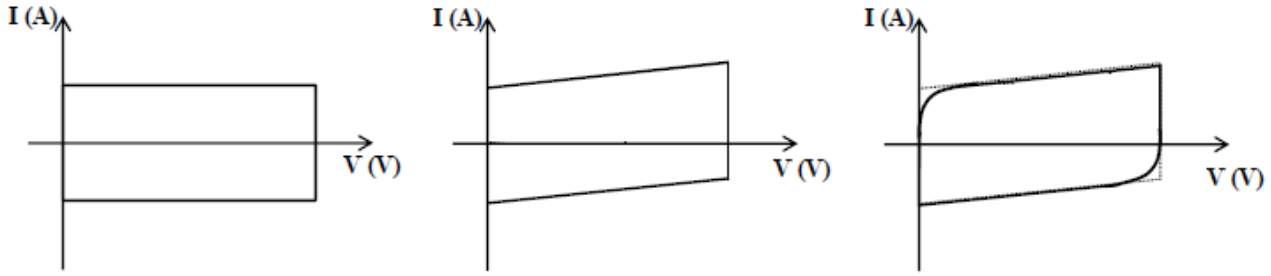


**Figure 11**: CV of an ideal SC (on the left), of a SC with the leakage resistance (in the centre), and a SC with also ESR (on the right).

In fact, since there is a linear relation between voltage and time according to Equation (7), in the first two plots of Figure 11 we can see that the capacitance $C$ is the intercept of the straight line divided by $\pm\nu$, so a first estimation of the capacitance is given by the following equation:

$$C = \frac{I}{\nu} \quad (10)$$

(where the scan rate is taken positive). Moreover, the angular coefficient of the straight line gives information about the leakage, since for high $R_L$ (infinite in the ideal case) the line tends to be horizontal. Actually, there is also a contribution due to the ESR during the changes of sign of the scan rate. ESR causes the curves at the corners of the CV rectangle, so that a typical CV plot is a blunt parallelepiped as in the third image of Figure 11. Nevertheless, CVs are not used to measure the ESR, but SC power can be calculated after the measurement of the stored energy through Equation 2 and dividing it by the charging time $(V_f - V_i)/\nu$.
The general formula for the capacitance C is the Equation 11,

$$C = \frac{1}{\nu(V_f - V_i)} \int_{V_i}^{V_f} I(V)dV \quad (11)$$

in which usually $V_i$ is 0 V and $V_f$ is the maximum voltage before electrolyte breakdown ($V_{MAX}$): 1.0 V for water, 2.5 V for Propylene Carbonate (PC) and 2.7 V for acetonitrile (CAN), the three most common solvent for the electrolytes [45]. If the integral of Equation 11 is calculated along the full closed line of a CV curve, then in the denominator there is also a factor 2, i.e. the capacitance is proportional to half of the area inside the curve. Sometimes the voltage excursion $(V_f - V_i)$ is not from 0 V to $V_{MAX}$ but from $-V_{MAX}$ to $+ V_{MAX}$ to verify the symmetrical behaviour of a SC with respect to the voltage difference [27]; of course in this case the excursion is double the first one but then also the area is almost the double, so according to Equation 11 the capacitance should be almost the same, even if it can be an overestimation [46].

Another cause of capacitance overestimation is the use of Equation 11 to the very first CV of a SC. On the contrary, the capacitance after 20 cycles is a reliable measurement [46], and then a good SC should keep the same capacitance for a large number of charge-discharge cycles.
When the same SC is tested at different scan rates, its decreases at higher rates, not as consequence of Equation 11, but due to the porous nature of the electrode (i.e., the same pore could be harder to charge using higher currents). Figure 12 shows an example of this kind of result with different CVs [47].

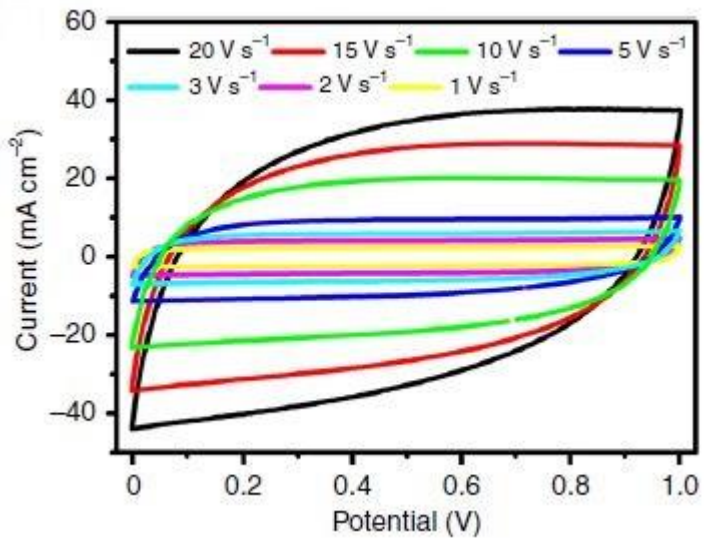


**Figure 12**: Example of CVs at different scan rate to the same SC (in this case, a mini-SC is under test, and the current shown in vertical axis is properly a current density in mA/cm$^2$).

Figure 12 suggests that there is an upper limit to the scan rate, namely when the area inside the curve (so, the capacitance) is too small to be measured or to be of scientific interest. Vice versa, at slower scan rates the capacitance is higher, but at the cost of lower power. Since the right range of the scan rate depends on the size of a SC (area or active mass loading), a general rule to choose this range is that the charge or discharge time should be from 5 s to 60 s [46].
After a capacitance measurement, to describe the performance of the SC under test in a comparable way with other SCs, an analysis has to report its specific capacity (F/g), according the following equation:

$$C_S = 4 \times \frac{C}{m} \qquad (12)$$

In Equation 12, $C_S$ is the specific capacitance (or specific capacity), $C$ is the (absolute) capacitance (measured by Equation 11) and $m$ is the total active mass of the SC, i.e. all the mass loading in a SC (for a common SC with two electrodes, it is the sum of each mass loading). The factor 4 has the following explanation: $C_S$ is the capacitance of one electrode with unitary mass, so since $m$ is the mass of (usually) two electrodes, each of them has a mass $m/2$. Moreover, $C$ is the capacitance of a SC made with a couple of electrodes that act like two SCs in series, having half the capacitance of a single SC. Thus, there is another factor 2 that explains the 4 in Equation 12. For example, if an activated carbon has a specific capacity of 100 F/g, then a SC with a total electrode mass of 100 g will have 2500 F.
A consequence of Equation 12 is that often in a CV diagram the density current or the specific capacity is reported on the y-axis, instead of the (absolute) current. In this way, the current is related

to the size or mass of the SC. Analogously, the specific energy is calculated by Equation 2 using the absolute capacitance *C* and dividing the result by *m* (usually, the specific energy is in Wh/kg, with 1 Wh = 3600 J).

All these considerations about CVs hold true for the EDLCs. However, if a CV concerns a pseudo-capacitor or an EDLC, in which some unwanted chemical reactions take place, there are two features to be taken into account:

1) CV area is not divided in two almost equal parts by the horizontal axis at 0 A, because the charge is not reversible, due to irreversible reactions.
2) There are peaks or cavities along the curve, in correspondence with the voltage threshold of electrochemical reactions. Figure 13 shows two CVs performed on the same kind of SC. In Figure 13a, the test was performed under the so-called two-electrodes configuration (i.e. a test on a couple of electrode), while in Figure13b under the three-electrodes configuration. In these configurations, there are one electrode of the tested SC, a counter-electrode, and a reference electrode [48]. In the case (a), the plot is like an EDLC CV, but the second configuration reveals the faradic reactions that take place near the electrodes. If these reactions were not reversible or not balanced between the two sides of the SC, Figure 13a would be like the 13b.

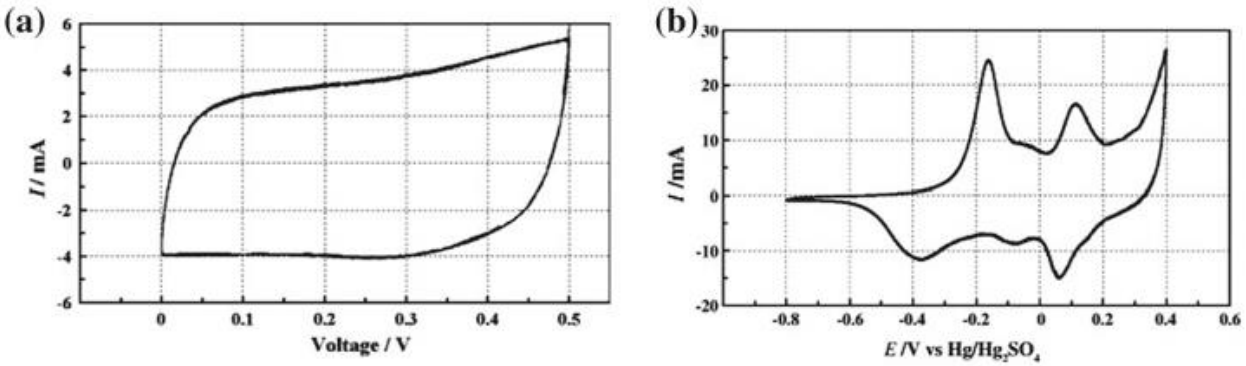


**Figure 13**: CVs comparison between the same pseudo-capacitor under a CV test with a two-electrodes configuration (a) and three-electrodes configuration (b).

## 1.3.2 Galvanostatic Cycles

A galvanostat performs a GC by suppling a constant current to a SC and reading its response in voltage. For a SC with capacitance *C* and internal resistance *ESR*, starting from a zero-voltage difference, the voltage changes during charge with the law:

$$V(t) = \frac{I}{C}t + (ESR) \cdot I \qquad (13)$$

where *I* is the constant current and the term at time 0 is an initial voltage drop on the internal resistance if the SC is described as a RC circuit (as shown in Figure 4b). The current *I* is usually chosen in such a way to obtain a ratio between it and the total mass loading of the SC (*m*) in a range between 0.1 A/g and 10 A/g, hence the GC plots have the current densities as charge/discharge parameter and not the (absolute) currents. A more general form of Equation 13, if a SC is starting from an initial voltage $V_0$ and the voltage drop is $\delta V$, is Equation 14:

$$V(t) = \frac{\pm I}{C} t \pm \delta V + V_0 \qquad (14)$$

in which the sign is + during charge and – during discharge. During a GC, the voltage of a SC starts from 0 and goes to the maximum voltage depending on its electrolyte, as in the CVs, then the sign of the current changes and the voltage falls to zero again. When the current changes its sign, the current variation is *-2I* and Equation 15 allows the ESR measurement,

$$ESR = \frac{\delta V}{2I} \qquad (15)$$

then using Equations 3 and 12 we get power and specific power of the SC under test.
The capacitance is obtained from Equation 14 by the following two formulas, slightly different from each other:

$$C = \frac{I \cdot \Delta t}{\Delta V} \quad (16a) \qquad C = \frac{I}{\frac{dV}{dt}} \quad (16b)$$

Both last equations concern the discharge of a GC. Equation 16a concerns a voltage variation $\Delta V$ that takes place during the time interval $\Delta t$. However, Equation 16b is more correct because it uses the slope of the discharge curve (i.e. the time derivative of the voltage) according to the linearity of Equation 14. Actually, a GC is not always linear, because the leakage phenomenon makes the SC as a RC circuit with also a resistor in parallel with the capacitor (as shown in Figure 4c), so there is a parasite resistor. In this case, the Equation 14 becomes Equation 17:

$$V(t) = \frac{\pm It}{C} e^{-\frac{t}{\tau}} \pm \delta V + V_0 \qquad (17)$$

in which

$$\tau = C \cdot R_L \qquad (18)$$

Figure 14 shows an example of GC with increasing current on the same SC, to explain the cited cases [22]. The red curve at 1 A/g is slightly curved during the charge, with a downward concavity. To avoid an overestimation of the time (so an overestimation of the capacitance, according to equation 16a and 16b), a GC analysis should be performed using two rules:

1) Equation 16a should be used only with the discharge part of the GC plot, in fact, the leakage causes a slower charge of the SC, while discharge time is based on the actual stored charges, even if it is not linear. If the leakage is particularly serious, the discharge time is visibly shorter than the charge time, while if there is no leakage, the CG plot is like an isosceles triangle.
2) The voltage excursion $\Delta V$ should be selected far from the initial drop and from the end of the discharge, because in this way the analysis refers to a portion of the curve that is linear, in good approximation. For example, $\Delta V$ can be taken from 90% to 30% of $V_{MAX}$ [46].

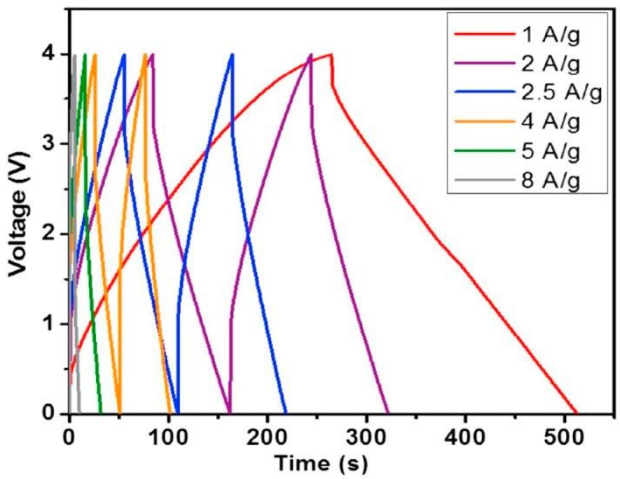


**Figure 14**: Example of GCs at different current densities on the same SC.

These two rules avoid the errors that are consequences of the leakage, even though the leakage itself can be minimized during SC manufacturing process in two ways:

1) With a proper choice of the separator. The separator is usually made with nonwoven cellulose or with polypropylene (PP) or with expanded polyethylene (PE) [49]. The separator avoids electric contact between opposite electrodes (so it avoids short-circuit) and allows the ions flow to them. A very thin separator guarantees a slight improvement in the energy density and a better power performance compared to a not very thin one [50], but the most important feature is its pores: if they are about 1 µm size [49], the ions movement can form the electric double layer near the electrodes, otherwise a part of the ions comes back to the solvent during charge causing the leakage.
2) Making a good quality SC. This solution is obvious, but this is a consequence of Equations 17 and 18: with the same $R_L$, a SC with bigger capacitance has a bigger time constant $\tau$, so in Equation 17 the linear behaviour prevails on the exponential one. Moreover, if the ESR is low, a SC can be tested with high current density, so that the parameter $I$ in Equation 17 is higher and also in this case the linear behaviour surpasses the exponential one.

The second way to prevent leakage concerns the choice of current densities. In GCs, the measured capacitance is higher for the lower current densities, but a too slow current can cause leakage problems and is far from the applications of a SC (this device is used for fast energy storage and delivery). On the contrary, at higher current densities the voltage drop can be so high that the SC stores and delivers low energy, as Figure 14 explains for the GCs at current densities over 2 A/g. A good quality SC should have high capacitance even with high current densities. However, in GCs the charge/discharge time should be between 5 s to 60 s [46]. Therefore, the current density range should be limited, according to these time limits. In the scientific literature, the specific capacity at 1 or 2 A/g is a typical reference to compare different SCs.

CVs and GCs are two electrochemical analyses that are always performed together in a work about SCs, because different results for the same SC should be comparable. Nonetheless, between CV and GC there are some important differences that explain their complementarity:

- In a GC capacitance ($C$) and internal resistance ($ESR$) are decoupled (in Equation 13 they are in different addends), moreover they concern distinct parts of a GC plot. On the contrary, in a CV, ESR causes the roundings of the corners of the closed curve, whose area gives the measurement of the capacitance. So, CVs are not used for the ESR measurement.

- In the case of leakage, there is the opposite situation to the previous point, i.e. in a CV leakage resistance ($R_L$) and capacitance ($C$) are decoupled (Equation 9), while in a GC are entangled (Equations 17 and 18). In a CV plot, leakage causes only an inclination of the entire curve, while in a GC there is the problem of the invalidity of the linear Equation 14, as discussed above.
- SCs companies use only the GC for commercial devices since it is easier and faster to analyse. Among different companies there are only trivial differences for the points that define $\Delta V$ for Equation 16a and often the GCs are not from 0 V to $V_{MAX}$ but from $V_{MAX}/2$ to $V_{MAX}$ and vice versa (hence, due to the quadratic dependence of the energy from the voltage, these GC are based on the storage and delivery of three quarters of the total energy of a SC).

In conclusion, we should explain better the so-called life cycle. The SC life cycles are tested performing a huge number of GCs, for example 10'000, reporting a capacitance measurement every 100 cycles. The crucial parameter for this kind of test is the charge/discharge time, which is calculated from Equation 16a:

$$\Delta t = \frac{C \cdot \Delta V}{I} \qquad (19)$$

The life cycle of a commercial SC can be till one million cycles and to test it a common laboratory electrochemical station is not enough: for a commercial SC cell of 3000 F, GCs between 1.35 V and 2.70 V, if every cycle lasts a time $2\Delta t$, it needs a 300 A current to perform a GC in 27 s, while a full test of half million cycles would last 156 days. These tests are performed by a huge DC generator called *cyclator*. A cyclator supplies constant currents of the order of $10^2$ A and voltage of 10-30 V both for life cycle tests and for GCs on the so-called SC-modules, i.e. several SC cell connected in series to reach values multiple of a single cell voltage.
Life cycle needs a couple of other scientific considerations about the actual lifetime of a SC and about its implicit linear approximation.
Lifetime of a SC depends on many factors, regardless life cycle. A crucial factor is inevitable electrolyte degradation. Of course, with high power applications, the life-span is lower and SCs are used exactly for these applications. Moreover, since the charge/discharge time of a SC is only of few seconds or few minutes, in a given time interval a SC performs more cycles than an electrochemical battery. Nonetheless, as on field estimation, a lead acid battery lasts about from six months to two years, while a SC can last till 10-30 years.
Moreover, SC performance degradation along its life cycle is not linear, as it could be hypothesized. Instead, it is as shown in Figure 15 [51].

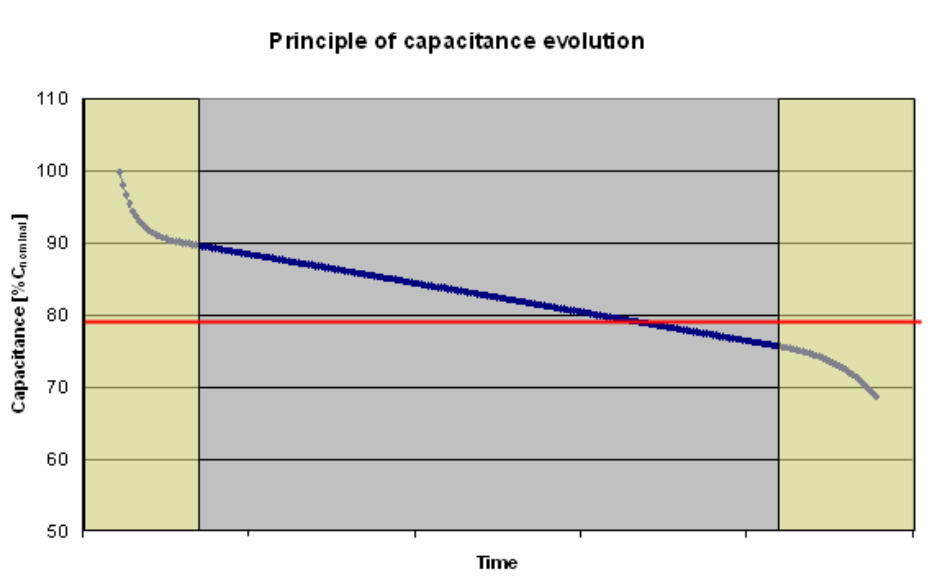


**Figure 15:** Life cycle of a commercial SC in terms of percentage reduction during time of the initial capacitance. The green areas delimit the non-linear trends, the blue area the linear one. The red line is the threshold for the definition of the life cycle.

The real life cycle trend is a negative exponential during the very first cycles (not more than the first 10), then is linear for a high number of cycles but a life cycle test ends when the capacitance becomes the 80% of its starting value (i.e. the rated capacitance). The number of cycles in correspondence of the intersection between the capacitance and the 80%-threshold is by definition the life cycle of a commercial SC. After a certain number of cycles beyond this point, the capacitance falls faster than a linear trend. The exact number of these cycles is not very important (so it is not indicated) because a drop of the 20% of the capacitance (so a loss of the 20% of the energy and usually also at the same time of the 50% of the power) is already big enough to end the use of a device. Thanks to the 80%-threshold that cuts off the non-linear ending part of the curve, a life cycle estimation is a direct measurement and not an extrapolation. An extrapolation would be statistically incorrect, as general rule for every kind of data analysis.

### 1.3.3 Electrochemical Impedance Spectroscopy

The EIS is a frequency analysis of a SC: a small AC voltage is applied on a SC, changing its frequency from $10^{-2}$ Hz (or from $10^{-3}$ Hz, when possible) to $10^{4}$ Hz. Since a SC is modelized as an RC circuit (as shown in Figure 4b), every components responds to the frequencies according to its typical impedance. In first approximation, SC impedance is

$$Z(\omega) = ESR - i\frac{1}{\omega C} \qquad (20)$$

in which $i$ is the imaginary unit, $\omega$ is the pulsation of a sinusoidal voltage like in Equation 21a:

$$V(t) = V_0 \sin(\omega t) \qquad (21a)$$
$$I(t) = I_0 \sin(\omega t - \varphi) \qquad (21b)$$

where $\omega$ is $2\pi f$ ($f$ is the oscillation frequency) while $V_0$ is usually about 5 mV. The impedance measurements derive from a ratio between V(t) and the current response of each component of SC model, i.e. a current like Equation 21b (the linearity of this response is a consequence of the small value of $V_0$ [52]). Using the complex numbers representation of Equations 21a-b and measuring the ratio $V/I$ at different frequencies, EIS provides the measurements of the real and imaginary part of Z(ω) in the first member of Equation 20. An appropriate model of the system (in our case a SC) makes possible an interpretation of the parts of Z.
In the case of Equation 20, the two terms of the second member are the resistive impedance and the capacitive impedance, respectively. At low frequencies, Z is mainly capacitive, so at least in principle EIS can give an estimation (precisely an underestimation) of the capacitance $C$ by Equation 22:

$$|Z_C(\omega)| = \frac{1}{\omega C} \quad \Leftrightarrow \quad C = \frac{1}{\omega |Z_C(\omega)|} \qquad (22)$$

Actually, EIS is used mainly as further measurement of the ESR, usually after that of a GC. In this case, for high frequencies Z is predominantly the internal resistance. For a more accurate measurement, the impedance is drawn in its components (real part and the opposite of the imaginary part) on the so-called Nyquist plot, as shown in Figure 16a [46].

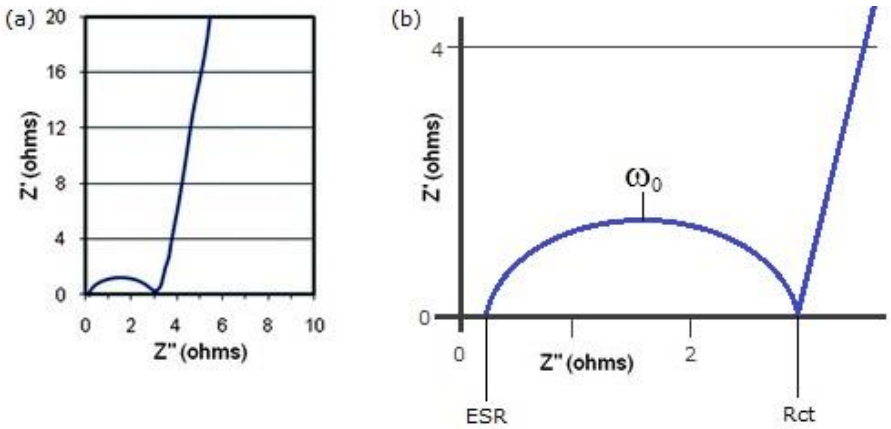


**Figure 16**: (a) Example of a Nyquist plot of a SC. Z' is the opposite of the imaginary part of the impedance while Z" is the real one; (b) zoom near the origin (high frequencies) with the point interpretation.

Figure 16a shows that the Nyquist plot of a SC is not made with only a vertical line shifted by ESR from the origin, as Equation 20 should indicate. A realistic Nyquist plot has different zones that give useful information.

- The first intersection near the origin of the real axis (also shown in Figure 16b). This point is a measurement of the ESR, i.e. the internal resistance of a SC that includes all the sources of resistance (current collector/electrode interface, ions movements inside the pores, resistance of the solvent). This point concerns the highest frequency during an EIS.
- The semicircle at high frequencies (in Figure 16b). The semicircle is due to the formation of a circuit with a resistor ($R_{ct}$) in parallel with a capacitance and the ESR in series [53]. They are the resistance and the capacitance due to the electrons transfer and the double layer formation at the electrode/electrolyte interface; this phenomenon is called *Interfacial Charge Transfer* [52]. $R_{ct}$ is the second intersection of the real axis (Figure 16a-b). $R_{ct}$ is due to contact resistance, so it depends on the quality of cell assembly. For example, Figure 17a

refers to a SC of the same kind of Figure 16 but was hand-made and not already-packaged [46]. In this case, the end of the semicircle is at a higher resistance and does not touch the real axis.

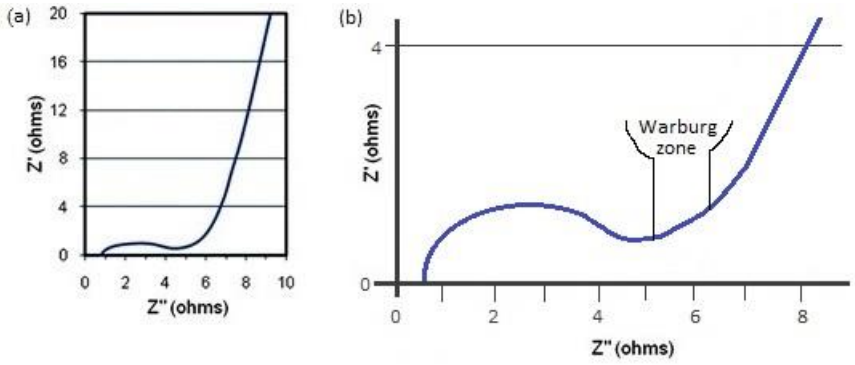


**Figure 17**: (a) Nyquist plot of a SC made with standard material but with a hand-made package and (b) its zoom at high frequency with the Warburg zone.

- The first slope of the straight line (Figure 17b). There is sometimes a line tilted at 45° after the semicircle that is called *Warburg element at mid-frequency* (knee frequency) *zone* [52]. This zone is due to an eventual ions concentration gradient in the electrolyte, but a good quality SC should not show it (Figure 16 has not this zone but Figure 17 shows it). If there is not a concentration gradient, it means that the pore size is fitted for the ions size, so this part of the plot is helpful for this information [35].
- The second slope of the straight line. The main straight line is due to the capacitive impedance of Equation 20 and its physical phenomenon is the double-layer formation. The persistence of a small slope is due to remaining ion diffusion.
- The hypothetic maximum point. As the frequency slows down, the plot rises vertically on the Nyquist plot and its limit is only the minimum frequency with which it can work. For example, 1 mHz corresponds to an oscillation period of 1000 s, i.e. 16.7 minutes for every oscillation. Smaller frequency would need even more time, so an EIS usually stops at this lower limit. However, at very small frequency the current/behaviour is almost a DC charge, so the impedance is mainly capacitive as in a GC or in a RC circuit at constant voltage.

In an EIS, the analysis also includes plotting opposite of the phase angle ($\varphi$) versus the frequency, the Bode plot. A Bode plot shows the same behaviour of a SC at different frequencies described in a

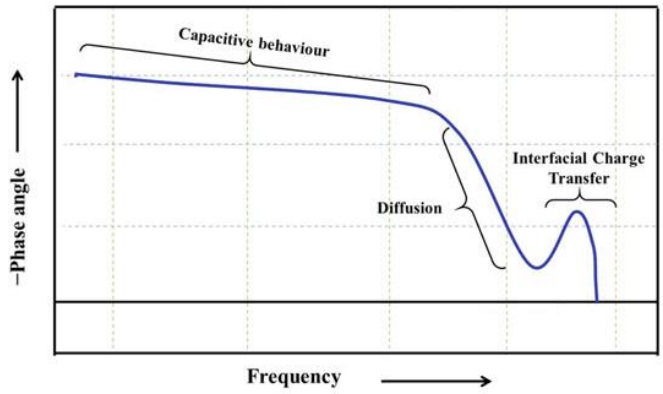


**Figure 18**: Bode plot of a SC as the opposite of the phase angle ($-\varphi$) vs frequency.

Nyquist plot, i.e. the capacitive behaviour of the double-layer formation, the diffusion, and the interfacial charge transfer, as explained in Figure 18 [52].
A helpful quantitative information comes from the frequency ($\omega_0 = 2\pi f_0$) at the phase angle of -45°. This point corresponds to the point on the Nyquist plot in the centre of the semi-circumference arc. In particular

$$f_0 = \frac{1}{R_{ct}C} \qquad (23)$$

Since the resistance $R_{ct}$ can be directly read from the Nyquist plot (the right end of the semicircle), inverting the Equation 20 it is possible to get another estimation of $C$.
Even if Equations 22 and 23 can give an estimation of $C$, an EIS is usually used only for the ESR for two reasons:

1) Equation 22 is valid at low frequencies, but it is an underestimation, as said above.
2) Equation 23 is valid only if the experimental plot at high frequencies is a perfect semicircle like in Figure 16a, but often a Nyquist plot shows either an incomplete semicircle (as in Figure 17a) or an oval or elliptical curve. In fact, from a computational point of view, an EIS needs to set up an explicit circuital model to extrapolate the required parameters (in fact EIS software does not use a pure capacitance but a model for a double layer capacitance in case of porous materials). On the contrary, for a CV or a GC we can directly use their formulas (Equations 11, 15, and 16a-b).

# 1.4 Overview of current research works

The interest about SCs is growing in the last decades for two reasons: because they are involved in many economic sectors and because the ways to improve them are very branched, so they offer many possible lines of researches. On the economic side, SC applications concern the most recent global trends of green energy, electric cars, micro-grids, public transports, and energy saving. Even if their involvement can be indirect, an improvement in their performances or in their scalability also supports the cited sectors.
On the scientific side, a simple example of how the interest is growing is shown in Figure 19 [32].

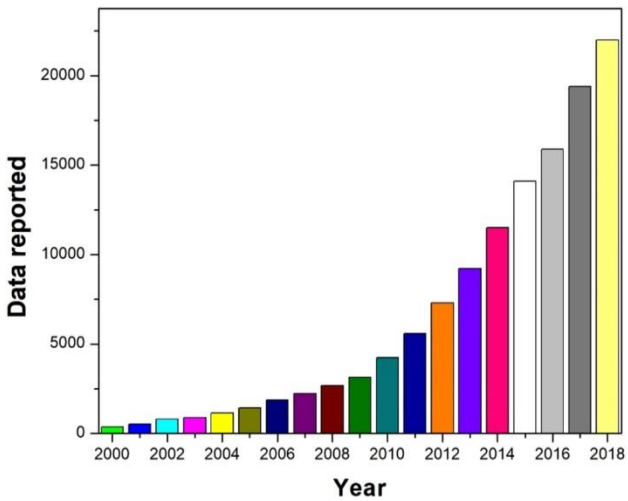


**Figure 19**: Publications about SCs in the last years.

Figure 19 shows an almost exponential trend, so a number of publications that grows with a velocity proportional to it. Therefore, to summarize such trend a review should be as updated as possible, but an overview about these researches can be also discussed through their main subjects, with some reference points. Every improvement in SC field consists of a new kind of SC with at least one of the following elements compared to its similar predecessor:
- an electrode material that has a higher specific capacity;
- an electrolyte that permits a higher specific capacity;
- an electrolyte that can sustain a higher working voltage;
- a combination of materials that make a SC with higher power density;
- a cheaper or more ecological element or both;
- a more scalable material or manufacturing process or both;
- the unification of two functions in the same material;
- a non-electrode-material with lower density or thinner thickness;
- a longer life cycle;
- a smaller leakage.

Even if in the following two sub-paragraphs the main subjects are the innovative electrodes and electrolytes, often there will be also the other features cited in this list. Of course, SCs are interdisciplinary systems, from the materials science to engineering, so this is another reason for the extended scientific literature about them.

### 1.4.1 Innovative electrodes

The main group of electrode materials concerns the carbon-materials, from the Activated Carbon (AC) to the so-called onion-like carbon, carbon nanotubes (CNTs) and all the graphene-like materials as graphene itself, Graphene Oxide (GO) and reduced Graphene Oxide (rGO). Other two groups of materials are the conductive polymers and the metal oxides. The materials of the first group have in common a relatively cheap raw material, i.e. carbon or graphite. Any manufacturing process on carbon and graphite concerns their porosity and their electrical conductivity, in a trade-off between better performances and scalable fabrication. Moreover, almost all the carbon-based and graphene-based SCs are EDLCs, as current commercial SCs, so the next SC generations will probably be a new kind of SC belonging to this group.
On the contrary, conductive polymers and metal oxides are less cheap and they are usually used for pseudo-capacitors, but in general, they have higher energy density with a reduction power density. This trade-off and other problematic details make not easy the choice among the innovative electrodes, so the market constrains will probably cut some lines, but the possibilities are wide for every branch of research.

**Activated Carbon**

AC is the current material of commercial SCs, in particular for EDLCs with an organic electrolyte [54]. It derives from a chemical or thermal process called indeed “activation” by which the common charcoal develops a high porosity, so a wide specific surface. An improvement of such material can concern the porosity or the raw material. There were many progresses in the preparation of new activated carbon, mainly in achieving higher specific area from a minimum of 1150 $m^2/g$ [55] to a record of 3000 $m^2/g$, using new processes, as chemical activation with KOH [56], or starting from a

new biological matter, namely a seaweed biopolymer [57]. In any case, specific area cannot be the only one important parameter, as demonstrated by the unsatisfactory capacity value of 10 mF/cm$^2$ obtained by the 3000 m$^2$/g activated carbon, against common values of 15-25 mF/cm$^2$ a exhibited by EDLC with standard activated carbon. Consequently, a second relevant parameter should be the presence of a mix of pores with different sizes that best fit the employed electrolyte, so that both good capacitance and good power performance can be simultaneously achieved. Moreover, an excessive specific area can be correlated to the presence of immobilized free radical that may cause degradation of the electrolyte, especially with organic solvents. Therefore, it is general opinion that a process to produce activated carbon from waste, such as sugar cane bagasse, cellulose, sawdust, cherry stone, and corn grains would be preferable, also from an ecological point of view [58].

**Carbon Nanotubes**

Many research works inspect carbon nanotubes (CNTs). Generally, CNTs can be made in two ways: a single graphite sheet curled into cylindrical form having a single-walled CNT (SWCNT), or a multi-walled CNTs (MWCNTs) that contains many concentric SWCNTs with different diameters. CNTs attract researchers' interest due to their high specific capacity and because they are able to sustain high currents.

A CNT-based electrode has a mesoporous matrix which favours the ion diffusion to the active surfaces, and they can reach high values of surface area up to 1600 m$^2$/g, besides a good electrical conductivity ($10^5$ S/cm) [59]. Moreover, CNTs have low mass density and intrinsic flexibility. Some practical limits are determined by the formation of only micropores and so by the increase of the internal resistance, so that the actual performances can be less than the theoretical ones. Finally, their manipulation can give toxicity issues during processing.

In a recent work, CNTs were coupled with flexible carbon fiber (CF) to make a hybrid electrode (CF-CNT). A further improvement was to develop a 3D composite architecture with a combination of CF, CNT, and graphene. This electrode was realized by Xiong et al. [60] working on reduced graphene oxide and CNTs grown on CF using electrophoretic deposition and chemical vapor deposition (see Figure 20). The 3D electrode showed a specific capacity of 203 F/g, which is 4 times greater than that of pure CF.

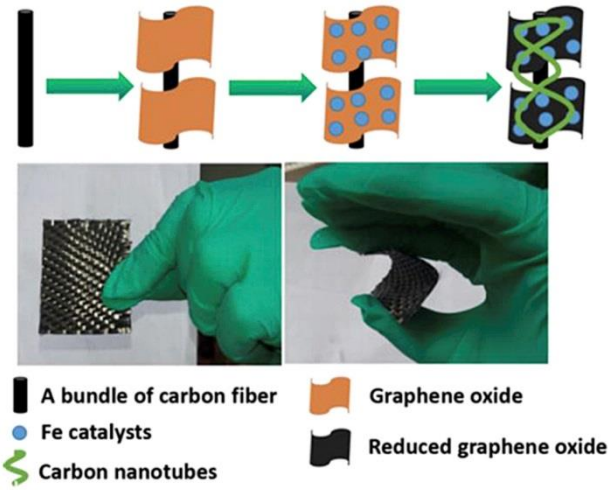


**Figure 20**: Scheme of the synthesis of the 3D CF-rGO-CNT hybrid.

**Graphene**

The material that presently is attracting most research activity is graphene with its derivatives: graphene oxide (GO), reduced graphene oxide (rGO), and graphene combined with different materials. Graphene is the well-known two-dimensional material made of carbon atoms arranged in a honeycomb pattern. It has many extraordinary properties, the electric and geometric ones being the most relevant for SC realization: electrical conductivity (sheet resistance of only 30 Ω/sq [61]), electrical mobility (15,000 $cm^2V^{-1}s^{-1}$ [62]) and specific area (2675 $m^2/g$) [63].

The maximum theoretically achievable specific capacity is 550 F/g. However, this very large value would be obtained only by a perfect configuration with graphene sheets perpendicular to the current collectors, and this is not an easy task to achieve. Graphene-based SCs with ionic liquid salts, aqueous electrolytes and organic electrolytes can reach specific capacity of 75 [64], 135, and 99 F/g [65], respectively. Reduced graphene oxide, when produced with low agglomeration, can reach a maximum specific capacity of 205 F/g in an aqueous electrolyte, yielding an energy density of 28.5 Wh/kg [66].

A great number of uses of graphene are possible in SC production, here we report just four significant strategies.

Graphene can be nanostructured, i.e. it can be coated on another material to obtain a special structure, for example it can be put on textile fibre (adding $MnO_2$, see Figure 21) [67] to gain higher specific capacity (315 F/g), specific energy (12.5 Wh/kg), and mainly more life cycle stability (100,000 cycles of charge/discharge, a quite high value compared with other sophisticated SCs).

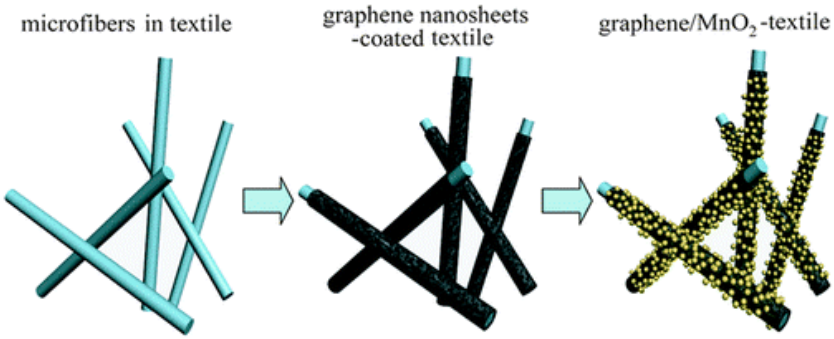


**Figure 21**: Illustration of the steps to produce the hybrid structure: in blue, the microfibers that are covered with graphene sheets (in grey), and which finally receive the $MnO_2$ particles (in yellow) by controlled electrodeposition.

In another work [68], researchers from the University of Salerno (Italy) covered nanoparticles of Fe3O4 (5-8 nm) with graphene sheets. After annealing, a SC with an aqueous electrolyte and this kind of electrode reached the outstanding specific capacity and energy of 787 F/g and 109 Wh/kg, respectively [68]. Its specific power range was between 250 and 9000 W/kg according to a specific current range of 0.5-18 A/g and its life cycle was about 30,000 cycles.

Another very common strategy to improve graphene-based SCs, and in particular to prevent restacking of the sheets, is based on the use of functionalized graphene. A functionalized graphene is a graphene with another chemical element or group, functional group, linked to its surface with a controlled density, to obtain additional specific properties, without a significant decrease of the electrical conductivity. This technique is applied also for biotechnological applications [69]. In SC field, we can mention a graphene electrode functionalized by nitrogen atoms [70] (see Figure 22). A remarkable result shown in this work is that the nitrogen functionalization is obtained directly

during the production process of the graphene-like material from shrimp shells, used as starting raw material.

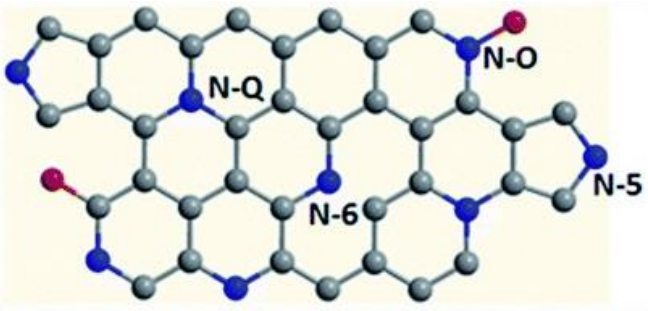


**Figure 22**: Nitrogen-functionalized graphene model for the work described in the text.

A SC with this kind of electrodes and aqueous electrolyte showed a maximum specific energy of 11.2 Wh/kg that is reduced to 8.4 Wh/kg when tested at the maximum power of 25,400 W/kg.
A third strategy, which gained a relevant industrial impact, is the use of curved graphene. Although graphene is by definition a two-dimensional material, its perfect flatness does not help in SC applications, and it may even be useless when parallel to the current collector. A curved graphene has proven to be more effective. The curved graphene is in fact a graphene sheet made in a concave shape to better expose its area and to avoid the stacking of graphene planes. We can see an example of this graphene in Figure 23 [63].

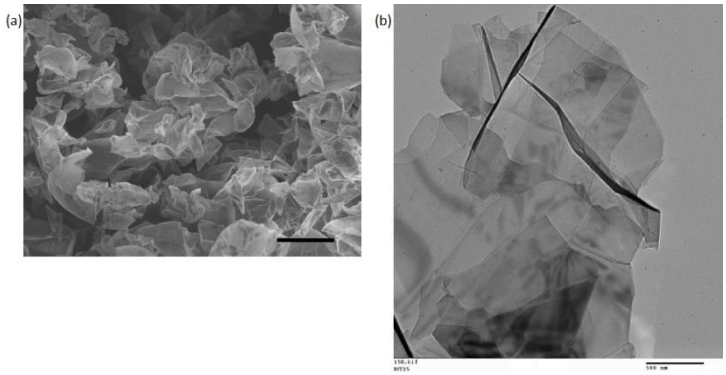


**Figure 23**: (a): SEM image of the curved graphene layers (scale bar: 10 µm); (b): TEM image of planar layers of graphene prepared with the usual chemical procedure, which overlap so they have the relative space as in the graphite bulk, i.e. less than 1 nm (scale bar: 500 nm).

The structure shown in Figure 23a has pores between 2 and 25 nm (mesopores). This curved graphene was employed in a SC with 5wt% carbon black and an ionic liquid salt that can sustain a maximum voltage of 4.0 V. Carbon black is a common additive used to improve AC-based electrodes [71]. The obtained specific energy is in the range 21.4-42.8 Wh/kg, depending on the electrode mass fraction.
Finally, a very recent strategy deals with graphene-based aerogel-like material. It is known that a SC cannot work outside the electrochemical stability window because solvent electrolysis reactions take place and the reaction products can obstruct the pores of the electrode, reducing both the capacitance and the life cycle of the device. Avoiding the occurrence of such phenomena actually determines the electrode stability to the applied voltage. In a recent work [36], a research group at the Tohoku University (Japan) showed a new electrode material made of seamless mesoporous carbon sheet consisting of a continuous three-dimensional framework of graphene mesosponge

(GMS). It can be seen like a mesoporous carbon made of edge-free graphene walls. This material is very attractive for its high specific surface area (1500 $m^2/g$); however its main feature is the possibility of using it to assemble symmetric SCs that can work up to 3.5 V and 4.4 V, at 60 and 25 ºC respectively. It is worth noting that these results were obtained using a conventional electrolyte (1 M $Et_3MeNBF_4$/propylene carbonate TEMATFB/PC electrolyte) generally limited to 2.7 V.
GMS is prepared using $Al_2O_3$ nanoparticles as a hard template (Figure 24d). A graphene-like material is deposited of an $Al_2O_3$ surface through Chemical Vapour Deposition (CVD) of $CH_4$, followed by template removal by chemical etching. The resulting mesoporous carbon is then annealed at 1800 ºC to convert discrete graphene into the continuous GMS. Then GMS is obtained in powder form and eventually in a self-standing GMS sheet (Figure 24e). Figures 24a-c show also the main carbon materials (CNTs, rGO and activated carbon, AC) employed in SCs.

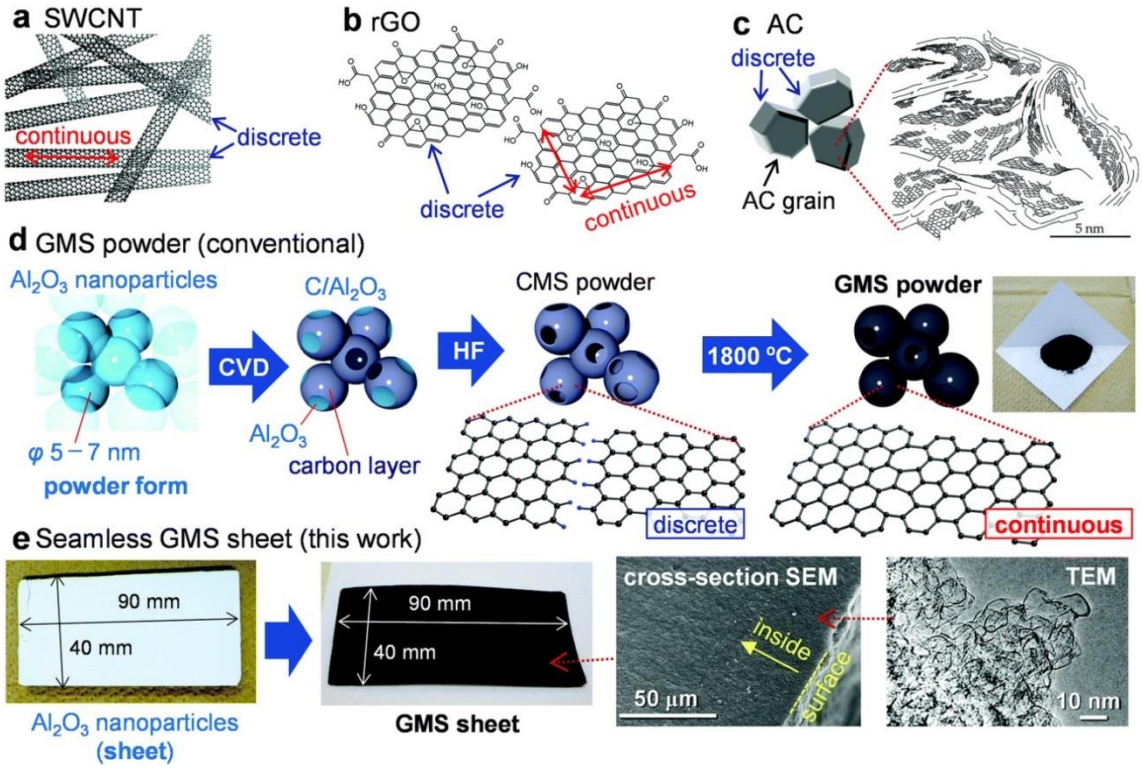


**Figure 24:** A list of carbon materials examined in this work. (a) SWCNTs, (b) rGO and (c) AC. The inset depicts the molecular-level structure of AC (d) Preparation scheme of the GMS powder, together with its photograph. (e) Photographs of sheet-moulded Al2O3 nanoparticles (template) and a resulting seamless GMS sheet. Cross-sectional SEM and TEM images of the GMS sheet are also shown.

In case of high-voltage operation, the GMS sheet exhibits a high energy density (60 Wh/kg) at 1 kW/kg. This energy value is 2.7 times higher than that of the conventional AC at the same operating power, which however is very low with respect to common applications. Finally, the GMS sheet retained its capacitance over 100,000 cycles.

**Conducting Polymers**

Normal polymers are electric insulant, but they can become conductive through a doping process similar to the one of semiconductor. Among conducting polymers (CPs), polyaniline (PANI), polypyrrole (PPy), and polythiophene derivatives got particular attention as SC electrode materials for their high conductivity and their low cost [72, 73]. Optimizing the morphology of CPs is an

important factor for the electrochemical performance of the resulting SCs. In particular, nanostructured CPs can achieve better performances than their bulk variation.
PANI (polyaniline) is a conducting polymer that has found promising applications in energy storage devices due to its easy synthesis, low cost, good electrical activity, and good stability. However, bulk PANI has low available surface area, thus the nanostructured version is always preferred. Moreover, to make a SC electrode, the PANI nanostructure needs a binder that can distort the structure and introduce inert materials in it. This problem is usually afforded with electrospinning and addition of small quantities of a different polymer. Simotwo et al. [26] found a facile approach to the fabrication of PANI nanofiber electrodes, without any binder, by means of electrospinning and CNTs. The SEM image in Figure 25a shows that electrospinning PANI at 93% solution produces a continuous and nonwoven nanofiber structure with controllable inter-fiber porosity. CNT addition (Figure 25b) does not degrade in any way the nanostructure. In a following work, Li et al. [74] prepared a SC electrode by a PANI nanofiber coated with graphite, showing a capacitance of 2136 F/g at a current density of 1 A/g, in 6 M $H_2SO_4$ and 91% capacitive retention up to 1000 cycles.

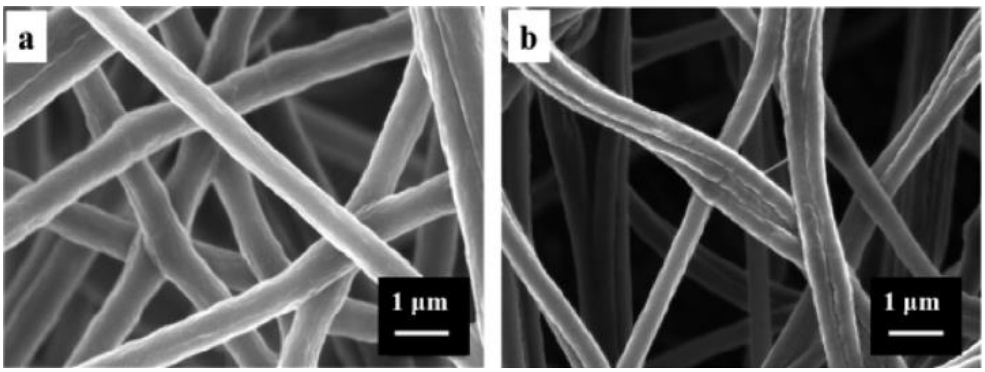

**Figure 25**: SEM images of (a) PANI and (b) PANI-CNT.

The polypyrrole (PPy) has received a lot of interest because it is water soluble and commercially available; it can store high specific energy, show reversible electrochemical doping/de-doping, and easy electrochemical processability. One research group [75] recently prepared the rGO/PPy/$Cu_2O$-$Cu(OH)_2$ ternary nanocomposite as an electrode material for SCs. In three electrode systems, this nanocomposite showed a gravimetric specific capacity of 997 F/g at a current density of 10 A/g. The EDLC with the PC and this kind of electrode resulted in specific energy and power of 20 Wh/kg and 8 kW/kg, respectively; while at the maximum specific power of 20 kW/kg, the specific energy was reduced to 5.8 Wh/kg, with capacitance retention of 90% after 2000 cycles.

**Metal Oxides**

The metal oxides used for SCs belong mainly to the transition metal family, such as nickel oxides (NiO), cobalt oxide ($Co_3O_4$), ruthenium oxide ($RuO_2$) and manganese dioxide ($MnO_2$). They raised interest due to their mesoporous structures, yielding high specific capacity [76, 77]. However, they are expensive materials, so many researchers considered also cheaper and earth-abundant alternatives. In particular, cobalt sulphide materials, such as $Co_3S_4$, $CoS_2$, $Co_9S_8$, $Co_1$-xS and $Co_xS_y$, have gained attention for their wide stoichiometric composition and good stability. However, the development of these materials is still at an early stage. Other metals oxides for SCs with neutral solutions are iron oxide ($Fe_2O_3$), vanadium oxide ($V_2O_5$), indium oxide ($In_2O_3$) and tin oxide ($SnO_2$).

**Composites**

Composite materials are presently the best and most studied choice for electrodes. We already mentioned different examples of electrodes made by a combination of materials: carbon-based material with another carbon-based material (AC with rGO, graphene on CNTs, and so on); carbon-based materials and metals oxides; carbon-based materials and ad hoc chosen materials.

Recent research has shown that graphene is the most adaptable and promising material. Graphene composites are usually multiphase materials in which graphene is mixed into a ceramic, polymeric or metallic matrix by physical processing techniques, such as shear mixing or ball milling [78].

## 1.4.2 New electrolytes

The most efficient way to increase the specific energy of SCs, at least from a simple mathematical point of view, could be finding a new electrolytic solution able to withstand higher voltage. In fact, this is a simple consequence of Equation 2 that states that the stored energy in a SC depends linearly on capacitance but quadratically on voltage. Moreover, it is possible to improve electrolyte performances also choosing ion molecules with suitable geometry. In fact, smaller ions can better fit in smaller pores, thus better exploiting all the available surface of the pores. In this way, the effective capacitance of the same electrode will result greater than that obtained with the usual commercial organic salts (e.g. TEATFB or TEMATFB) and more energy can be stored in the SC.

As said before, the most common electrolyte solvent in a commercial SC is acetonitrile, which works with a maximum voltage of 2.7–2.85 V [45]. However, in the scientific literature, there are many papers dealing with solid-state and quasi-solid state electrolytes. Solid-state electrolytes mitigate the risk of leakage, a common problem for liquid electrolytes. Leakage is the phenomenon for which a SC, charged at maximum voltage, loses charges due to small currents (exchange of charge carriers between the electrolyte and the electrode), which should be absent in the ideal case (constant voltage at complete charging) but in practice unavoidable, because of electrode irregularities at the molecular scale. In SCs with liquid electrolyte, leakage is caused by the normal limits of the stability of the double layer formed near the electrodes. This problem is obviously much less severe in SCs with solid electrolytes. The latter, however, have lower conductivity than liquid ones.

Other aspects afforded by the research on electrolytes are the working temperature range (which then affects the operating temperature range of the SC), the specific heat and the thermal conductivity (i.e. the thermal stability, which is related to the maximum current that a SC can deliver and dissipate), and the environmental impact (i.e. how ecological electrolyte preparation and its disposal are).

**Aqueous electrolytes**

Aqueous electrolytes are grouped into alkaline, acid, and neutral solutions, of which $Na_2SO_4$, $H_2SO_4$ and KOH are the most commonly used representatives. Generally, aqueous electrolytes show good conductivity (e.g. 0.8 S/cm for 1 M $H_2SO_4$ at 25 °C) but they must be coupled with suitable electrodes to compensate the relatively low ESW.

Qu et al. [79] studied the performances of $MnO_2$ nanorods using neutral aqueous electrolytes (e.g. $Li_2SO_4$, $K_2SO_4$ and $Na_2SO_4$). In Figure 26a, a SEM image of the nanorods is shown. The newly

fabricated AC SC showed good life cycle stability (Figure 26b) with large specific energy (17 Wh/kg) and power (2 kW/kg).

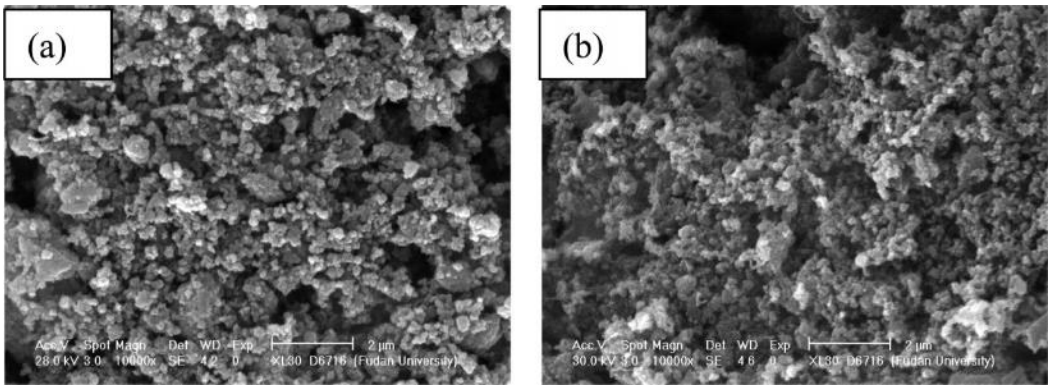


**Figure 26**: SEM images of the $MnO_2$ electrodes, (a) native and (b) after 23,000 cycles.

In another study [80], the combination of $NaMnO_2$ and activated carbon was tested using aqueous solution of $Na_2SO_4$ (see Figure 27). This system delivers a maximum specific energy of 19.5 Wh/kg at a power of 130 W/kg. The measured capacitance loss is about 3% after 10,000 cycles, and the estimated remaining capacitance after 100,000 cycles is above 80%.

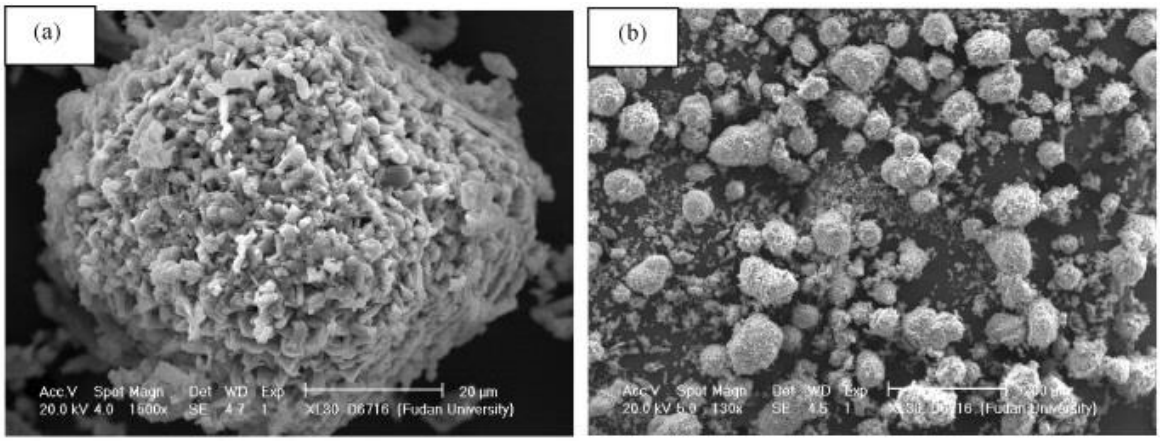


**Figure 27**: SEM images of the as-prepared $NaMnO_2$ with different scales: (a) 20 μm and (b) 200 μm.

**Organic electrolytes**

We already explained advantages (wide ESW) and disadvantages (lower conductivity, toxicity, flammability, volatility, and hygroscopicity) of the organic electrolyte, in particular of the most common one, acetonitrile (ACN) with TEATFB. The second most common solvent is PC, because even if it has a lower ESW (2.5V), it has a lower toxicity than ACN, wide liquid-phase temperature range and resistance against hydrolysis [81].

A first example of an alternative electrolyte comes from a research published in 2010 [82], where NASA Tech Briefs reported about an organic electrolyte with a freezing temperature of −85.7 °C. It was formulated by the addition of $TEABF_4$ to mixed CAN and 1,3-dioxolane (DOL) at 1:1 volume ratio. The cell filled with this electrolyte showed highly linear discharge curves over a wide range of temperatures. Of course, it can be considered a good solution for special applications at low temperature working condition.

For what concerns more substantial alternatives, a first strategy consists in the search for new organic salts. Some asymmetric tetraalkylammonium salts and cyclic quaternary ammonium salts

were thus explored, including triethylmethylammonium (TEMATFB), 1-ethyl-1-methyl-pyrrolidinium (EMPYTFB), and tetramethylenepyrrolidinium (TMPYTFB) [83]. These salts show higher solubility in PC, thus can be used in higher concentrations and hence offer higher conductivity than commonly employed salts, e.g. TEATFB. However, many studies showed that it is highly challenging to increase the operating voltage beyond 3V for EDLCs using any known commercial electrolyte [81].
Novel electrolytes including new solvents were published in the scientific literature with the aim of significantly increasing the operating voltage. Some of them are based on linear sulphones, as the Ethyl isopropyl Sulphone (EiPS, operating up to 3.7 V [84]), alkylated cyclic carbonates, as the 2,3-butylene carbonate (2,3-BC, up to 3.5 V [85]), and adiponitrile (AND, up to 3.75 V [86]). Unfortunately, their relatively high viscosity and low ionic conductivity, especially at room temperature, reduce the power performance of such EDLCs.

**Ionic Liquid Electrolytes**

An alternative to electrolyte solutions is represented by ionic liquids (IL). IL are salts that as a result of a deprived crystalline packaging (when, for example, cations are particularly large compared to anions and have a low degree of symmetry) are in the liquid state at room temperature and often also at lower temperatures. The ionic nature of these materials and the weak coordination between the ions prevent their evaporation, so IL do not have a measurable vapour pressure and have a high chemical stability at high temperatures, even greater than 400 °C [87].
In an EDLC with ionic liquids, the formation process of the double layer is quite different from the other cases because, due to the absence of the solvent, the ions have not a solvation sphere around them and therefore the distance from the charges in the electrode is shorter. This peculiarity results in a large increase of the most important SC feature, the ESW, which can reach values over 5 V [88].
A good example of IL for SC technology is the $PYR_{14}TFSI$, pyrrolidinium trifluoromethanesulphonylimide. Its electrochemical properties, hydrophobic nature, high level of purity, are well suited for long life cycle and high-voltage SC. The downside of this IL is its ESR ten times greater than ACN-based electrolytes, because of the lower conductivity exhibited at 60 °C [89]. Even at room temperature, the electrical resistance is so high to prevent its use in commercial SCs. Moreover, the maximum applicable voltage depends crucially on the residual humidity (even a few ppm of water can break down the working voltage), which would entail considerable constructive problems for an industrial line.
In a recent research on IL, Zarrougui et al. [90] prepared six novel, low-viscosity IL to serve as electrolytes for SCs. All of them were formed with the cation $AMIM^+$ (1-allyl-3-methylimidazolium) and one with a planar anion ($DCA^-$), while the other five anions ($PF_6$, $BF4^-$, $TFSI^-$, $TFA^-$ , and $OTf^-$) with non-polar architectures (see Figure 28).

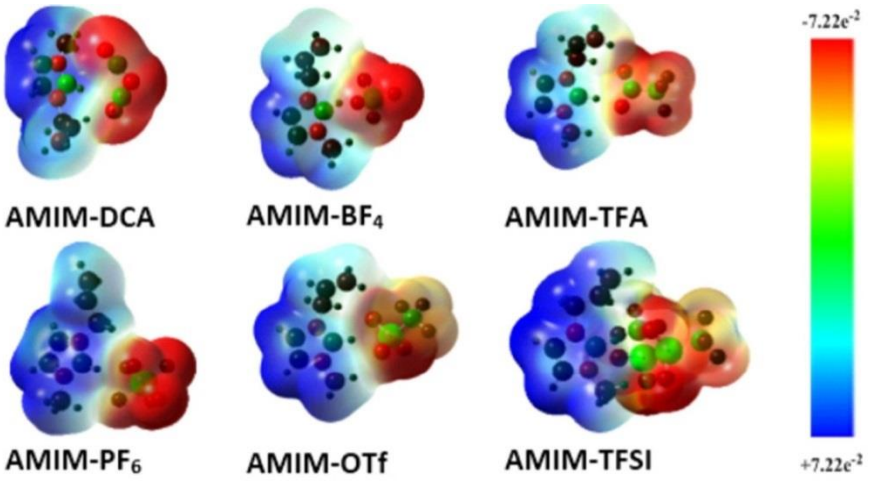


**Figure 28**: Structures of the six ILs with the electrostatic potential map.

The electrochemical system based on those electrolytes showed good performance in terms of specific capacity (135–228 F/g), reasonable energy density (41–115 Wh/kg) and cycling stability up to 1000 cycles (a good value for a IL-based SC, even if it is very low for current commercial SCs).

# 1.5 Applications and future trends

## 1.5.1 Green energy

There is a strong link between green energy, ecology, and SCs. The reasons are multiple and they need to be made explicit, since the previous paragraphs often cited them.
Wind and solar energy sources are intermittent, so also their generated power is intermittent, and it can cause problems. Nonetheless, their plants are becoming widespread, in particular in the form of independent power grids that need an appropriate energy storage devices system. Thus, a storage application to huge grids is important because those infrastructures are designed to last 50+ years. Moreover, these plants need intrinsic low maintenance, but frequent replacement and disposal of exhausted batteries. The last issue would be unmanageable and environmentally harmful because of the dimensions of such infrastructures (MWh or GWh). The use of SCs instead of batteries solves the issue, a main aid for grid infrastructure: they smooth the effect of intermittent power sources (wind or solar) and provide extra power during demand peaks. More precisely, the power grids use new class of storage systems, which includes older and newer technologies. It includes elderly technologies as compressed air energy storage, already installed in the 1980s, and some of the younger gravitational energy storage, which uses giant weights hung in a mineshaft to store and release charge, as in the case of Highview Energy, and Energy Vault recently backed with millions of dollars [91]. These interesting devices are now entering the electricity market with demonstration projects, to prove the technical concept. The constant integration of variable energy sources will require in turn additional storage devices to stabilize the electricity grid, so it needs also SCs.
Finally, SCs have been widely applied to blade pitch control of wind turbines. Their huge power density overwhelms the performance of electrochemical batteries for application like this, where the high power is required for a short time and the maintenance is reduced.

### 1.5.2 Automotive, rail, and industrial

The automotive applications concern cars, buses, trucks, trains, and heavy machines, in the context of the transition to the full electric mobility and hence in the ecology field.
Full electric cars are, at the moment, far impossible target for a pure SC application, as the minimum allowed range of 300–500 km would require about 100 kWh [2]. Commercial SC-based solutions for specific task are available for both Internal Combustion Engine (ICE) and electric cars. They range from aids to jump start or start/stop in ICE models to regenerative braking (KERS) in hybrid and Battery Electric Vehicles (BEVs). On plug-in hybrid bus, braking energy recovery system composed of supercapacitor modules can absorb and store the energy produced at braking and then release the energy during start-up or acceleration, so the vehicle could save fuel consumption and reduce emission more efficiently. If pure electric vehicles only use batteries as power supply, which has relatively short service life and limited number of charging and discharging cycles, the high power required by the vehicle at start-up will have great impact on the battery life. However, if a SC system is integrated with the batteries on the vehicles, it will provide instantaneous high power on starting, on quick accelerations and on strong braking, letting batteries operate in more steady running situations. Summarizing, SCs can provide peak energy for pure electric vehicles, stabilize the voltage, and significantly extend the service life of batteries. They are also a “fit-and-forget” device, a device that need rare or no replacements, because of their very long life cycle.
Many companies are focusing on vehicles equipped with SCs, due the cited wide spectrum of applications, so their aims suggest what the future trends will be. For example, Raghu Das, CEO of IDTechEx, a company dealing with market and technology researches, claims that: “The number of auto makers going for that fit-and-forget, grab more electricity, waste less electricity proposition still increases. The natural extension of this logic is the newly committed adoption of larger supercapacitors for peak-shaving and acceleration boosting at 30-100Wh across the batteries in mild hybrid cars, then full hybrid, then totally replacing the lithium-ion battery if pure electric cars have not destroyed the hybrid car business by then" [91].
A similar consideration concerns also buses and trains. If urban buses and light trains can use SCs at least during charge at route end, then they will charge in 20-50 seconds, and escape battery replacement costs [91]. Figure 29 shows a more updated version of the Ragone plot in Figure 1, highlighting the role that the Battery-Supercapacitor Hybrid (BSH) can have for the urban buses [91].
Even though not yet widely diffused, cranes and machine tools, for the same above-mentioned reason, are other good applications. Moreover, those tools have big potential for energy saving by exploiting at best SC high performance in regenerative braking. Maxwell® (US company, recently acquired by Tesla, which calls “ultracapacitor” its device) supplies SC energy storage for cranes, straddle carriers, stackers, forklifts, and other earth-moving and mining equipment to benefit of the most important features of SCs: their ability to increase the power density of an energy source.

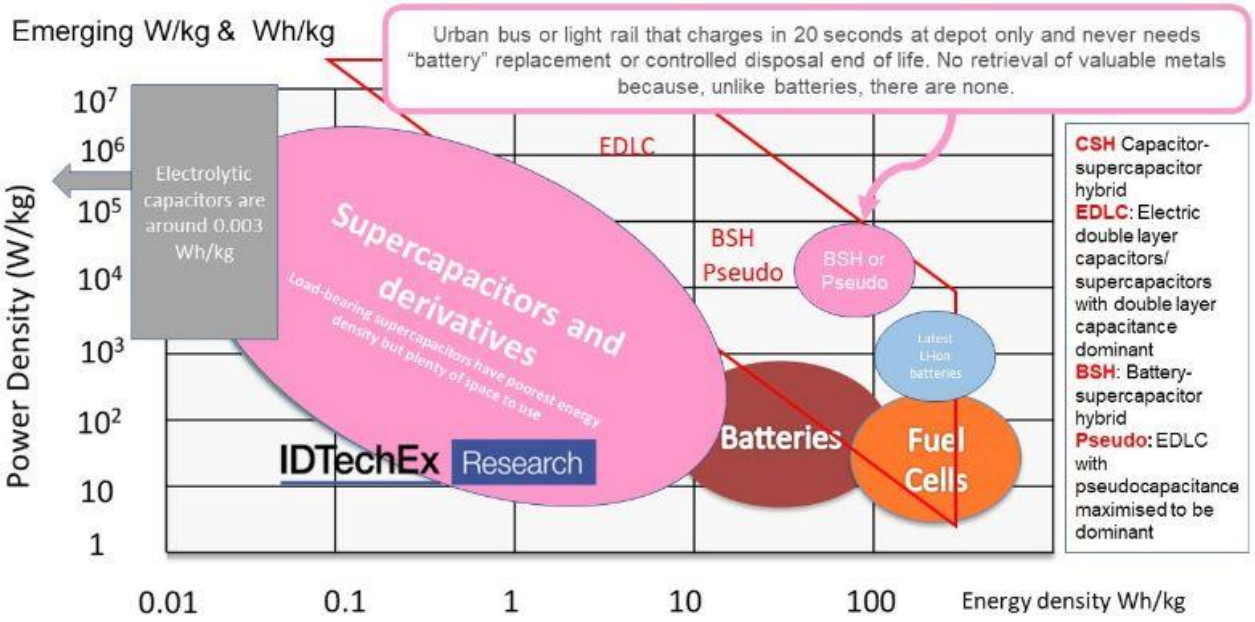


**Figure 29**: Ragone plot of present and arriving energy storage devices, with additional details about electric urban bus with SCs.

### 1.5.3 SC and batteries

The main advantage of batteries towards SCs is their specific energy. In fact, electrochemical batteries are part of vehicles and of every electric portable device (smartphone, computer, remote controls); while SCs have, at the moment, very specific applications. Table 1 shows a list with specific energy and other performance and costs differences between the main kind of batteries and current SCs.

However, compared to batteries and regardless they higher specific power, life cycle and working temperature range, SCs are safer, tolerate overcharge, avoid complex battery management systems. Most are now non-flammable, non-toxic, incur in no costly controlled disposal, and they provide lowest total cost of ownership. They waste 14% less electricity, grab twice the regenerative energy from crane or truck [91]. Dr, Peter Harrop, Chairman of IDTechEx, affirms: "Greatly improved supercapacitors will be multi-billion dollar business, taking 10% of battery sales" [91]. Of course, there are different kinds of "improved SCs" and only a part of them could actually takes a fraction of the battery sales. Graphene-like materials are good candidates to take an important role in this sense.

Raghu Das, CEO of IDTechEx, explains graphene-based SCs trend in this way: "8.75% of supercapacitor manufacturers now offer graphene versions, up from zero ten years ago. 43% of the manufacturers using graphene are in China so they are ahead in numbers, though certainly not in graphene supercapacitor research, much of which is aimed at the massive emerging market for replacing lithium-ion and lead-acid batteries with highest energy density of 100 Wh/kg or more. In research, this is usually achieved by boosted pseudo-capacitance, though some improves the technology of the newly commercial 100 Wh/kg lithium-ion supercapacitors. 33% of supercapacitor material research is graphene-centric, followed by carbon nanotubes then metal organic frameworks" [91].

| | Lead acid | NiCd | NiMH | Li ions | SC |
|---|---|---|---|---|---|
| **Specific Energy (Wh/kg)** | 30–50 | 45–80 | 60–120 | 100–250 | 5 |
| **Number of cycles** | 200–1000 | High | High | 1000–3000 | > 1,000,000 |
| **Temperature range** | R. T. to little more | -50°C to 70°C | R. T. to little more | R. T. to little more | -40°C to 80°C |
| **Cost per cycle ($)** | 0.2 | 0.3 | 0.3 | 0.2 | < 0.001 |
| **Cost per kWh ($)** | 100–200 | 300–600 | 300–600 | 300–1000 | 10,000 |
| **Specific Power (W/kg)** | 10–50 | 20–100 | 20–100 | 500–1000 | 10,000 |

**Table 1**: Comparisons between current energy storage devices performances and costs [2].

This is assisted by the fact that a disproportionate amount of the demand for large supercapacitors is in China, with the Government requesting that all parts of trains, buses, etc. be made in China. However, USA and Europe will follow soon it in next years.

# Chapter 2
# Graphene Oxide

## 2.1 Advantages of Graphene Oxide

Graphene Oxide (GO) is a two-dimensional material of the graphene-like material family. It is like a graphene plane functionalised with oxygen-containing groups as hydroxyl group (–OH), carboxyl group (–COOH), and oxygen in the form of epoxy bridge (–O–). Figure 30 shows a scheme of a GO plane [92].

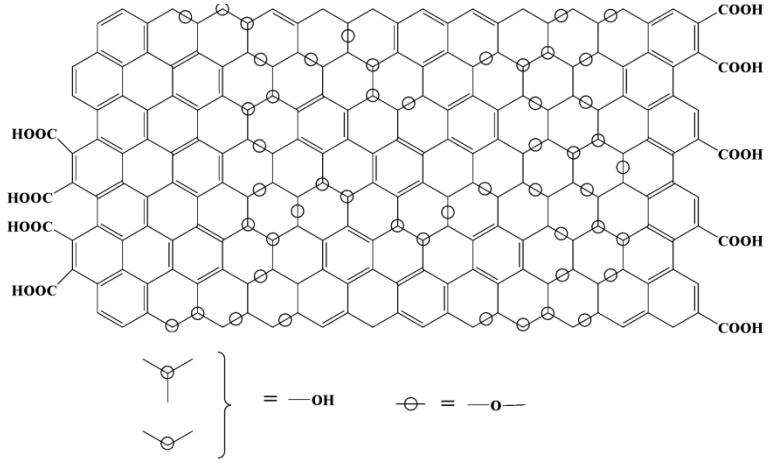


**Figure 30**: Schematic representation of a GO plane.

These groups break the electronic proprieties of graphene making it an insulator. Graphene is the most conductive material having a sheet resistance of 30 Ω/sq [61], while GO has more than 20 MΩ/sq [93]. Since a SC electrode materials has to be porous and conductive, GO is not fitted for this purpose as such. However, GO has two great advantages that justify its central role in this Ph. D. thesis: high workability and ease of conversion into graphene.

**Workability**

Thanks to the oxygen-containing groups, GO is very hydrophilic. GO powder in water makes easily homogeneous aqueous slurry, also called water-based slurry. In general, the use of water as liquid dispersant is not compulsory. Even the use of liquid slurry is not strictly necessary. However, for practical reasons liquid slurry is the most convenient way to make homogeneous mixture with a powder, to perform coating on a substrate, and to control the amount of mass loading. Moreover, liquid slurry allows chemical or thermal manipulations and selections of specific part by a centrifugation.

Not all these operations need strictly water. For example, Graphite Oxide (GtO, the GO precursor) can be dispersed in Propylene Carbonate (PC) [94]. PC, water/acetone mix, water/ethanol mix, N-methyl-2-Pyrrolidone (NMP), and other solvents for graphene-like materials have in common a surface voltage of 40-50 mJ/m$^2$. This surface voltage range is higher than the one of a volatile solvent, as pure acetone (24 mJ/m$^2$), and it is less than water surface voltage (73 mJ/m$^2$) [95]. GtO and GO are hydrophilic, while graphene needs PC, NMP or the other previous dispersants.

Otherwise, graphene can be dispersed in water only using an additive, as the so-called sodium cholate (NaC) [96]. Analogously, Activated Carbon (AC) and Carbon black (CB) also need a surfactant in water, as the Triton X-100 [97]. The advantages of water are obvious, since it is cheap, ecological, and harmless. The addition of a surfactant is a very small complication in a laboratory experiment. Unfortunately, in a scale-up operation a surfactant implicates a further line of production with respect to the main materials, with a non-negligible impact on costs and environment. For these reasons, GO is very helpful thank to its hydrophilic nature.

Finally, there is also a purely scientific advantage of GO in water-based slurry. A slurry is made with a dispersant and with a solid material (as AC, CB or GO) which does not solve in it. A slurry is a dispersion, not a solution. Therefore, while in a solution the limit for homogeneity is only the solubility threshold, in slurry there is always an uncertainty about the solute/dispersant concentration. This uncertainty can be reduced using high dilutions or strong and long mixing. Unfortunately, too high dilutions make hard the slurry coating in making an electrode with at least 1 $mg/cm^2$ of active material on a current collector. This surface density is the minimum one for an EDLC. On the contrary, a strong and long mixing can be even pointless if the dispersed material is hydrophobic. Instead, GO in water does not need high dilutions nor long mixing and the uncertainties about its concentrations are low. For example, if we put 5 mg of GO in 5 mL of water in a Becker, we will obtain a GO slurry with a concentration of 1 mg/mL. On the contrary, with 5 mg of graphene in 5 mL of water, even after a long mixing, the slurry will soon have a concentration gradient from the top to the bottom of the Becker. After that, almost all graphene will drop to the bottom in minutes or hour. In any case, we cannot say that the concentration is 1 mg/mL, and this uncertainty will affect every following steps.

**Conversion into graphene**

GO is often only one of different graphene precursors. The direct conversion of graphite to graphene is apparently more convenient than the double transition from GtO to GO and then from GO to rGO. However, in the contest of electrodes manufacturing this last statement needs important clarifications.

The scaling-up problems of the graphene manufacturing and of a graphene-based electrode are not exactly the same problem. If our purpose is to maximize the graphene production, using a process for good quality material, our main variables concern only production performance. An important performance is the ratio of the produced graphene with respect to the raw material or to the initial concentration (conversion ratio). Another performance is the production rate, i.e. the graphene produced in a unit of time, usually 1 hour. In this case, the simplest manufacturing process is the graphite exfoliation by hydrodynamic forces (through ultrasonication or high shear rate mixing) to graphene flakes. A deep work for this case is the experiment of Paton et al. with a kitchen blender; this work is also a sort of review [98]. Using this very common tool, after 100 minutes of exfoliation they convert the 0.1% of the graphite into graphene. Reusing this method on the non-converted graphite, it reaches a cumulative production yield of the 3% after 30 recycling runs. So, this method wastes a large part of the raw material, but it is an optimization of the production rate. This rate can achieve 5.3 g/h at the large-scale trial of 300 L of graphite slurry with a concentration of 100 g/L. This rate is much higher than the industrial threshold of 0.4 g/h, which is on the contrary too high for the methods that use GtO and GO.

Nonetheless, this performance does not concern the graphene applications, but only its production. For SC electrode applications, graphene needs a binder to adhere on a current collector and something that prevents the re-stacking of the flakes. Due to re-staking, graphene tends to reform

graphite. A manufacturing optimization must concern all these variables. A method based on GO reduction can reach a production rate of only 0.02 g/h, but with a higher conversion ratio. The conversion depends on the effectiveness of the GO reduction, and often with the direct production of a ready-to-test electrode. Especially for this second reason, GO versatility is more helpful then a graphene production method optimized as such.

# 2.2 From Graphite Oxide to Graphene Oxide

Graphite Oxide (GtO) is to Graphene Oxide (GO) as graphite is to graphene. GtO can be considered an Avogadro number of GO planes stacked together as graphite for graphene. Both GtO and GO are electric insulator (GtO conductivity is between 1 and $5 \cdot 10^{-1}$ S/m at a bias voltage of 10 V [99]). GO, as all 2D materials, is a nanomaterial and all its differences with the bulk graphite are deep and they would need a course in Physics of Matter. For our purposes, a characterization of a GtO sample can be performed through three parameters: electrical conductivity (or resistance), C:O mole ratio and manufacturing method.
In the case of a 2D material is not properly correct the concept of resistance ($R$) and specific resistance ($\rho$), because the transport properties are completely different. A 2D material is not simply a very thin material, especially graphene. In fact, graphene discovery deserved a Nobel prize while graphite is the lead of a pencil. In a bulk material, the resistance $R$ depends on the resistivity, and on its size and form as in Equation 24:

$$R = \rho \frac{l}{A} = \rho \frac{l}{w \cdot h} \qquad (24)$$

where $l$ is the length and $A$ the section area, which in the rectangular case is width ($w$) times height ($h$). In a 2D material, $h$ tends to the monolayer height and the charges movement is not "inside" it, but it is a 2D conduction. So, a fitter magnitude is the sheet resistance $R_S$:

$$R_S = \frac{\rho}{h} \qquad (25)$$

where the ratio ($l/w$) in Equation 24 becomes unitary. The unit of measure of $R_S$ is Ohm (Ω), but since also $R$ is measured in Ohm, usually $R_S$ is measured in Ω/sq. "Sq" refers to the resistance of a unitary square, sometime using the symbols Ω/□.
Sheet resistance of GtO and GO is proportional to the O:C mole ratio (or vice versa, conductivity is proportional to C:O mole ratio). O:C mole ratio is the number of moles of the oxygen in all the functional groups of a GtO sample divided by number of moles of all its carbon atoms. For example, if O:C is 0.6, then on average 100 carbon atoms are coupled with 60 oxygen atoms. Sometimes, this ratio is expressed in terms of mass percentage with respect to the whole mass, for example if C is the 40 wt.%, then 1.0 g of GtO powder is made with 0.4 g of carbon atoms. In order to find a relation between these two magnitudes, we call these them in the following way:

$$\begin{cases} \alpha \equiv \dfrac{n_O}{n_C} \\ \beta \equiv \dfrac{m_C}{m_C + m_O} \end{cases} \qquad (26)$$

in which $\alpha$ is the O:C mole ratio and $\beta$ the carbon mass ratio (on the whole sample). The relation between these two ratios is Equation 27 (in two equivalent forms):

$$\beta = \frac{w_C}{w_C + \alpha \cdot w_O} \Leftrightarrow \alpha = \frac{w_C}{w_O} \cdot \frac{1-\beta}{\beta} \qquad (27)$$

where $w_C$ and $w_O$ are the atomic weight of the carbon and oxygen atoms respectively (i.e. 12.0107 g/mol and 15.999 g/mol respectively). For example, if the O:C mole ratio is 0 (no oxygen), then $\beta$ is 1 (100% of the weight is carbon). Instead, if the O:C ratio is 1 (a 1:1 ratio between the two types of atom), then $\beta$ is about 41.4 wt.%, i.e. a mass ratio due to only the different atomic weights. Vice versa, if $\beta$ is 0.5 (half of the total mass), then the O:C mole ratio coincides with the C/O atomic weight ratio (about 0.75).

The O:C mole ratio can be measured in a "direct" way through a Nuclear Magnetic Resonance analysis (NMR). However, NMR needs a fully dehydrate GO sample, which is a hard task. Simpler methods are the comparison between the peaks of the oxygen-containing groups and the crystal lattice of graphite in a NMR or in an X-ray Diffraction analysis (XRD). Another method is a thermogravimetric analysis (TGA), which gives the mass reduction due to the GtO reduction. TGA consists of a furnace with a sensitive scale that can measure the mass changes of a sample during a temperature increment. GtO loses its groups at high temperatures in inert atmosphere, so it losses a part of its mass. For this reason, GTA is an indirect measurement of the O:C ratio thanks to Equation 27. Regardless these characterizations, the higher is the O:C mole ratio, higher is GtO hydrophilic nature and its colour tends more on brown than to black.

The most used graphite oxidation process was formalized by Hummers Jr. and Offeman [100]; now it is called "Hummers method" and it dates back to 1958. In the Hummers method, the oxidation of graphite is accomplished by treating graphite with an almost water-free mixture (i.e., highly concentrated mix) of $H_2SO_4$, $NaNO_3$, and $KMnO_4$. This method requires less than 2 h for completion at temperatures below 45 °C and can be carried out safely. The final C:O ratio is 2.25. However, all three reactions involve the liberation of toxic gas $NO_X$ and/or $ClO_2$.

Some modifications based on the Hummers method have been proposed. Often, a more recent version of this method is used to achieve a higher O:C ratio, in particular the so-called "modified Hummers method" by Kovtyukhova [101]. In this case, a pre-oxidizing procedure is added using $H_2SO_4$, $K_2S_2O_8$, and $P_2O_5$. The C:O ratio of the oxidation product was 1.29, illustrating that this was richer in oxygen than the graphite oxide prepared by the Hummers method.

Sometimes, the graphite oxidation takes place thanks to an "improved Hummers method" by Marcano [102]. By adding $H_3PO_4$ to the formation of graphene oxide nanoribbons (GONRs) from multiwalled carbon nanotubes, it shows that more GONRs were produced with more intact graphitic basal planes. The improved Hummers method, using $KMnO_4$, $H_2SO_4$, and $H_3PO_4$ as the oxidizing agents, avoids the release of $NO_X$ and yields a greater amount of hydrophilic oxidized graphite material compared to the original Hummers method (C:O ratio is 1.43). Due to its simpler protocol and equivalent performance, the improved Hummers method is attractive for preparing GO on a large scale. The differences of these three oxidation methods are summarised in Figure 31.

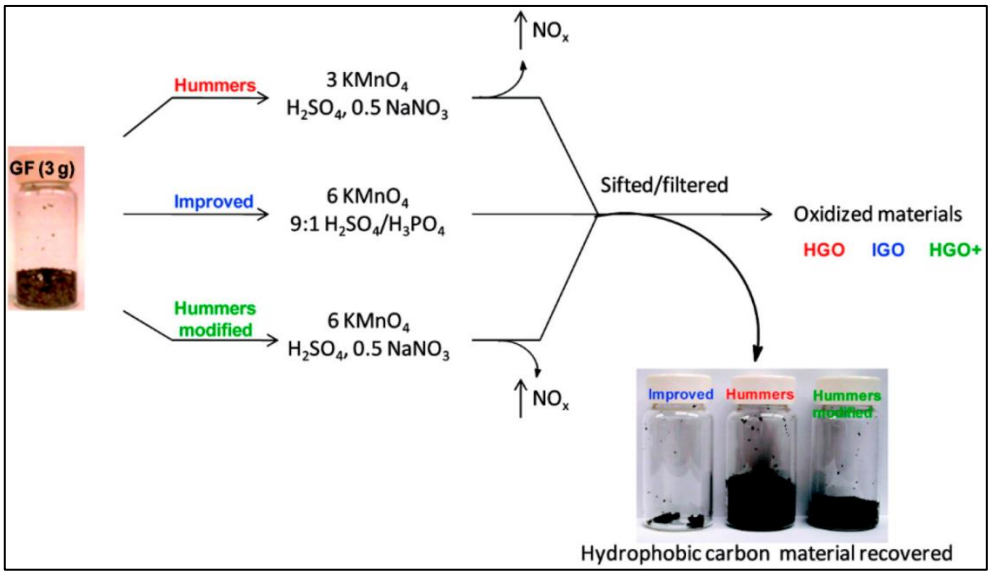


**Figure 31**: Scheme of the three graphite oxidation methods cited in the text.

The conversion of GtO into GO is not a chemical reaction, but it is only an exfoliation (or delamination). Hence, to obtain exfoliation, the following three kind of hydrodynamic forces are sufficient: shear force, cavitation, and collisions. These forces are realized by a high shear rate mixer. This mixer has a static open cylindrical part (stator) and an inner rotating set of blades (rotor) and it can reach till 24,000 rpm (as shown in Figure 32a-b) [103]. Regardless the different performances, also a common kitchen blender can perform this exfoliation, with collision and shear force (Figure 32c) [98]. While collisions are trivial, shear force is the effect of a laminar flow of a liquid at high shear rate; this force can overcome the non-covalent bonds between the GO planes of a GtO particle.

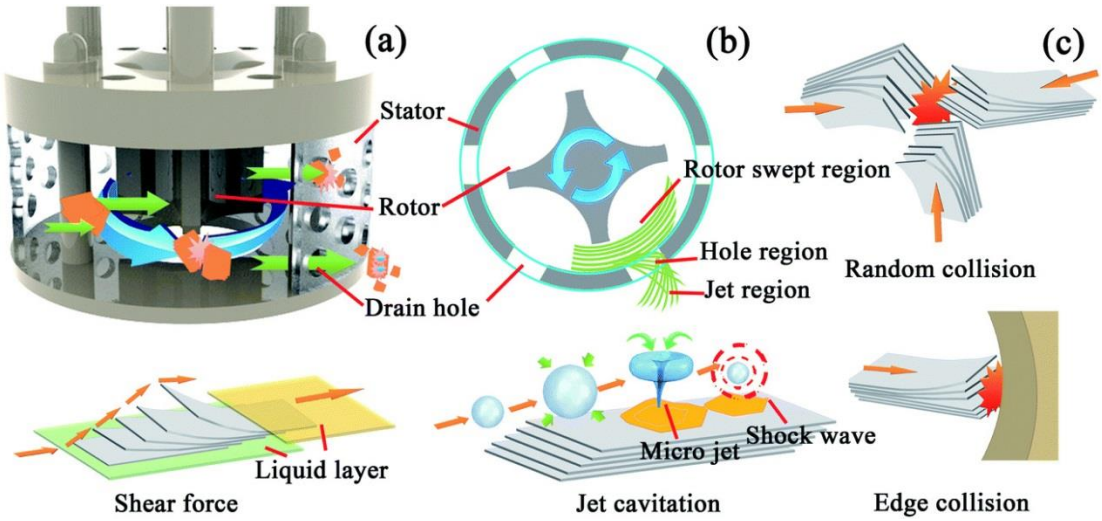


**Figure 32**: Details of the tool and of exfoliation mechanism. (a) drawing of a high shear rate generator; (b) main energy dissipation regions of the high shear mixer (sectional view); (c) schematic representations of shear force, collision, and jet cavitation.

The most powerful mechanism is cavitation. Cavitation phenomenon takes place when in a liquid there is locally a very high pressure, so an air bubble forms, which then implodes. The implosion forms, as first, a micro jet, then it causes a shock wave. This last causes the exfoliation and to obtain

this kind of exfoliation the right tool is a probe sonicator, as shown in Figure 33. In a probe sonicator, a tip generates high power ultrasounds that cause the cavitation phenomenon.

**Figure 33**: Exfoliation of GtO in water-based slurry with a probe sonicator, with freezing water to prevent excessive heating and the help of a magnetic stirrer.

By my direct experience, an exfoliation of GtO powder with O:C mole ratio of 0.6 and particle size in the range 5-50 μm is optimized in the following way [4]:

- using water-based slurry with a GtO/$H_2O$ concentration of 8 mg/mL, or in any case below 12 mg/mL, because above this value the slurry viscosity is too high to make the sonication efficient.
- activating the sonicator with a power of 72 W for 45 minutes.

Compared to usual graphite exfoliation, the second point concerns a minor amount of energy (194 kJ, so less than 1-10 h of sonication with similar power). Moreover, since GtO is hydrophilic, water helps the exfoliation separating formed flakes and avoiding restacking. In fact, even after 1 week or more from the sonication, the GO slurry did not show differences (no sedimentations).

# 2.3 Reduction of Graphene Oxide

The reduced Graphene Oxide (rGO) is not called simply “graphene” even if “rGO” seems redundant. In fact, a substance that oxidises and then reduces should come back in its initial form. Actually, there are many differences between graphene and rGO that need some specifications.
GO formation is like the oxidation of $n$ carbon atoms (in a honeycomb lattice) in a reaction approximatively like the following ($n$ and $m$ are positive integers, with $n >> 2m$):

$$nC + mO_2 \longrightarrow (n-2m)C + (2m)CO \qquad (28)$$

In Equation 28, the oxidation number of both the reagents is 0, but oxygen is the oxidant, and carbon is the reducing agent. In fact, in the product, *(n-2m)* carbon atoms are unchanged, while *2m* carbon atoms grow in oxidation number (+2) by covalent bonds with *2m* oxygen atom (whose oxidation number falls to -2). For this reason, this kind of graphene-like material is called "Graphene Oxide". Equation 28 assumes that the O:C mole ratio in not a perfect 1, which would be the case of every carbon atom coupled with an oxygen one.
If a reduction reaction takes place, it can be described by Equation 29 (*p* is less than *2m*):

$$(n-2m)C + (2m)CO + pR \longrightarrow$$
$$\longrightarrow \quad (n-2m+p)C + (2m-p)CO + pRO \qquad (29)$$

in which *R* is a generic reducing agent that removes *p* oxygen atoms from a GO sample. It is worth noting that Equations 28 and 29 are generalizations that do not respect all the chemistry conservation rules, nor the exact reaction chain of an actual red-ox reaction.
It is perfectly normal that *p* is less than *2m*, which means that not all the oxygen-containing groups are removed. This happens because no chemical reaction with a minimum level of complexity is efficient at 100%. Since at least in a very small part rGO is still oxidized, rGO is not perfect graphene (PG). Of course, the stronger is GO reduction, the closest rGO is to a strictly-speaking-graphene, especially in terms of electrical conductivity and hydrophobic nature. Moreover, the condition that *p* is less than *2m* is not the only difference between rGO and graphene.
When a covalent bond between a carbon atom of the GO lattice and a functional group is broken during a reduction, the honeycomb lattice made is not always restored (as in PG, shown in Figure 34a). In this case, the lattice can locally have or a vacancy (as shown in Figure 34c-d) or a recombination of the carbon atoms that forms new couples with pentagons and heptagons (Figure 34b, the so-called Stone-Wales defect) [104]. In both cases, they are lattice defects that make rGO less conductive than graphene. Finally, the chemical properties of the carbon atom in a graphene plane are different from the ones at its boundary. Oxidation and reduction act like a percolation transition, so oxygen tends to react forming clusters and preferring interfaces [105]. In particular, the plane boundaries are more reactive, so they easily oxidize (or easily oxidize again). For all these reasons, even if different experiments starts with the same GO sample, rGO samples from

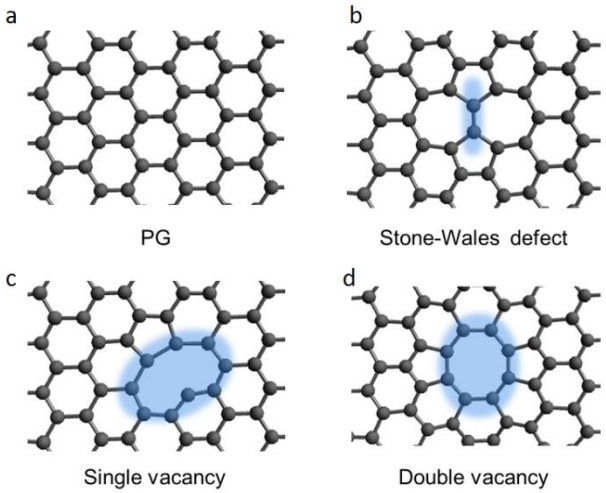


**Figure 34**: Representation of (a) a perfect graphene (PG) plane and of its principal defects (especially in rGO), i.e. (b) Stone-Wales defect, (c) single vacancy and (d) double vacancy.

different oxidation processes can be very different.
Nonetheless, even if rGO is not PG, this situation can be an advantage. In fact, some groups still present after a reduction are a graphene functionalization that helps to prevent the planes from restacking. Moreover, these groups can form non-covalent bonds that can be exploited for different applications [4].
A graphical summary of the descriptions of graphene, GO and rGO is shown in Figure 35a, while Figure 35b shows the whole processing route from graphite to rGO [106]. rGO in Figure 35a-b is not like graphene but it has always some oxygen atoms and vacancies. However, even rGO can have an electrical conductivity higher then GO by many orders of magnitude, according to the proper reduction method.

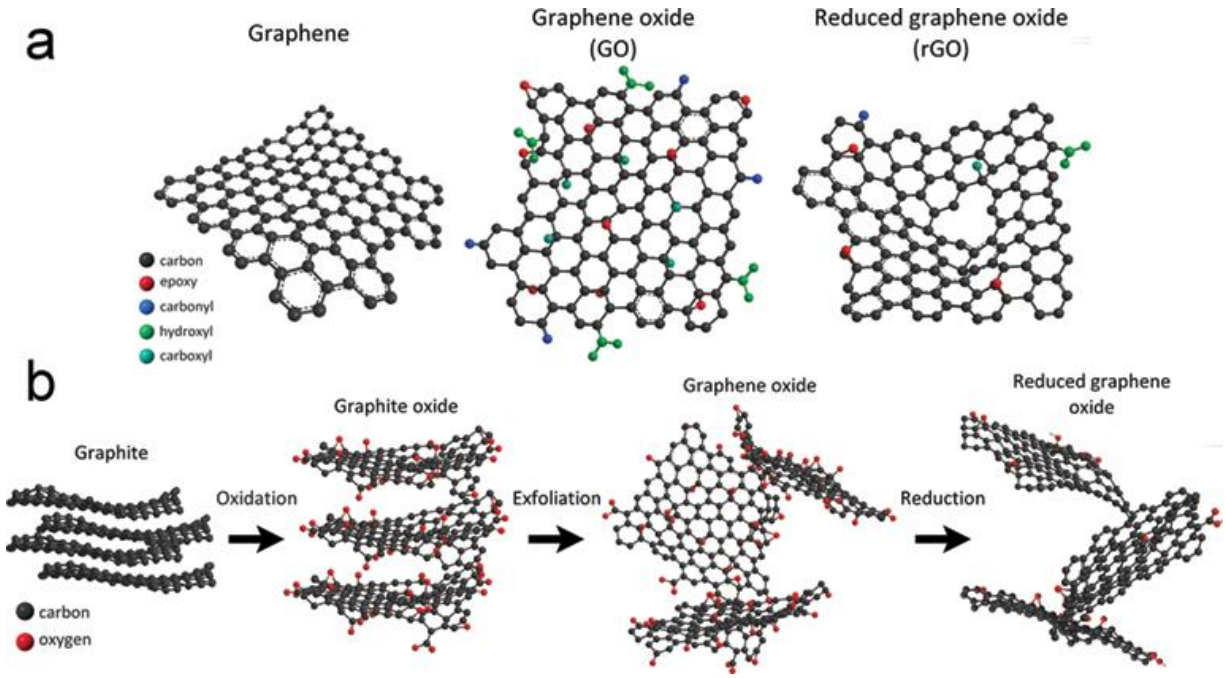


**Figure 35**: (a) schematic representation of PG, GO and rGO; (b) processing route from graphite to rGO as discussed deeply in this thesis, but regardless the specific oxidation and reduction process.

## 2.3.1 Thermal methods

A thermal treatment can reduce a GO sample if it stays under a reducing ambient, i.e. an atmosphere without oxygen. The oxygen absence causes the reduction reaction if GO receives an amount of thermal energy above a given threshold. This threshold depends on the specific parameter of the experiment (temperature, pressure, and time) and on the sample features (mass and level of oxidation). This kind of reduction follows a law like Equation 29, where the reducing agent is not a chemical substance *R* but the heat, while products (apart from rGO) are gases ($CO_2$, $O_2$ and water vapor, depending on the groups on the starting GO).
The thermal methods are relatively simple because they need only specific physical conditions, without using acids or other materials. However, the downsides are substantially two. First, thermal reduction needs specific equipments that are not always scalable. Second, every other material which is mixed with GO must tolerate the same thermal condition during the reduction. In fact, often GO reduction takes place at high temperatures, which can be above the melting point of

materials that couple with graphene-like materials. This is the case of as textiles, glues, or other polymers. To solve these downsides, researchers explored different combination of the thermal treatments parameters. These combinations concern a "standard method" and then additional five methods that touch upon the "extreme cases".

1) A standard method to thermally reduce GO employs relatively low temperatures for long time. In a work about a Propylene Carbonate-based slurry (PC) of GO [94], after 1 h of bath sonication of GtO, the as-exfoliated GO was thermally treated at 150 °C for 12 h in an oil bath. PC is a dispersant for graphene and hence for rGO, while its relatively high boiling point (242 °C) allows the use of a reducing temperature of 150 °C. Immediately after the exfoliation, the slurry looks like in Figure 36a, as a brown-coloured mixture of suspended platelets, while after reduction the mixture becomes black.

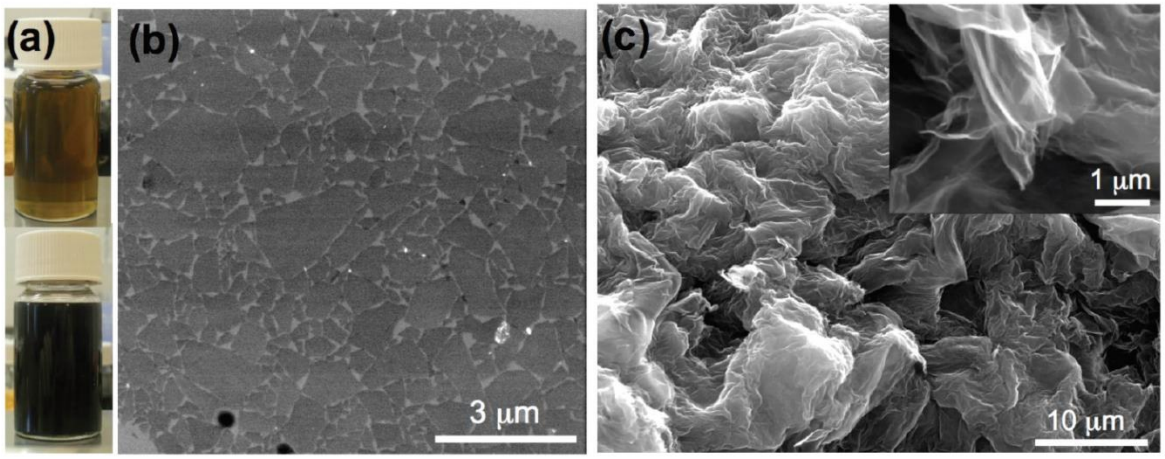


**Figure 36**: (a) Optical images of a graphene oxide suspension in PC (top) before and (bottom) after thermal treatment. (b) SEM image of GO platelets deposited on a Si substrate. (c) SEM image of the rGO powder with a high magnification detail in the inset.

A simple characterization of GO is performed by a Scanning Electron Microscopy (SEM) analysis of a diluted GO slurry dropcasted on a Si substrate (Figure 36b). GO is made with discontinued flakes of about 1 µm size and almost two-dimensional. On the contrary, after reduction, a new SEM image (Figure 36c) shows a continuous, fluffy, and crumpled morphology. Moreover, the high magnification SEM details, in the inset of Figure 36c, shows thin and wrinkled platelets transparent to electrons.
This method is only suited for producing SC with a PC-based electrolyte, it needs long time, and a precedent GtO exfoliation.

2) Strong vacuum condition can perform a direct conversion of GtO powder into rGO at the same temperature of the previous point (150 °C) [22]. A vacuum oven set at -76 cm Hg (-1 atm) and 150 °C for 4 h applies heat (under reducing ambient) to reduce GtO. Vacuum pressure is expressed in a negative value with respect to the atmospheric pressure. At the same time, the heat exfoliates the powder through the gases made during reduction ($CO_2$ and $H_2O$), with the help of the vacuum thrust. In fact, the forces that bind the GO planes of a GtO particle are the Van der Walls ones, as a scheme in Figure 37 explains. Figure 37 also shows a sample before and after this treatment.

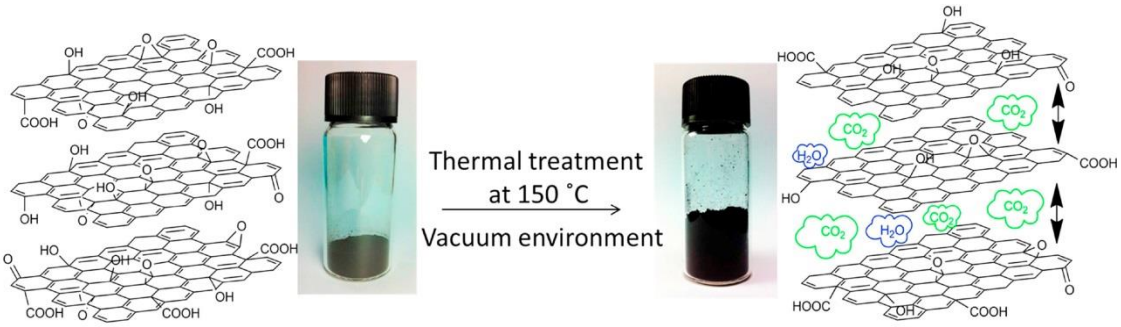


**Figure 37**: Schematic representation of the vacuum-assisted GtO exfoliation and reduction. The oxygen-containing groups create van der Waals forces that can be overcome by the pressure of the gases released as products of the reduction, while the vacuum helps them. The photos also show change in colour (from brown to black) and in density (rGO is less dense than GtO) before and after this thermal method.

The authors of this work claim an estimation of the threshold pressure to exfoliate GtO. This pressure should be at least 1.51 MPa, which can be easily reached by the emitted gases. In fact, the produced $CO_2$ and $H_2O$ have a mass of 44 and 18 g, respectively, for every GtO mole, and their pressure during the treatment is about 7.43 MPa (using the ideal gas law). This methods allows using different electrolytes (their authors choose an Ionic Liquid), but this material needs further step for the electrode manufacturing.

3) A faster GO reduction method exploits a "thermal shock" [107]. It does not need vacuum, but it uses higher temperature (400 °C). The treatment consists in inserting a glass tube containing GO powder into a preheated furnace at 400 °C. The thermal shock occurs in less than just 2 minutes after tube insertion. During this process, as always, the bright yellow powder turns to black and becomes fluffy. Then, the tube is kept in the furnace for additional 2 minutes to ensure completion of the exfoliation process. Finally, the tube cools down naturally, then the sample is collected for further treatments. In fact, even though the rGO had an oxygen content of ~13.7 at% with an O:C ratio of 0.16, it cannot be used as it is. Thus, this rGO is mixed with GO flakes at different ratios to form a self-standing film, as shown in Figure 38a. Usually, the obtained self-standing electrodes , i.e. electrodes which do not need a current collector, are made for producing thin and flexible SCs. Figure 38b shows a SC of this type with a solid-state electrolyte (Figure 38b).

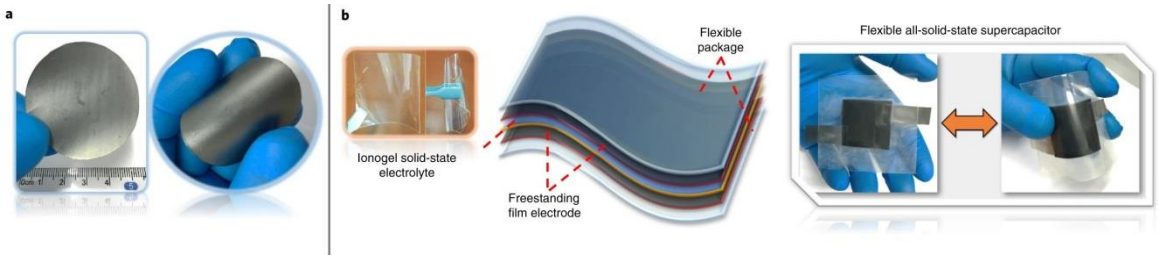


**Figure 38**: (a) GO/rGO electrode film, in which the GO component is reduced in turn with a chemical method. (b) solid electrolyte (ionogel), scheme and photos of the flexible SC made with the GO/rGO film.

Besides this very specific application of the electrode film, the thermal shock is a versatile GO reduction method.

4) A very fast method for a direct conversion from GtO to rGO uses rapid heating in a quartz tube. A heating rate at more than 2000 °C/min is applied under argon atmosphere for about 1 min, until it reaches 1050 °C [108]. Also in this case, GtO powder is exfoliated through the gases produced by the reduction, but this method produces rGO powder with an O:C ratio of 0.10. The effectiveness of elevated temperatures is very intuitive, due to advantages of an excess of heat. In fact, during a thermal reduction part of the heat does not reduces GO but warms up the gases themselves and often dries the dispersant of a GO slurry. At elevated temperatures, heat realizes mainly the reduction and its part involved in the other two processes is negligible. However, such temperature rate needs specific furnace that is not very common nor scalable. Moreover, the most common current collector, aluminium, melts above 660 °C, so this method is not suited for a direct conversion on the current collector.

5) A GO reduction can be performed to directly obtain an electrode; in this case GO is usually in form of slurry, coupled with other electrode materials. This is the case of a work that I co-authored, about water-based slurry with a carbon black and a surfactant [4]. In this slurry, GO was previously exfoliated, and the thermal treatment was performed at 550 °C for 1 h under Ar flow. This method used a medium time and an expensive gas, but rGO formed directly both an electrode and a binder to the current collector.

6) Finally, a variant of the thermal reduction is the photo-thermal reduction through a laser beam [93]. Water-based GtO slurry can be dropcasted on a substrate, dried at ambient condition, then treated with a laser beam (in this case, 788 nm and 5 mW, i.e. weak infrared light). The light locally heats GtO till direct conversion into rGO, obtaining the so-called

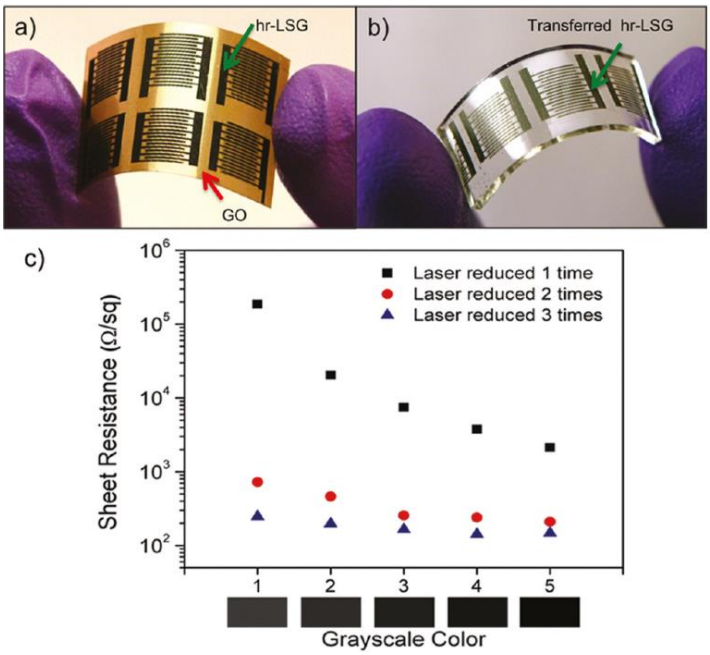


**Figure 39**: (a) Example of hr-LSG in an interdigitated patter in which the (non-reduced) GO is also the separator; (b) the same interdigitated electrodes transferred onto polydimethylsiloxane (PDMS); (c) Sheet resistance of the hr-LSG vs the intensity of the laser beam (the colour is darker, the more intense is the beam) and with the number of treatment on the same point as parameter.

highly reduced Laser Scribed Graphene (hr-LSG). In fact, after laser treatment, O:C falls from 0.38 to 0.036.

This reduction is also very spatially precise, in such a way that a GO slurry can be dried forming a foil and then reduced drawing with the laser an interdigitated pattern like in Figures 39a-b. The insulant channels between the interdigitated electrodes work like a separator, while an electrolyte (usually an ion gel) completes the SC (actually a micro-SC).

If the laser beam has more than 5 mW, the reduction is stronger, and the electrode has a darker gray (Figure 39c). If the same point is laser treated twice or three times, again the reduction is stronger. In Figure 39c the efficacy of the reduction is quantified by the reduction of the sheet resistance, which spans among three orders of magnitudes. This plot also explains the large spectrum of possibilities in the definition of "rGO", since in the same experiment it can have different optical and electrical features.

## 2.3.2 Chemical methods

Since GO reduction is a chemical reaction, the most studied methods to perform it use a chemical reducing agent (or reductant). The scientific literature about GO chemical reduction is so wide that this sub-paragraph cannot be exhaustive. We can suggest a proper review, as the work of Chua and Pomera [109].

According to this review, one of the most powerful reducing agent is hydrazine ($NH_2$-$NH_2$). Through its reduction the C:O ratio rises till 10.3 (at 100 °C for 24 h) or even 11 (at 80 °C in a mix of dimethylformamide and water for 12 h). Even if hydrazine is very often cited in the literature, its use is forbidden in many universities because it is toxic, cancer-causing, and explosive. In fact, it is usually used in rockets and space shuttles.

At the opposite extreme, the more recent literature suggests green reductants, as some sugars or amino acids [18]. Figure 40 shows a graphical summary of the main reductants, in order from the most toxic to the most harmless [18].

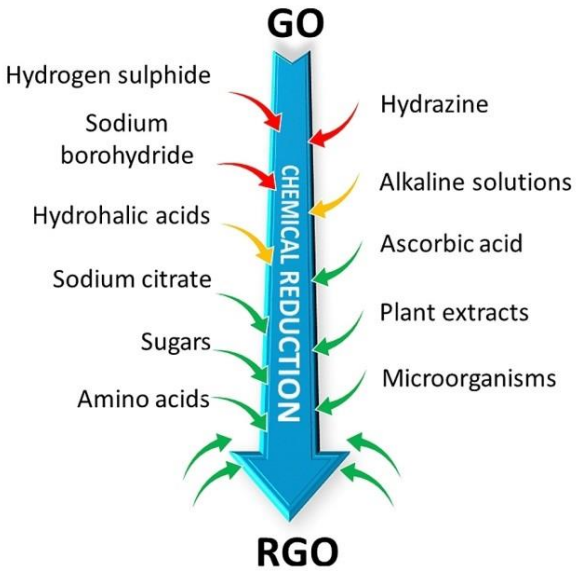


**Figure 40**: Summary of the GO-chemical reduction methods, from most toxic (top, with red arrows) to the less ones (down, with green arrows).

Green reductants can have high performance in terms of C:O ratio (6-11), but not in terms of conductivity (the order of magnitude is about 3000 S/m) [109]. The absence of positive correlation between C:O ratio and conductivity for rGO is normal. High C:O ratio means only that almost all the oxygen-containing groups have been removed. Nonetheless, only if at their place the honeycomb lattice has been restored then the conductivity is high.
A reducing agent which is at the same time simple in its application and whose performances are high is the hydriodic acid (HI). HI entails C:O ratio equal to 12 and conductivity of 29,800 S/m [110]. In this work [110], performed by Pei et al., HI is used on GO films, which are immersed in a water solution or at room temperature for 16 h or at 100 °C (in an oil bath) for 1 h. This method gives better results in the second case. They propose as possible mechanism a twostep reduction by $H^+$ ions produced through HI dissolution. Figure 41 shows these two steps: at first, there is a break of the epoxy bridge by an $H^+$ ion, then a second $H^+$ completes removal of the oxygen.

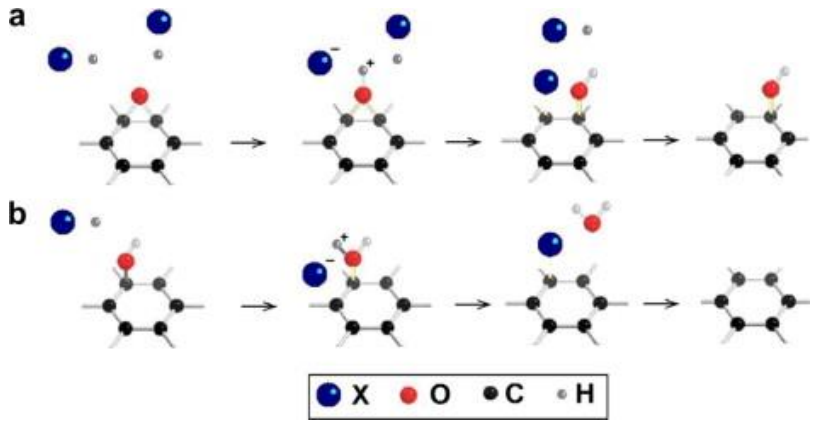


**Figure 41**: Two possible steps for a GO chemical reduction where the X atom can be I or other anions that couple with H. (a) A decoupled $H^+$ breaks an epoxy bridge forming an OH group; then (b) a further $H^+$ completes the reduction forming a $H_2O$ molecule. In both cases, the ion $I^-$ lets its electron.

$I^-$ ions supply the electrons for the formation of a water molecule, but they can sometime functionalize the rGO plane. To prevent this last phenomena, after the reduction the solution needs a substitution of its solvent with pure water.
Within my Ph.D. project, a variant of this reduction with HI was performed. A HI solution (with HI at 57 wt.%, the maximum of the water solubility) was added in a GO slurry at 1 mg/mL (after GtO ultra-sonication in water). The added amount of HI volume was chosen with an approximation by excess. GO was considered with an O:C ratio equal to 1, i.e. with every carbon atoms coupled with an oxygen one, like a lattice of CO molecules. In summary, 1 mg of GO was treated as 1 mg of CO, so the same mole number of HI was added. Even in this case, the reaction took place at room temperature for long time (72 h) or at 100 °C for 1 h. In the second case, a vapor condenser was used, due to water boiling and loss of HI, which is a gas. A first proof of the reduction was the change in colour from brown to dark gray and in the solubility in water. In fact, GO was stable in water, while after HI treatment it quickly sedimented. Moreover, a concentration decrease was also noticed. In fact, the mass of the same volume of a GO slurry was different if extracted before or after the acid treatment. This happened because part of the oxygen become gas, leaving GO that hence loses a non-negligible fraction of its mass. A deeper characterization using a zeta-potential analysis verifies this reduction method. The details of this kind of analysis will be discussed in a following paragraph. Eventually, the analysis confirmed that the experiment performed at 100 °C

gives better reduction yields. These results are unpublished because they still need a deeper characterization. Nonetheless, they should be plausible because they derive from a slight variant of a well-known reduction method.
Our distinction between thermal and chemical reduction methods refer to the possibility of using only heat in the first case (in a reductant ambient). This distinction is not categorical. In fact, the previous cited experiments show that a chemical reductant is helped by high temperature, as for all the endothermic reactions. A proper study about GO chemical reduction, performed with the same reductant at different temperatures, like for instance the work of Jung et al [111], can be very helpful. This work explains that a generalization is not easily possible. However, they define *k* as the velocity of a chemical reaction, i.e. the number of mole of a reagent that becomes product in a unit of time. The dependence of *k* from temperature follows the law of Equation 30:

$$k = Ae^{-\frac{E_a}{RT}} \qquad (30)$$

In this equation, *A* is the so-called "pre-exponential factor", *T* is the absolute temperature (in K), *R* is the universal constant of ideal gas, and $E_a$ is the activation energy. Since *R* is a constant while *T* is our variable, only *A* should be an experimental parameter. $E_a$ is the cost in energy to form/decompose the C-O bond in a GO sample, thus $E_a$ depends only on the material. In the case of the work of Jung et al., $E_a$ is 32-37 kcal/mol for a single-layer GO platelet. The method was a thermal reduction under vacuum. For another reduction method, there is a different *A*, while for a different GO sample (for number of layer, oxidation level and other details) there is a different $E_a$. When an analogous study for the determination of the parameters of Equation 30 is not possible, the alternative could be an optimization study. In this approach, possible guidelines are the maximum tolerable temperature by materials coupled with GO, and the maximum time to make a reduction method scalable [5].

# 2.4 Analysis of GO and rGO

The GO quality and the effectiveness of its reduction can be characterized by many analyses. Main results for all the cited materials are the thickness of their particles and their oxidation level. When GO is studied by itself, as for example for biotechnological applications [3], these results verify the oxidation of GtO, GO and GtO exfoliation. When GO is reduced, then these analysis concern the efficacy of a reduction method by comparisons with GtO or GO. This paragraph devotes particular attention to the analysis techniques used for the published work of its author [3, 5].

## 2.4.1 Optical methods

Some information about a GO sample derives simply by looking at a water-based slurry, as already said. GO is brown or dark brown and stable in water, while rGO is dark gray or black and hydrophobic (as shown in Figure 36a, 37 and 39a). Sometimes, also the difference between GtO and GO is visible in a qualitative manner at first glance, as shown in Figure 42. During an experiment about a GO application [3], a water-based slurry of GtO of the *TOB co.* was ultrasonicated for half an hour. Resulting GO was centrifuged (3500 rpm for 10 minutes) to separate

the supernatant part from the subnatant one. Three test tubes show GtO (before ultrasonication) and GO (after), see Figure 42. There was no apparent difference between supernatant and subnatant part. On the contrary, both last two samples are homogenously dispersed in water, while GtO sedimented.

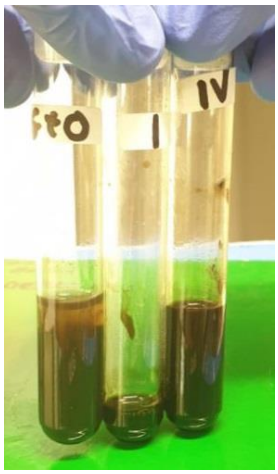


**Figure 42**: water-based slurry of GtO (8 mg/mL) and of the supernatant (I) and subnatant (IV) part of GO, i.e. the first sample after ultrasonication and centrifugation.

GO reduction was also verifiable noting a mass reduction. This observation holds only in very preliminary way and only with big samples (grams or tens of mL). A quantitative discussion needs a more objective analysis. In the case of optical methods, this kind of analysis includes Scanning Electron Microscopy, Transmission Electron Microscope, Ultraviolet-Visible spectroscopy, and X-Ray Diffraction. They give information about exfoliation and some collateral effect of reduction. Besides that, Raman Spectroscopy gives these and further information, so it deserves a separate section.

**Scanning Electron Microscopy and Transmission Electron Microscopy**

Scanning electron microscopy (SEM) and Transmission Electron microscopy (TEM) give images which show morphological features of a GO or rGO sample. SEM and TEM can verify their planarity or the opposite. In fact, Figures 36b-c show a clear opposition between GO and rGO, since the former is in form of planar platelets while the latter is fluffy and crumpled. The planarity of GO is intuitive, since GO is like a graphene with some oxygen bonded to it. Instead, the reasons for different morphology of rGO are the following two:

1) during a reduction, the oxygen-containing groups become gases, so they must go away passing through the rGO flakes. This emission often takes place in an abrupt way, especially in thermal methods. These gases spread the flakes making the material untidier.
2) when functional groups are close together on a GO plane, a reduction can create or strengthen a fold of the plane. Such folds stay bent after reduction, because vacancies form at the place of the groups. This mechanism gives rGO a different morphology compared to the graphene one. Figure 43 shows a model that explains this phenomenon [108].

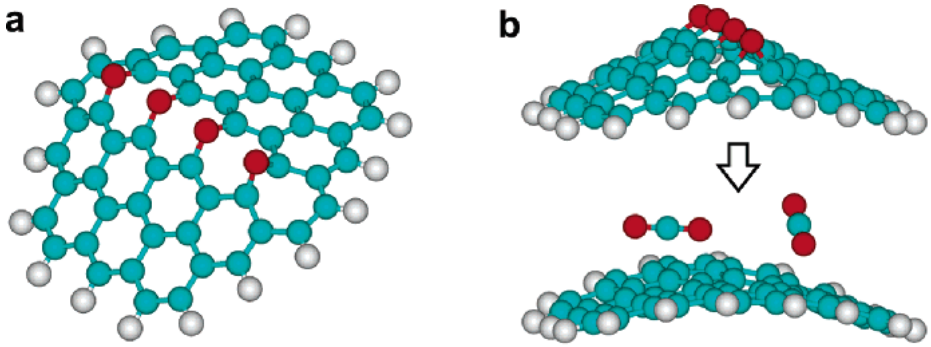


**Figure 43**: (a) model of a bent GO plane due to a line of epoxy bridges; (b) lateral view of the figure and formation of a bent rGO plane after epoxy bridges removal.

TEM images can show a more subtle difference between GO and rGO at high magnifications. Since rGO has a higher crystallinity, when two or a few more layers are close together the electron beam of TEM can produce an interference patter called "Moiré fringe". Moiré fringes look like straight lines on the flakes, as shown in Figure 44 [112]. These lines lack on a GO TEM image.

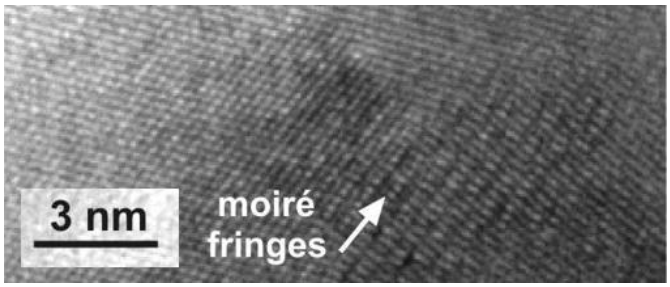


**Figure 44**: TEM image of a few-layers graphene sample with visible Moiré fringes.

**Ultraviolet-Visible spectroscopy**

Ultraviolet-Visible spectroscopy (UV-Vis) uses a light beam between 200 and 800 nm (so in the UV-Vis wavelength) to measure the absorbance of a material dispersed in a solvent. A plot of the absorbance vs beam wavelength gives a method to verify oxidation or reduction. In the next three figures this method will be applied in the case of graphite or graphene-like material particles

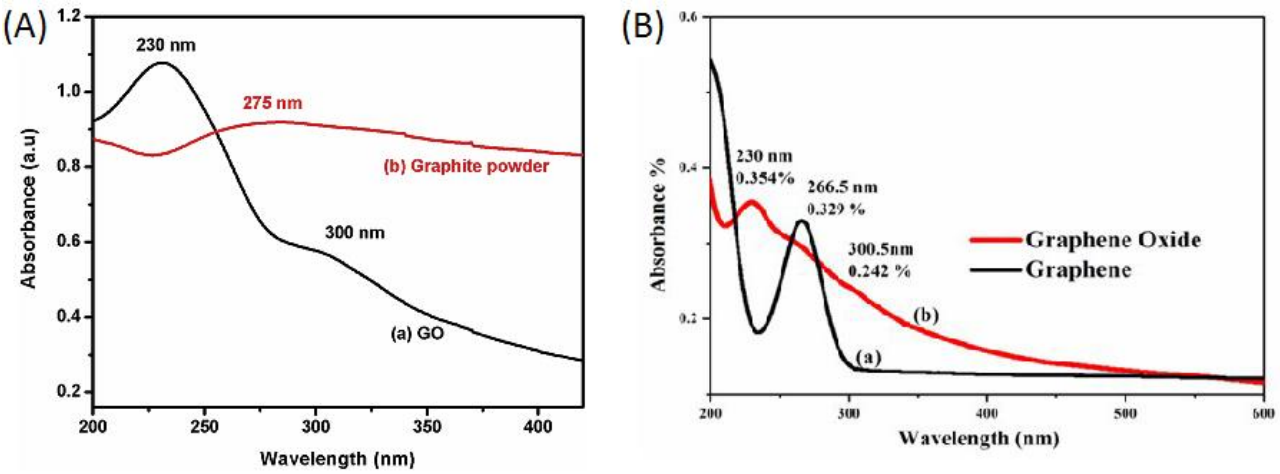


**Figure 45**: (A) UV-Vis spectrum of (a) GO and (b) graphite powder in water, with the wavelength of the respective peaks; (B) same type of plot for (a) graphene/rGO and (b) GO with also the absorbance percentages of their peaks.

dispersed in water. In the case of graphite, an UV-Vis spectrum shows a curve with only a low peak at 275 nm. After graphite oxidation, this plot shows a clear peak at 230 nm, with also a small shoulder at 300 nm, as shown in Figure 45A [113]. This analysis is the same for GtO and GO.
When GO is reduced, there is a peak at 266.5 nm and a growing trend for wavelengths going under the lower limit of 200 nm, as shown in Figure 45B [114].
In a work, whose I am a co-author [3], after GtO exfoliation by ultrasonication in water (8 mg/mL), a GO sample was diluted till a concentration of 600 g/mL and then tested with an UV-Vis analysis (Figure 46). Since both the raw data and the plot show a peak at 230 nm, this analysis confirmed the successfully GO preparation in view of its applications, even without further treatments.

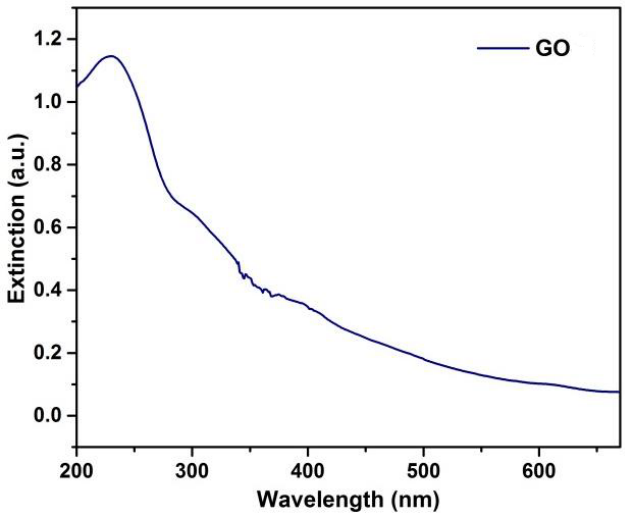


**Figure 46**: UV-Vis spectrum of a GO water-based slurry (600 µg/mL) with a peak at 230 nm.

An UV-Vis spectrum can be used also for the determination of very low concentrations (under 1 mg/mL) for the so-called "optical concentration determination". For high concentrations, a standard method is the measurement by a chemical scale of the mass of a dropcasted sample with known volume. The mass weighted after sample drying is the mass of the powder, while mass difference with respect to the sample before drying it the solvent one. This method in not applicable for low concentrations, which derive from a selection inside a GO sample. In fact, even after a GtO or graphite exfoliation in a liquid dispersant, a selection of the better-exfoliated flakes of graphene or of GO can be compulsory. Centrifugation and collection of the supernatant part of a test tube with a graphene or GO sample allow this selection [98]. In these cases, the optical method for the concentration determination is an application of the Beer-Lambert law (Equation 31) [115]:

$$A = \varepsilon_\lambda c l \qquad (31)$$

In Equation 31, $A$ is the absorbance of a sample analysed by an UV-Vis, $\varepsilon_\lambda$ is its absorption coefficient, which depends on the used wavelength. For this reason, this law is used with a specific wavelength, for example a peak one. Finally, $c$ is the concentration, and $l$ is the optical path (usually the depth of a cuvette). The absorption coefficient is measured by the absorbance of a set of known concentrations (using the same $l$ and $\lambda$, both known), then by fitting the results. Using Equation 31 to draw a straight line with $c$ as independent variable, the fit has $A/l$ as dependent variable and $\varepsilon_\lambda$ is the angular coefficient. Finally, a last UV-Vis test is performed on the sample with unknown concentration to use again Equation 31.

**X-ray diffraction**

X-ray diffraction analysis (XRD) determines the atomic and molecular structure of a crystal, whose crystalline structure causes a beam of incident X-rays to diffract into many specific directions. XRD applies Bragg's law of diffraction (Equation 32) by measuring the angles and intensities of X-rays diffracted beams [116]:

$$d = \frac{\lambda}{2 \sin \theta} \qquad (32)$$

In Equation 32, $d$ is the lattice separation, $\lambda$ is the X-rays wavelength and $\theta$ the diffraction angle. The result of a XRD is a spectrum of beams intensity (in arbitrary unit) in function of the angle $2\theta$ (°). From this spectrum, the mean positions of the atoms in the crystal can be determined, as well as their chemical bonds, their crystallographic disorder, and various other information. Usually, XRD peaks are labelled by the triplets of indices that define reference planes ideally crossing a lattice (the so-called Miller's indices).

In an analogous way, XRD analysis can be used to estimate crystallite size $L$, using the Scherrer's Equation (Equation 33) [117]:

$$L = \frac{K\lambda}{B \cos \varphi} \qquad (33)$$

In Equation 33, $\lambda$ is the radiation wavelength, $K$ is a shape factor, $B$ is the line broadening at half-maximum intensity of the peak, and $\varphi$ is the corresponding scattering angle. Equation 33 can be used for two main crystallite dimensions, which are the stacking height $L_C$ and the crystallite lateral size $L_A$, as explained in Figure 47 [118]. They can be estimated from, respectively, the (002) peak, using a shape factor of 0.89, and the (100) peak, with a shape factor of 1.84 [118].

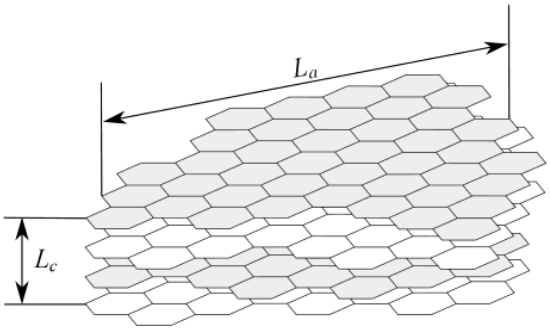


**Figure 47**: Schematic representation of a graphite-like particle with stacking height $L_C$ and lateral size $L_A$.

XRD analysis can verify a graphite oxidation, a GtO exfoliation into GO and a GO reduction. In the first case, graphite XRD spectrum shows a peak at 30.87 °, on the (002) plane, which decreases with graphite oxidation, as shown in Figure 48 [119]. The (002) peak in graphite corresponds to an interlayer distance of 0.3363 nm. After graphite oxidation, in GtO spectrum there is also a peak at 13.18 °, on the (001) plane, which corresponds to an interlayer distance of 0.7795 nm. In fact, the oxygen functional groups reduce long-distance order, so the (002) peak and the other peaks of graphite (above 45°) disappear. At the same time, the spacing between close layers grows for the same reason.

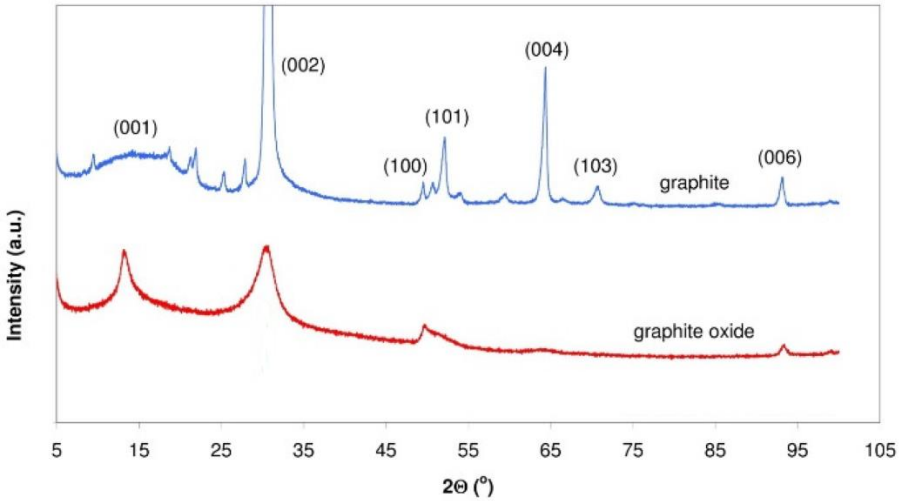


**Figure 48**: XRD spectra of graphite (blue) and GtO (red).

Thanks to an exfoliation process, in a GO sample this interlayer distance is even wider so, according to Equation 32, the (001) peak shifts to a lower angle (11.8 °), as shown in Figure 49a [120]. Figure 49a shows also that this peak is almost the only one, since GO is a two-dimensional material.

With reduction of GO, the ordered crystal structure is restored. This is verified by the reappearance of the (002) diffraction peak at 25.5 ° and disappearance of the diffraction peak (001), as shown in Figure 49b. In the transition from GO to rGO, interlayer distance reduces again if compared to GO one, as a consequence of the oxygen functional groups removal.

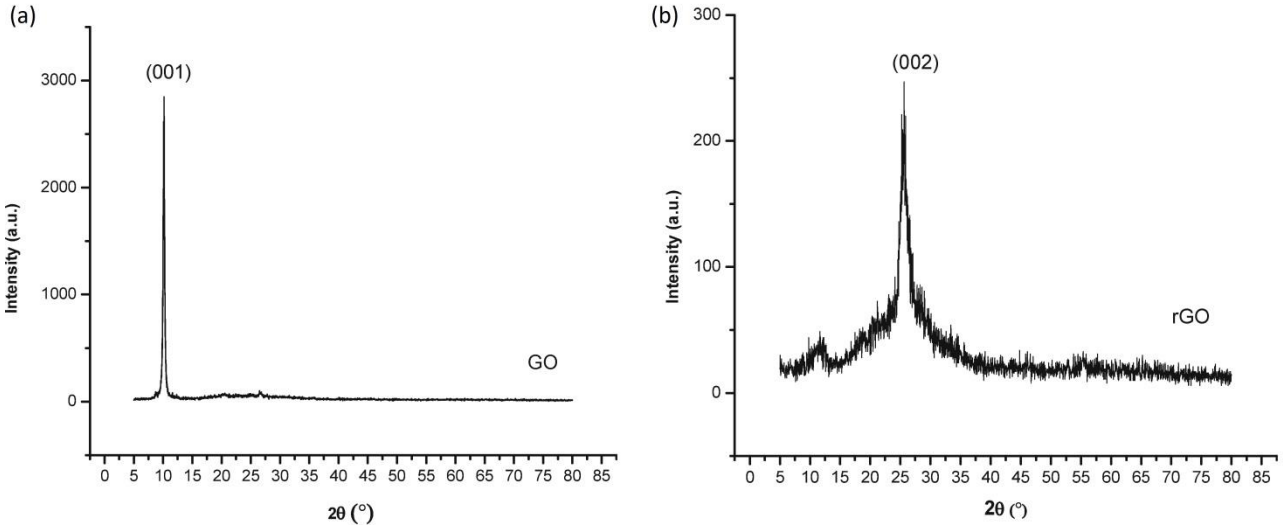


**Figure 49**: XRD spectra of (a) GO and (b) rGO.

## 2.4.2 Raman spectroscopy

Raman spectroscopy (RS) performs material determinations like UV-Vis and XRD, but in a more univocal way. In fact, RS is based on scattering of a monochromatic laser beam, measuring the intensity and the frequency of the light scattered from the material according to molecular

vibrational energetic levels of the last. The result is that in addition to material determination, RS can quantify its disorder, and in our case, also its number of layers.

A Raman spectrum shows the intensity of the scattered light (in arbitrary unit) in function of its wave number $\lambda^{-1}$ ($cm^{-1}$). RS interpretations use mainly the following relation between wave number, frequency $v$, and energy $E$ of scattered light and energetic levels:

$$E = hv = h\,c/\lambda \qquad (34)$$

In Equation 34, "$h$" is the Planck's constant and $c$ light velocity in void. Since RS measures a change in wave number, then in RS graphs the independent variable is usually called "Raman shift". If not diversely stated, all the values of this paragraph refer to RS performed with laser beam with wavelength of 514 nm.

In the case of graphite, GtO, and graphene-like materials, RS analysis studies mainly three bands or modes:

1) G band, which is close to 1580 $cm^{-1}$. This band is associated to the inplane vibration of the $sp^2$ bonds of the carbon atoms, so it is like a "graphitization level indicator".
2) D band, which is near to 1350 $cm^{-1}$. This band refers to $sp^3$ out-of-plane breathing mode in presence of defects of the carbon lattice, so of the material disorder.
3) 2D or G' band, which is about 2700 $cm^{-1}$. This band is the second order of zone boundary phonons (the overtone of D band), and it is related to the stacking nature of graphene-like materials, so to the number of layers.

In the Raman spectrum of graphite shown in Figure 50a, we find the aforementioned D and G modes [121]. After graphite oxidation (GtO) and then its exfoliation (GO), both modes become wider and increase their intensity (Figure 50b-c). More precisely, both position and FWHM (Full Width at half maximum) of G band increase with the oxidation level [122]. At the same time, the well-defined peak of 2D band in the pure graphite spectrum (Figure 50a) undergoes changes in the others spectra. 2D peak goes out of shape in GtO (Figure 50b) and even disappears in GO (Figure 50c). The changes of 2D band in GtO are related to considerable defects in the graphene sheet, produced by oxidation. In GO, 2D peak reduces with respect to GtO one due to reduction of number of layers (see also Figure 51).

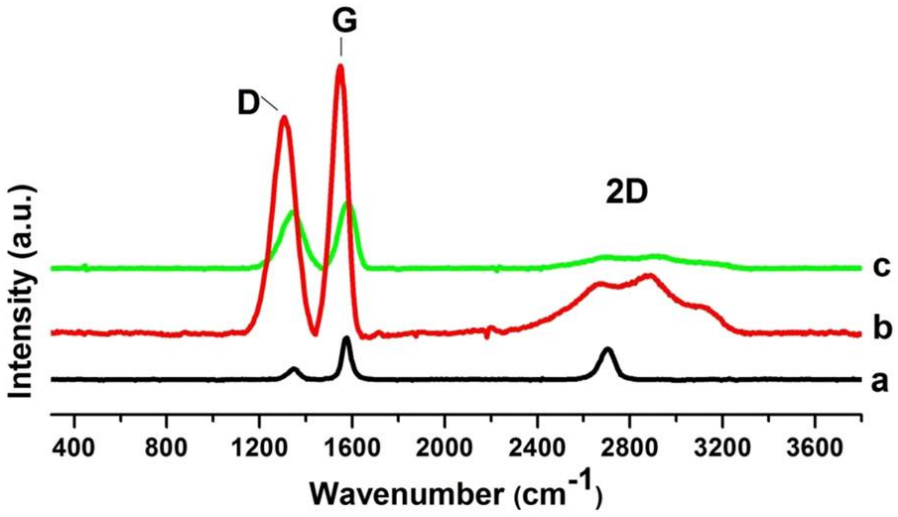


**Figure 50**: Raman spectra of (a) graphite, (b) GtO and (c) GO.

Assuming the same oxidation level, the number of layers on GO has a linear relationship with G band intensity, as shown in Figure 51 [123]. In fact, as the number of layers grows, GO tends to GtO, as shown in Figure 50b.

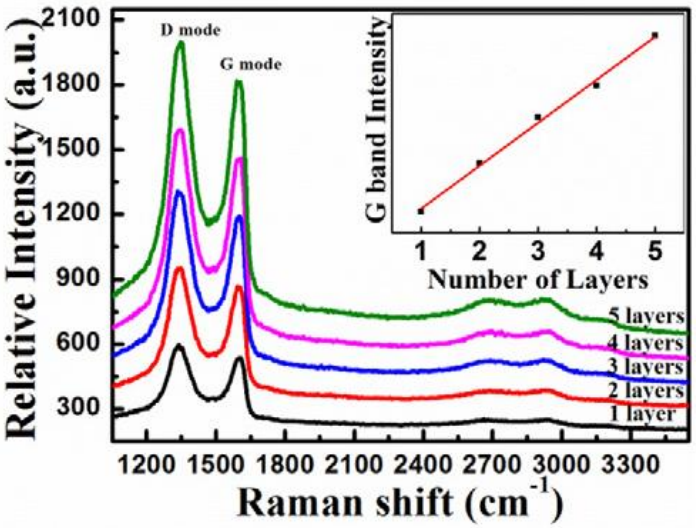


**Figure 51**: Raman spectra of GO with 1-5 layers. In the insert, a plot of G band intensity correlated with the number of layers (Raman wavelength is 532 nm).

RS gives account of GO reduction observing G peak position and the intensities ratio between D and G band, as shown in Figure 52 [124]. After GO reduction, the D band peak position remains unchanged in rGO spectrum with respect to the GO one. On the contrary, the G band peak of rGO downshifts (from 1597 $cm^{-1}$ to 1587 $cm^{-1}$), because rGO partially restores the hexagonal network of carbon atoms. However, there are defects (vacancies and impurities) due to reduction, so the D band intensity is higher in the rGO case. In the example of Figure 52, the relative peak intensity $I_D/I_G$ grows from 0.91 to 0.97.

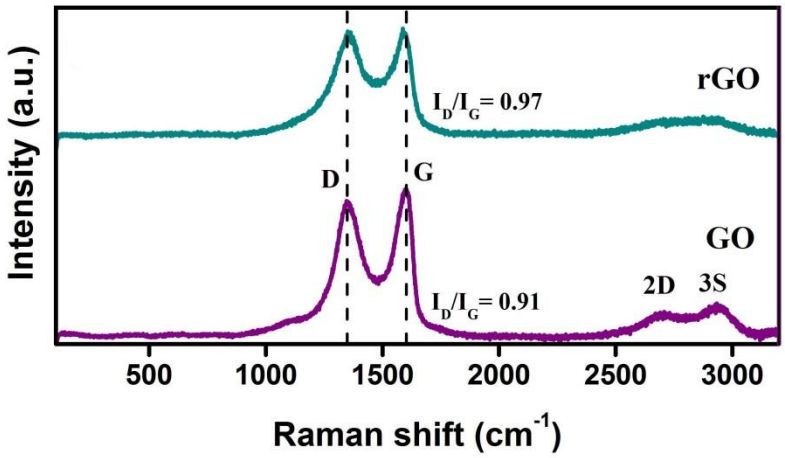


**Figure 52**: Raman spectra of GO and rGO with their $I_D/I_G$ ratios.

The criterions based on relative peak intensities are "universal" for every RS apparatus, but the peak positions ones can depend on the laser wavelength. In the case of graphene and rGO, the differences of the RSs with different laser wavelengths are shown in Figure 53 [125]. Figure 53 shows that the G band position is almost the same. In fact, G peak corresponds to the so-called "simple resonance process", in which the outgoing photon energy depends only on the momentum of the excited

electron. According to Equation 34, also the outgoing wave number depends only on this momentum, so it cannot change with different laser wavelength. On the contrary, in the 2D band there is also a contribution of a phonon, because it is a second order band. This phenomenon is called "double or triple resonance process". In this case, the energy of the phonon is proportional to

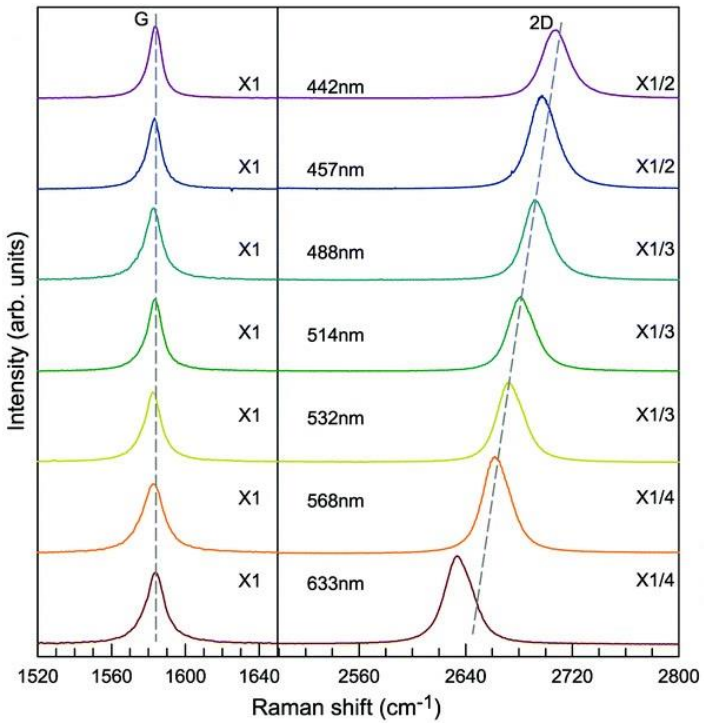


**Figure 53**: Raman spectra of graphene using different Raman wavelengths.

the incoming photon energy. Therefore, if the laser wavelength decreases, its beam energy increases and hence the Raman shift from the 2D peak increase, in accordance with Equation 34.
Using only the G peak position, there are many experimental relationship between it and the number of layers of a graphene or rGO sample. For instance, the work of Weing et al. suggests a relatively simple formula for a few-layer-graphene [126]:

$$\omega_G = 1581.6 + \frac{11}{(1 + n^{1.6})} \qquad (35)$$

In Equation 35, $\omega_G$ is in $cm^{-1}$ and $n$ is the number of layers. According to this law, G peak should be at 1587.94 $cm^{-1}$ for monolayer graphene, at 1584.16 $cm^{-1}$ for the bilayer graphene, and at 1581.72 $cm^{-1}$ for the three-layer graphene.
Graphene/rGO number of layers has others effects on a Raman plot, as shown in Figure 54 [127]. Figure 54 shows more precisely that:

1) G peak position shifts to lower values as $n$ increases (in accordance to Equation 35);

2) G peak intensity almost does not change from 19 to "infinite" layers (graphite);

3) 2D peak is higher than G one for $n < 5$, so this is another helpful criterion to distinguish high quality graphene/rGO from other graphene-like materials;

4) the second order peak at 3250 $cm^{-1}$ is independent by *n*. For this reason, a Raman spectrum usually stops at lower wave numbers.

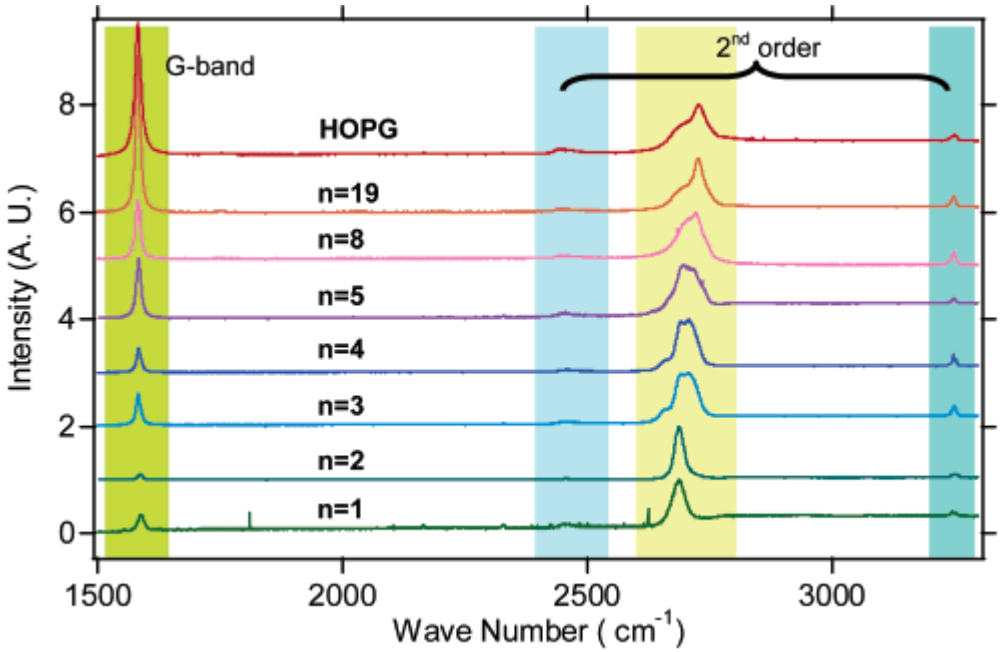


**Figure 54**: Raman spectra of graphene with different numbers of layers (*n*) and in the case of highly oriented pyrolytic graphite (HOPG, a high quality graphite).

## 2.4.3 Zeta potential

The ζ-potential or Zeta Potential (ZP) analysis is a very fast method to estimate the surface charge of a particle through polarization of its functional groups. ZP needs only a diluted solution or slurry with known features (solvent, temperature, and pH), and a few-minutes-test with an apparatus called "Zetasizer".

The particles dispersed in a solvent can be granules, polymers, or flakes of a 2D material. In a ZP test, an electric field causes a motion of charged/polarised particles and the formation of a charged layer, consisting of solvent molecules, around them. ZP is the voltage difference (usually expressed in mV) between this layer and the outer part of the solvent. The surface which ideally separates this two part of the solution is called "slipping plane".

Figure 55 shows that the slipping plane should not be confused with the charged surface of the particles nor with the closest ions/molecules layer, the so-called "Stern layer" [128]. The Stern layer is an electric double layer of the same kind of the EDLC one, and it forms in a different zone with respect to the slipping plane.

Each of these three surfaces has its potential, but a Zetasizer measures only the one on the slipping plane. Therefore,, ZP is not properly the potential of the surface charge, but often is the only way to measure it. Moreover, the sign of ZP is the same of the surface charge, so a ZP analysis helps to determine the kind of groups on a functionalized material.

Actually, a Zetasizer measures the electrophoretic mobility ($\mu$) of the particles, which is by definition the ratio between the velocity of the particle due to an electric field and the electric field itself.

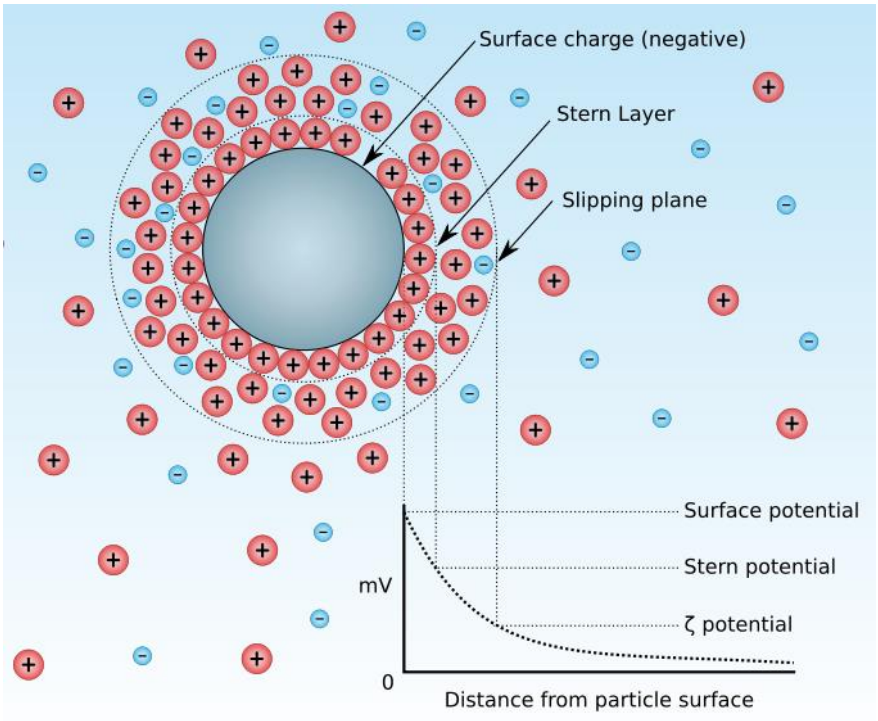


**Figure 55**: Schematic representation of the surface charge, the Stern layer, and the slipping plane of a spherical particle in an aqueous solution.

From the $\mu$ measurement, this analysis provides a measurement of the ζ-potential through the Henry's equation [129], within the so-called Huckle and Smoluchowsky limits [130]:

$$\mu = \frac{2\varepsilon\zeta f(ka)}{3\eta} \qquad (36)$$

In Equation 36, $\varepsilon$ is the dielectric constant of the solvent, $\eta$ is its viscosity and *f(ka)* is a function that varies smoothly from 1.0 to 1.5 in the cited limits. More precisely, the Smoluchowsky limits are the following two:

1) A sufficiently thin double layer, i.e. its Debye length $\lambda_D$ must be smaller than the particle radius *a*. The Debye length definition is given by Equation 37:

$$\lambda_D = \frac{1}{k} = \sqrt{\frac{\varepsilon_r \varepsilon_0 k_B T}{2z^2 e^2 n}} \qquad (37)$$

   where $\varepsilon_r$ and $\varepsilon_0$ are relative and vacuum dielectric constant respectively, $k_B$ is the Boltzmann constant, *T* is the absolute temperature, *z* is the ion charge, *e* is the elemental charge, and *n* is the ion density. Since *k* is the reciprocal of the Debye length, then this limit is followed when *ka* is much higher than 1.

2) The conductivity of the solvent near the particle is negligible, i.e. the so-called "surface conductivity" is very low compared with the bulk one.

The first limit is valid for water-based slurry and with particles size above 100 nm. The second one is valid for non-heavy-charged particles. Both these limits are not violated in the GO water-based slurry used in the works that I co-authored [3, 5].
Given these conditions, ZP is proportional to the surface charge of a particle, for instance the functional groups of a 2D-material. Consequently, ZP indirectly measures the stability behaviour of a solution, for instance the hydro-solubility of a powder. The higher is the surface charge and its ZP, the higher is the material stability in a solvent. Table 2 shows the predicted stability according to five ZP ranges [131].

| Zeta potential (mV) | Stability behaviour |
|---|---|
| 0 to ±5 | Rapid coagulation or flocculation |
| ±10 to ±30 | Incipient instability |
| ±30 to ±40 | Moderate stability |
| ±40 to ±60 | Good stability |
| > 61 | Excellent stability |

**Table 2**: Interpretations of a ZP measurement in terms of stability of particle/molecules in a solvent.

According to Table 2, if ZP is under 5 mV (in modulus), then the particles in the solution will sediment quickly, while at growing ZP the sedimentation time protracts till the complete stability.

**Example of a ZP analysis application in biotechnology**
Two-dimensional materials have (among many) also biotechnological application due to their functionalization, chemical reactivity, high specific surface, and sharps edges. In particular, in some work as the one I co-authored with Singh et al., $MoS_2$ and GO are used against bacteria and viruses. More precisely, this work studies the interaction between these 2D-materials and a gram-negative bacterium, Escherichia coli, and a gram-positive bacterium, Staphylococcus aureus. Moreover, these two types of nanomaterials were employed to study their antiviral action toward the Herpes simplex virus type-1 (HSV-1).
GO was obtained by ultrasonication of GtO (TOB®) in water. Among the varied fabrication methods, ultrasonication serves as an effective exfoliation strategy to obtain clean and defect free nano-sheets . Other methods failed due to low yield, expensive and complex equipment, and intense use of harsh chemicals. In this experiment, GO concentration in water was 600 and 1400 mg/mL to study and reveal different antibacterial and antiviral effect. In our case, at lower concentration this action was stronger. However, GO dispersion was centrifuged at 3500 rpm for 30 min, then its sediment was re-dispersed in a smaller volume, separating the supernatant for further characterizations. This procedure was performed three times, with a centrifugal force of 2000g, 3000g, and 3500g, respectively.
Table 3 shows ZP results for the GO samples obtained with the three centrifugal forces. All of three ZP values are to be considered high because, according to Table 2, they are in the range of good stability. This happens because GO flakes are rich of negative charges due to oxygen-containing groups, and this situation is more evident in the sample obtained with the 3500g centrifugal force. Probably, the highest centrifugal force selected the most exfoliated flakes, which could expose to water the inner layers. Instead, in the other two samples functional groups were more hidden, involving a lower ZP.

| Centrifugal force (g) | Zeta Potential (mV) |
|---|---|
| 2000g | -48.0 |
| 3000g | -47.5 |
| 3500g | -49.4 |

**Table 3**: ZP of GO water-based slurry after three different centrifugations.

In the case of antibacterial action, ZP has also an explicit role in the chemical-physical interaction between a 2D-material and the cellular membrane. Results in bacteria samples were interpreted in terms of the Derjaguin–Landau–Verwey–Overbeek (DLVO) theory [132], which essentially accounts for the Liftshitz-van der Waals ($V_{LW}$) and the electrostatic interactions ($V_{EL}$). The latter interaction is due to the surface charge of bacteria on one hand and of nano-sheets on the other, as shown in Equations 38-39.

$$V_{tot} = V_{EL} + V_{LW} \tag{38}$$

$$V_{EL} = \frac{\pi a_1 a_2 (\zeta_1^2 + \zeta_1^2)}{a_1 + a_2} \left\{ \frac{2\zeta_1 \zeta_2}{\zeta_1^2 + \zeta_2^2} \ln\left[\frac{1+exp(-kd)}{1-exp(-kd)}\right] + \ln[1 - exp(-2kd)] \right\} \tag{39}$$

In Equation 38, $V_{LW}$ depends only on the bacteria and on nano-sheets radius ($a_1$ and $a_2$ respectively), and on their separation distance $d$. Instead, $V_{EL}$ depends also on ZPs of their respective surfaces ($\zeta_1$ and $\zeta_2$). Finally, in Equation 39, $k$ is the reciprocal of Debye length (as in Equation 37). The stronger is $V_{EL}$, due to ZPs, the higher is the possibility that a GO nano-sheets touches and breaks a bacterium membrane.

This is the case of $MoS_2$, while GO has a weak effect on bacteria. However, interpretations of this weak effect in interesting because they are strongly interdisciplinary. More precisely, $V_{EL}$ is predominantly repulsive due to surface charges of the same sign. In addition, salt and nutrients contained in the bacterium growth medium reduced the GO stability and lead to fast aggregation. Finally, due to the so-called wrapping effect, bacteria tend to be insulated from the external environment.

On the contrary, GO has a strong antiviral action on HSV-1, especially in the case of the "co-treatment". Co-treatment is the adding of GO slurry and viruses' strain to a host cellular culture (Vero cells) at the same time. In this case, GO-virus interactions are not descripted by Equation 38, because it is not applicable to a complex system where there are present also host cells.

Of course, the direct interaction between GO nano-sheets and viruses is still responsible for the antiviral action. In addition, the work of Singh et al. ascribes this intense action also to the presence of specific glycoproteins on the Vero cell membrane like Lectin. Lectin has high affinity with negative groups present on the surface of GO in solution, given the presence of electrolytes, such as carboxyl and epoxy [133]. This implies a high probability for both GO nano-sheets and HSV-1 to meet and be in touch in correspondence of the Vero cell membrane. This adding mechanism reinforced the effect of the GO-viruses direct interaction.

This kind of affinity has de facto a binding behaviour, which makes GO helpful also for SC electrode applications, as deeply described in next chapter.

# Chapter 3
# GO in SC manufacturing

## 3.1 Introduction

In this work, the fabrication of binder-free electrodes for EDLCs based on a nanocomposite of CB and rGO is proposed. A water-based slurry of CB and GO was coated to a current collector and then thermally treated through a tube furnace to promote the reduction of GO. rGO formation was confirmed by chemicophysical characterization, while its ability to behave as an "active binder" was proven by electrochemical characterization. We define "active binder" a material that ensures adhesion of the nanocomposite to the substrate with direct contribution to the final performance. In addition, an innovative use of a current collector consisting of high-quality rGO paper was also tested. It derives from a high-temperature thermal treatment of GO and allows advantages with respect to conventional Al collectors. Our rGO paper has an improved adhesion with the nanocomposite active material under examination, thanks to the materials' affinity. Moreover, it has a reduced weight, thanks to a density of 1.2 g/cm$^3$ against 2.7 g/cm$^3$ of aluminium, with a comparable thickness.
A SC made with these materials showed a high specific power of 32.1 kW/kg and a corresponding specific energy of 8.8 Wh/kg at a current of 1 A/g. It had also a cheap, environmental-friendly, and scalable process. These promising performances make the "all-graphene-based" device described in this study a valuable candidate for the future of SCs.

## 3.2 Experimental apparatus

### 3.2.1 Materials and Methods

**Materials**
CB powder (Black Pearls 2000®) was supplied by Cabot Corporation. Triton X-100® (TX100, laboratory grade), regenerated cellulose membrane filters (Whatman RC55), triethylmethyl ammonium tetrafluoroborate (TEMA-TFB), and acetonitrile (ACN) were purchased from Sigma-Aldrich. GtO powder was acquired from Xiamen TOB New Energy Technology Co. Deionized water (MilliQ®), was used throughout all the experiments. All chemicals were used as received without further purification.

**Preparation of the CB/GO Slurry**
CB powder (1660 mg) was added in a solution of water (13 mL) and TX100 (46.5 μL, corresponding to 50 mg) and mixed as follows: 30 min of bath ultrasonication and subsequently 2 h of magnetic stirring. The resulting CB suspension in water was then mixed with a GO dispersion of 166 mg in 20.75 mL of water (8 mg/mL) with the aid of an ultrasonicating bath. A homogeneous

CB/GO (34 mg/mL) slurry was finally obtained after 12 h of further mixing using a magnetic stirrer. A CB-only slurry (34 mg/mL), without the addition of GO, was also prepared as reference. TX100 was mixed in water with the aid of a sonicating bath in a specific amount so that its concentration with respect to CB is 3 wt.%. The GO dispersion was obtained by ultrasonic exfoliation of 1200 mg of GtO in 150 mL of water. The used GO volume was fixed in order to achieve a mass ratio of GO/CB = 1:10.

**Preparation of the rGO Paper**

The rGO paper used as the current collector was prepared following the procedure described in a previous work of Rapisarda and Meo [134]. Briefly, a GO solution in water was cast on a polyethylene terephthalate film and dried for 24 h in ambient conditions to obtain a GO film. The latter was annealed at a temperature of 1300 °C for 3 h under argon (Ar) atmosphere. Finally, rGO was rolled to obtain a freestanding paper, with a controlled thickness of 40 μm and density of 1.2 $g/cm^3$.

**Fabrication of the EDLCs**

The as-prepared slurries were coated on all the surface of the rGO paper serving as the current collector using the doctor blade technique. A common Al sheet was also used as the current collector for reference purpose. The coated collectors were heated at 550 °C for 1 h under an Ar atmosphere. Finally, squares of 1 cm side were cut and used as electrodes of the supercapacitor samples. Nonthermally treated electrodes, subjected instead to ambient drying for 24 h after the coating, were used as reference.

For each SC sample, two identical electrodes were laminated in the sandwich configuration using the regenerated cellulose membrane as the separator, and a 1.5 M solution of TEMATFB in ACN as the electrolyte (0.5 mL). Heat-sealable laminating pouches and copper tape for more robust electrical connections to the current collector were used to finish the fabrication. We specify that the conductive tape is never in contact with the active material. A total of six different samples were manufactured and tested; the adopted nomenclature and the relative features are summarized in Table 4. A summarizing scheme of the whole manufacturing process is shown in Figure 56.

| Sample[a] | Slurry composition | Current collector | Thermal treatment |
|---|---|---|---|
| CB_Al_AD | CB-only in TX100/$H_2O$ | Al | No |
| CB_Al_TT | CB-only in TX100/$H_2O$ | Al | Yes |
| CB_Gr_TT | CB-only in TX100/$H_2O$ | rGO paper | Yes |
| CB/GO_Al_AD | CB/GO in TX100/$H_2O$ | Al | No |
| CB/GO_Al_TT | CB/GO in TX100/$H_2O$ | Al | Yes |
| CB/GO_Gr_TT | CB/GO in TX100/$H_2O$ | rGO paper | Yes |

**Table 4**: Summary of Fabricated and Tested Supercapacitor Samples with the Adopted Nomenclature.
[a]AD is the abbreviation of ambient drying, TT is the abbreviation of thermally treated, and Gr is used to refer to the rGO paper used as the current collector.

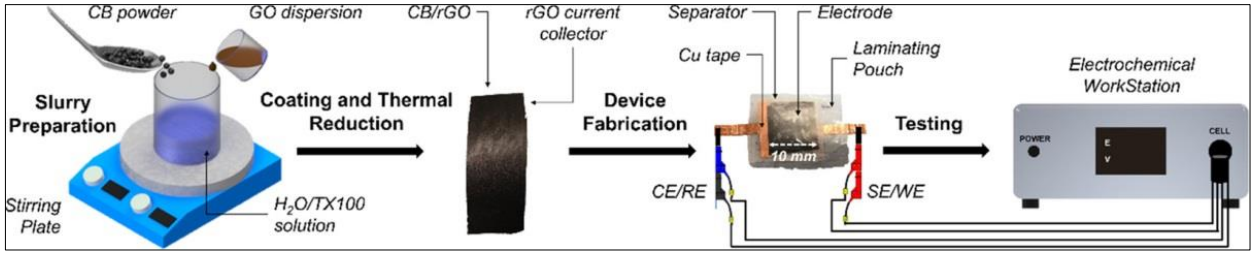


**Figure 56**: Scheme of the manufacturing process showing also electrochemical workstation. CB/rGO indicates the carbonaceous nanocomposite used as the active material. CE, RE, SE, and WE indicate, respectively, the counter electrode, reference electrode, sensing electrode, and working electrode.

**Chemicophysical Characterization**

For the ease of analysis, powder samples of the coating were scratched from the current collectors of each electrode type, and then treated depending on the characterization technique. Transmission electron microscopy (TEM, by a JEOL JEM-2100Plus) and field emission scanning electron microscopy (FE-SEM, by a JEOL JSM-6301F FESEM) were used to characterize the structures and morphologies of particles and agglomerates constituting the carbonaceous nanocomposite. The powdered samples were subsequently sonicated and drop-cast on TEM grids for TEM analysis. The same samples were instead deposited on conductive carbon adhesive tabs for FE-SEM analysis. The obtained images from TEM and FESEM were then processed with the software ImageJ to extrapolate the features of interest.

Chemical properties were investigated through Raman spectroscopy (inVia Raman microscope from Renishaw) using a 523 nm laser source (IK Series He-Cd). The crystalline structures of the blends were analysed with transmission powder X-ray diffractometry (XRD, by a STOE STADI P) using a Cu Kα generator with 1.54 Å of wavelength. The powdered samples were deposited on regular microscope slides for Raman spectral collection, while they were mounted on specific sample holders for XRD measurements. XRD data were processed to obtain the interplanar spacing $d$ in crystal lattices, following Bragg's law (Equation 32 [116]), and to estimate crystallite size $L$, using the Scherrer equation (Equation 33 [117]).

**Electrochemical Characterization**

The electrochemical performances of SC samples fabricated as previously described were evaluated using a μAUTOLAB-BIII-FRA2 electrochemical workstation from Metrohm in a two-electrode configuration (Figure 56). Two different techniques were exploited, all using the aforementioned workstation: Cyclic Voltammetry (CV) and Galvanostatic Cycles (GCs).

CV curves were analysed, and the following formula (Equation 40, equivalent to Equation 11) was applied to calculate cell capacitances $C$

$$C = \frac{1}{2\nu\Delta\mathrm{E}} \oint I(E)dE = [F] \qquad (40)$$

In Equation 40, $\nu$ is the scan rate, ranging from 50 to 500 mV/s in current tests, $E$ is the potential expressed in volts (V) with $\Delta E$ as the potential excursion, between −2.7 and 2.7 V. This excursion spans both voltage signs to better verify the EDLC behaviours of the samples, as previously discussed. The integral represents the area inside the curve, which corresponds to the charge accumulated in the SC; the factor of 0.5 normalizes the repeated area of the CV curve due to

opposite sign scans. The specific capacitance $C_S$ was obtained by Equation 12 (which we report for the convenience of the reader):

$$C_S = 4 \times \frac{C}{m} = [F/g] \qquad (12)$$

In Equation 12, *C* is the capacitance of the cell measured in the electrochemical tests, while *m* is the mass of both electrodes expressed in grams (g). The multiplier of 4 adjusts the capacitance of the cell and the combined mass of two electrodes to the capacitance and mass of a single electrode. In fact, each electrode has a mass of *m/2* and an EDLC is equivalent to two SCs in series with half the capacitance of a single electrode. Moreover, the specific energy $U_S$ was determined with the following (Equation 41)

$$U_S = \frac{1}{2 \times 3.6 \times m} C E_{MAX}^2 = [Wh/kg] \qquad (41)$$

where $E_{MAX}$ is the maximum applied potential and 3.6 is a factor used for the conversion of the energy from joule to watt-hour (Wh), and of the mass from grams to kilograms (kg).
GC curves were obtained using specific currents of 0.5, 1, 2, and 4 A/g, in the potential range of 0−2.70 V. The capacitance was also calculated through the discharging part of the GC curves by the formula (Equation 42)

$$C = \frac{I \Delta t}{\Delta E} = [F] \qquad (42)$$

where *I* is the constant discharging current, expressed in ampere, and $\Delta t$ is the time interval, in seconds, of the discharge potential range $\Delta E$. The specific capacitance and the specific energy were determined as in the previous case. Furthermore, the *ESR* can be estimated through the initial voltage drop $\delta E$ of the GC according to the following formula (Equation 43)

$$ESR = \frac{\delta \mathrm{E}}{2I} = [\Omega] \qquad (43)$$

The specific power $P_S$ of SCs depends on the ESR and the maximum reached voltage during the test, as expressed in Equation 44

$$P_S = \frac{E_{MAX}^2}{4 \times ESR \times m} = [kW/kg\ ] \qquad (44)$$

The specific capacitance and the specific energy from the two tests just described usually show comparable results. However, thanks to the extra information obtainable from GCs, a Ragone plot can also be drawn to picture the trade-off between the energy and power of electrical energy storage devices.

### 3.2.2 Slurry Optimization

All the proportions in our slurries and details of mixing have specific explanations, which can be helpful to divulge. The following observations concern qualitative information which do not derive

from a chemicophysical or electrochemical analysis, but they are a compulsory step. In fact, without homogeneous slurry or without a good coating, a SC fabrication is not possible.
In the case of the CB-based slurry prepared before GO adding, its concentration was about 128 mg/mL, then it became 34 mg/mL after GO adding. The first concentration was particularly high in order to make the final CB/GO slurry still highly concentrated. Then, last concentration results from the following trade-off:

1) lower concentrations allow easier mixing and homogeneity, but at the same time after coating on aluminium and slurry drying, the electrode has a lot of vacancies, crack, and fragile points.
2) Higher concentrations need a too long mixing or at least stronger mixing. In the second case, heating due to mixing makes part of the solvent evaporate, so the final concentration becomes unknown.

The best way to solve this trade-off was the choice of both high concentrations and long mixing (2 h for CB-only and 12 h for CB/GO).
Even the TX100/CB mass ratio derives from a trade-off problem, because at ratio below our 3 wt.%, no improvements in homogeneity and workability were observed, while over 3 wt.% the final electrode could have too many impurities due to non-evaporated TX100 particles. In fact, TX100 is helpful only to mix charcoal in water, otherwise mixing is too much hard. However, TX100 has no role in an electrode and it is not even a conductive material.
GtO concentration has only an upper limit of 12 mg/mL, at least in our experiments. Going from this value to higher concentrations, the probe sonicator becomes inefficient in GtO exfoliation. On the contrary, lower concentrations are enough for our purposes and they can eventually be diluted if a value under our 8 mg/mL is fitter to other experiments. For example, in the work of Singh et al. [3], the lower GO concentration was 0.600 mg/mL.
Finally, GO/CB mass ratio of 0.10 was the same of the work of Galhena et al. [27], more precisely, it was the best one between it, its reciprocal (10), and the 1:1 ratio. In both our and Galhena's work, this choice derives not only from a matter of best performance. In our works, rGO is mainly an active binder that helps CB to bind to a current collector. Higher GO/CB ratios can be pointless for our purposes, while there are already other works in which this specific kind rGO is the only electrode material [94].

### 3.2.3 Aluminium pre-treatment

Sometimes, an aluminium foil is not already suited for working as current collector for a carbon-based electrode. This problem exists because aluminium tends to oxidise due to oxygen in the air, then an oxygen layer forms on its surface making difficult the adhesion of a carbon or rGO layer.
In our case, aluminium pre-treatment avoids this problem, in particular using a 3% sulfuric acid bath for 2 minutes. Nonetheless, a just treated aluminium foil is even more reactive than a not pre-treated foil, so to not make worst this problem coating must take place as soon as possible. For the same reason, the solution for the etching should not have more than a 3% of $H_2SO_4$ nor should last more than few minutes. Etching should be even better if in the same solution there is also fluoridric acid, but only at 80 ppm.

Regardless aluminium etching, an aluminium foil must be as flat as possible; otherwise even a homogeneous water-based slurry will not produce a homogeneous coating. In our case, this problem was solved by literally ironing aluminium foils before etching.

# 3.3 Results and discussions

**Chemicophysical Characterization**

The carbon nanocomposite was obtained, as described in detail in the paragraph "Material and methods", with a GO-aided homogenization of CB particles previously suspended in a mixture of water and TX100. This nanocomposite behaves as the active material of the SC electrodes proposed in this research work. The carbonaceous coatings obtained after drying of the slurries were physically and chemically characterized to investigate the effects of GO in the resulting nanocomposite. The characterizations also confirm the reduction of GO to rGO, when thermal treatment on the CB/GO slurry was applied.

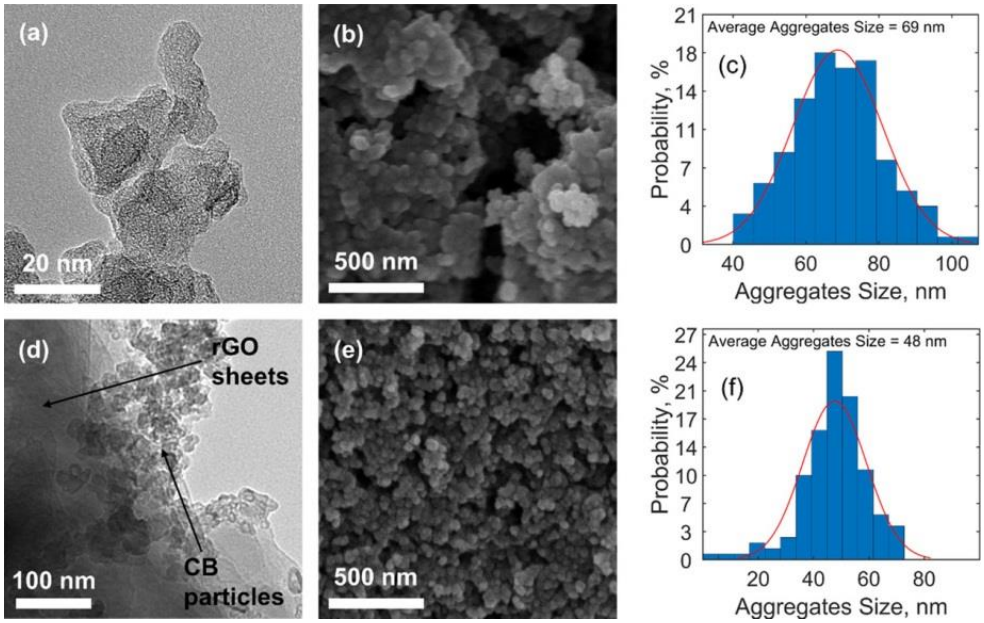


**Figure 57**: (a, d) TEM and (b, e) FE-SEM images of (a, b) CB_TT and (d, e) CB/GO_TT with the relative histograms of aggregate size distribution (c, f), respectively (see Table 2 in "Materials and Methods" for the adopted nomenclature in this work). The term referred to the current collector has been omitted since it does not affect thermal treatment results.

CB is characterized by hierarchical morphology with particles and aggregates: particles are the fundamental building block, but they are very rarely found in isolation due to van der Waals interactions that exert a driving force for their aggregation [135]. While the initial size of pristine CB particles used for this research work ranges between 20 and 50 nm [136]. The TEM images (Figure 57) analyse the thermally treated carbonaceous coating obtained from the CB-only suspension in the H2O/TX100 solution (CB_TT). They show that CB particles are disrupted and reduced in size, with values ranging from 10 to 20 nm (Figure 57a). Moreover, an average agglomerate size of 69 nm was estimated from the FE-SEM image in Figure 57b, and it is also depicted from the histogram with the size distribution in Figure 57c. Such a value is slightly smaller

than in usual CB aggregates (which ranges between 85 and 500 nm) [135]. Both phenomena suggest that the use of TX100 effectively aids the dispersion of the carbonaceous particles in water. However, signs of inhomogeneity and defects in the structure of the material are still clearly visible (Figure 57b).

When GO is added into the slurry, the resulting thermally treated nanocomposite (CB/GO_TT) is homogeneous and less defective (as pictured from SEM in Figure 57e). The role of TX100 is to predisperse CB in water and then to subsequently allow an intimate intercalation of GO sheets between CB particles. TX100 is a surfactant characterized by amphiphilic molecules with a hydrophilic region, consisting of polyethylene oxide chains, and a hydrophobic region, consisting of aromatic hydrocarbon chains. These are partially adsorbed by carbon, with the noncovalent π–π interaction between the aromatic rings and external graphene layers on the surface of CB particles having an important function. Meanwhile, the hanging polyethylene oxide hydrophilic tails determine steric stabilization of CB particles against the van der Waals forces that tend instead to aggregate them [137].

In GO, thanks to the hydrophilic behaviour of oxygen functional groups, water molecules can intercalate between graphene interlayer spacings, leading to stable suspensions in water [138]. When the latter is added to the predispersed CB mixture in water, the GO sheets could wrap CB particles and thus generate an interconnected 3D network (as imaged from TEM in Figure 57d and illustrated in Figure 58a). The network prevents CB to flocculate into bigger clusters and thus leading to smaller agglomerates, as confirmed by an estimated average size of 48 nm depicted in Figure 57f.

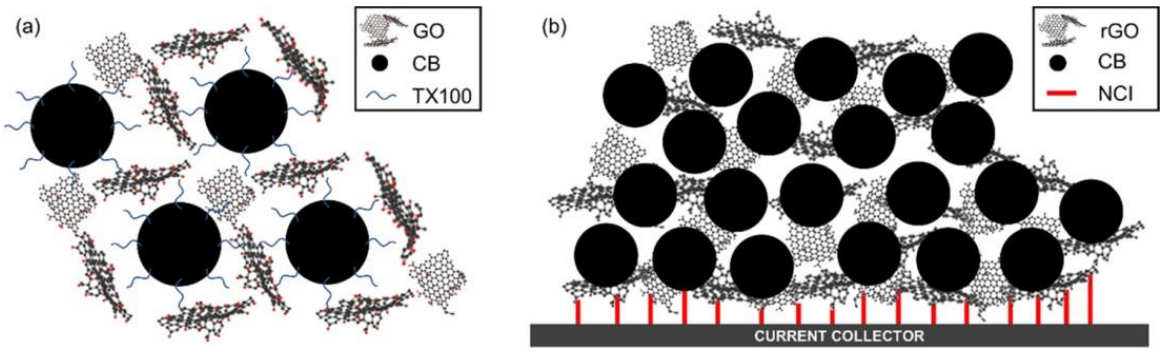


**Figure 58**: Proposed schemes for (a) the 3D interconnected network consisting of CB and GO with TX100 molecules as dispersers and (b) the electrically conductive carbon nanocomposite consisting of CB and rGO with noncovalent interactions (NCI) enhancing the adhesion with the current collector.

As water evaporates in ambient conditions, the 3D structure is maintained, but it is very likely that some of its molecules would be trapped due to the strong noncovalent interactions with the CB/GO/TX100 complex. Moreover, the electrically insulating GO sheets lead to poor electrical conductivity in the electrodes, while the adsorbed TX100 molecules affect electrolyte ion diffusion. Thus, poor electrochemical performances are expected from the ambient dried samples.

On the other side, when high temperatures are applied, there is the formation of a highly electrically conductive carbon nanocomposite with free access to pores for electrolyte ion diffusion. Moreover, there is an enhanced adhesion thanks to noncovalent interactions with the current collector, as schematized in Figure 58b. Therefore, remarkable electrochemical performances are likely to be developed. Conductive nanocomposite and its adhesion derive from two simultaneous phenomena. The first phenomenon is the thermal reduction of non-electrically conductive GO to form conductive rGO, discussed in the following paragraphs with the supporting Raman spectroscopy

and X-ray diffractometry (XRD) results. The second phenomenon is the complete evaporation of TX100. Such evaporation takes place when a critical temperature of 310 °C is reached under an inert atmosphere, as demonstrated by Mitsuda et al., [139].
The Raman spectra of all the carbonaceous coatings (Figure 59a) show the existence of the so-called "G band" and "D band". G band arises from the primary vibration mode of $sp^2$ atoms in rings and chains, which is a characteristic of all graphitic materials, at ~1600 $cm^{-1}$. The D band arises at ~1345 $cm^{-1}$ from the breathing modes of $sp^2$ atoms, when defects and disorder in the crystalline structure activates such scattering.

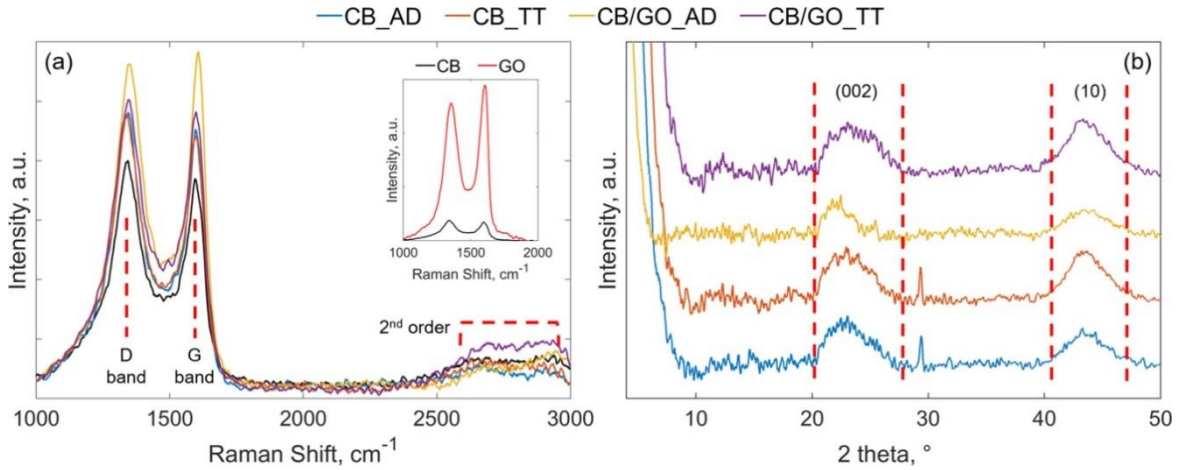


**Figure 59**: (a) Raman spectra of the carbonaceous coatings with untreated CB included as reference; the inset shows the comparison between CB and GO. (b) XRD patterns of the same coatings. The term referred to the current collector has been omitted since it does not affect thermal treatment results.

These two features can be merged in their peak intensity ratio ($I_D/I_G$) to analyse the structure quality, where higher values of the ratio correspond to an increased disorder [140, 141]. The as-calculated values for the materials under examination are reported in Table 5. Pristine CB and GO were included for reference purposes, with the higher intensity of GO peaks, explainable with a smaller crystallite size.

| sample | $I_D/I_G$ ratio | (002) [°] | (10) [°] | $d_{002}$ [Å] | $L_C$ [Å] | $L_A$ [Å] |
|---|---|---|---|---|---|---|
| CB_AD | 1.06 | 23.01 | 43.63 | 3.86 | 18.6 | 40.4 |
| CB_TT | 1.08 | 23.09 | 43.63 | 3.85 | 18.1 | 42.1 |
| CB/GO_AD | 0.96 | 22.23 | 43.70 | 4.00 | 27.3 | 36.3 |
| CB/GO_TT | 1.04 | 23.55 | 43.60 | 3.77 | 17.8 | 41.0 |

**Table 5**: Raman D-to-G Band Ratios, XRD Peak Positions, Lattice Spacing, and Crystallite Sizes.

Their $I_D/I_G$ ratios of, respectively, 1.08 and 0.96 reveal instead their expected disordered structures. The material resulting from the ambient dried CB-only suspension in the TX100/$H_2O$ solution shows a marginal increase in intensity of the peaks. We can explain this intensity with the reduction in size of CB agglomerates during the processing in the presence of TX100. Moreover, as the $I_D/I_G$ ratio is only slightly reduced to 1.06, the overall disorder of the crystallite structure can be assumed as unaffected. The thermally treated suspension CB_TT is almost unvaried in both peak intensity and $I_D/I_G$ ratio (equal to 1.08), confirming that CB is inert at 550 °C under an Ar atmosphere.
On the other hand, the nanocomposite obtained from the ambient dried CB/GO slurry is characterized by higher peak intensity and an $I_D/I_G$ ratio of 0.96. So, in this case GO sheets in

solution successfully help the disaggregation and stabilization of CB agglomerates in smaller particles. This process leads to a homogeneous mixture and thus confirming our previous assumption and TEM and FE-SEM results. When the thermal treatment is applied, oxygen functional groups and intercalated water are eliminated, releasing carbon dioxide ($CO_2$), carbon monoxide (CO), and water vapor. After that, the conjugated network of the hexagonal lattice of carbon atoms is restored [108].

The last is the mechanism governing the electrical conductivity of graphene [15]. The transition from the electrical insulating behaviour of GO toward the conductive one of rGO is confirmed by electrochemical tests that will be described later. The generated rGO sheets show a higher degree of disorder as depicted by an $I_D/I_G$ ratio of 1.04, a value in between those of the CB/GO nanocomposite after ambient drying (CB/GO_AD) and CB_TT. The higher ratio is due to vacancies and topological defects on graphene layers after the release of $CO_2$ and CO [108].

The successful reduction of GO to rGO is furthermore proven by the increased intensity of second-order scatterings, around the graphene-associated 2D band at ~2700 $cm^{-1}$ [142]. 2D band also shows turbostratic arrangements of graphene layers [140].

The XRD patterns of the CB/GO nanocomposite and of the processed CB-only carbonaceous material used as reference, before and after thermal treatment, are presented in Figure 59b. They all show a broad peak at around 22.97°, attributable to the (002) carbon lattice. (002) peak is downshifted with respect to the ordered structure of graphite, where the same peak is sharp and shown at 26.38° [143]. According to Bragg's law [116], reported in Equation 32, the interplanar spacing $d_{002}$ in CB_GO_AD has a measured value of 4 Å. Such spacing is higher than the counterpart without the addition of GO (CB_AD), as observable from the values summarized in Table 5. This difference suggests a more expanded and amorphous 3D structure of the nanocomposite, as compared to the 3.38 Å of crystalline graphite.

When the thermal treatment is applied, $d_{002}$ is almost unvaried for the CB-only carbonaceous material, while it is contracted to a value of 3.77 Å for CB_GO_TT. This is a result of the reduction of GO to rGO, which leads to the reorganization of the structure toward a more ordered fashion. Other important carbon features are the (100) and (101) lattice peaks, usually shown in graphite at $2\theta$ values of, respectively, 42.22 and 44.39° [143]. However, for all the tested carbonaceous coatings, these peaks are merged into the broad (10) peak at around 43.64°. The latter is a consequence of turbostratic arrangements of graphene layers [143].

According to the Scherrer equation (Equation 33) [117], we can know the two main crystallite dimensions, which are the stacking height $L_C$ and the crystallite lateral size $L_A$. $L_C$ can be estimated from the (002) peak, using a shape factor of 0.89. $L_A$ derives from the (10) peak, with a shape factor of 1.84 [144]. From their values, reported in Table 5, it is possible to notice the difference in both sizes between the two ambient dried samples, with and without the addition of GO. $L_C$ and $L_A$ are instead comparable after the thermal treatment. The bigger stacking height in CB/GO_AD than in CB_AD can be explained, in accordance with the interplanar spacing behaviour, with an expanding effect of intercalated GO layers. In the CB-only material, almost no difference is measured in both $L_C$ and $L_A$ passing from the ambient dried to the thermally treated sample. In the CB/GO nanocomposite, however, a sharp decrease of $L_C$ and a simultaneous increase of $L_A$ are registered after the thermal treatment.

These results are evidence of a hybrid structure for the carbonaceous nanocomposite under investigation, composed by an ordered graphitic state and an amorphous state. This structure is typical in amorphous carbon as CB but influenced by GO intercalation. The amorphous subphase is promoted over the crystalline one in the ambient dried sample, due to a higher interplanar spacing

and to a bigger crystallite size. After the application of the thermal treatment, the reduction of GO to rGO causes an opposite effect favouring the crystalline subphase, due to the reduced spacing and the smaller crystallite size.

**Electrochemical Characterization**

Figures 60a-b show the cyclic voltammetries (CVs) and galvanostatic cycles (GCs) of SCs made with the CB/GO slurry before and after thermal treatment. In addition, the CVs and GCs of SCs made with the CB-only slurry before and after thermal treatment are reported for comparison.

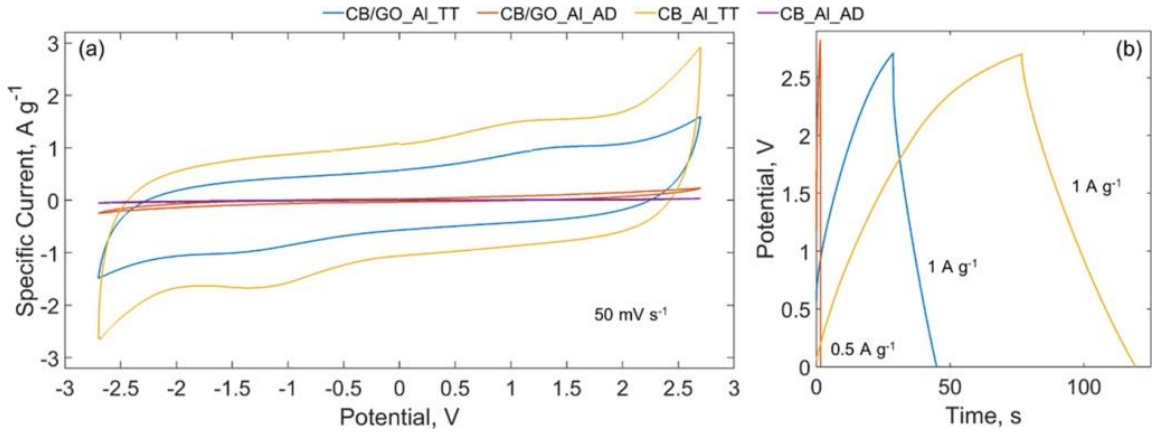


**Figure 60**: (a) CVs at 50 mV/s between −2.7 and +2.7 V and (b) GCs at 0.5 and 1 A/g in a 1.5 M solution of TEMA-TFB in ACN of SCs made with CB/GO_Al_TT, CB/GO_Al_AD, CB_Al_TT, and CB_Al_AD (the GC profile of the latter is omitted as the internal resistance was too high to perform measurements with comparable specific currents with respect to the other samples).

In Figure 60a, CVs are recorded using a scan rate of 50 mV/s in a potential range of −2.70 to +2.70 V; in Figure 60b, GC curves were obtained with specific currents of 0.5 A/g for CB/GO_Al_AD and of 1 A/g for CB/GO_Al_TT and CB_Al_TT. In the latter case, the different specific currents are justified by practical reasons. Using the same specific current (0.5 or 1 A/g) for all the samples, the CB/GO_Al_TT and CB_Al_TT curves would be much longer than that of CB/GO_Al_AD, leading to the impossibility of observing the trend of the latter. In Figures 60a-b, the differences between CB/GO_Al_AD and CB/GO_Al_TT prove that only with thermal treatment of GO an active material suitable for SCs can be achieved. The area under the CV curve of the thermally treated sample, CB/GO_Al_TT, is 18 times wider than that of the untreated one, CB/GO_Al_AD. In fact, the values of $C_S$ calculated using Equations 40 and 12 are, respectively, 47.7 and 2.7 F/g for a scan rate of 100 mV/s.

Observing Figures 60a-b, at first glance the sample without GO in the starting slurry, CB_Al_TT, shows even better electrochemical performances. Actually, it lacks other crucial properties, such as adhesion on the current collector and mechanical stability, as shown in Figure 61. This behaviour arises from the absence of any binder, and therefore, such an active material can hardly be considered for the manufacture of SCs. For GCs of non-thermally treated sample, the nonlinearity of the curve was too high to conduct any measurements. Instead, GC is almost linear in the discharge curve of the sample annealed at 550 °C. In this case, $C_S$ was of 27.4 F/g for a specific current of 1 A/g, calculated using Equations 42 and 12.

These results are a consequence of the thermal GO reduction. Since GO is an insulating material, it hinders charge transfer inside the pores. In fact, a voltage drop in the discharge curve is dominant in the CB/GO_Al_AD sample. Without reduction, the oxygen-containing groups of GO can lead to

Faradaic reactions during the charge/discharge process, deviating from EDLC behaviour. Such reactions also explain the nonlinearities in the curve and the leakage.

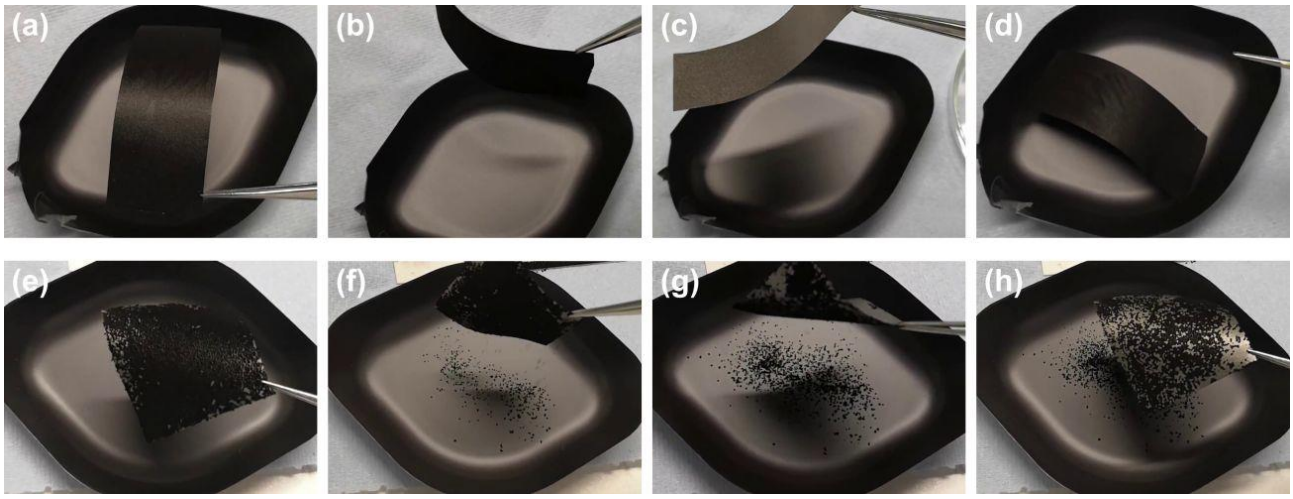


**Figure 61**: Qualitative comparison of the adhesion of the active material on the current collector and of its mechanical integrity between (a-d) CB/GO_Gr_TT and (e-h) CB_Gr_TT as samples were: (a) and (e), as taken out from the furnace; (b) and (f), tilted on a side; (c) and (g) tilted upside-down; (d) and (h), returned to horizontal position. A considerable amount of active material falling from the current collector is noticeable for the sample CB_Gr_TT, while no material is detached from the sample CB/GO_Gr_TT.

The tests shown in Figures 60a-b highlight mainly the effectiveness of the GO reduction procedure (1 h at 550 °C under Ar flow). However, the sample of main interest for the current work, CB/GO_Gr_TT, deserved more tests to carry out on, as pictured in Figures 62a-b. The active mass loading, necessary to extrapolate the specific capacitance from the cell capacitance, is also reported in Table 6. Table 6 shows also the absolute and specific capacitance range, calculated from direct measurements performed with the electrochemical workstation according to Equations 40, 12, and 42.

| Sample | Active mass [mg] | Capacitance range [mF] | Specific Capacitance range [F/g] |
|---|---|---|---|
| CB_Al_TT | 3.68 | 31.6-51.6 | 34.3-56.1 |
| CB_Gr_TT | 3.33 | 42.2-47.3 | 50.6-56.7 |
| CB/GO_Al_TT | 3.16 | 13.1-25.6 | 16.6-32.4 |
| CB/GO_Gr_TT | 2.33 | 13.1-21.7 | 22.5-37.2 |

**Table 6**: Comparison of the four devices of Figure 6 in terms of active mass loading, capacitance, and specific capacitance, with the values measured through GCs at specific currents ranging from 0.5 to 4 A/g.

Figure 62a shows CVs between −2.70 and +2.70 V at 50, 100, 300, and 500 mV/s. The rectangular shape of these graphs proves reversibility of charge/discharge after GO reduction (i.e., electrostatic behaviour only). To study the effect on specific power and adhesion in an almost "all-graphene-based SC", the trend in GCs was also analysed. In Figure 62b, charge/discharge curves at 0.5, 1, 2, and 4 A/g are shown. Their analysis gives a specific capacitance range of 22.5−37.2 F/g and a specific energy range of 6.3−10.5 Wh/kg. The resulting specific power range is 28.8−32.9 kW/kg (ESR is between 30.2−26.5 Ω), calculated using, respectively, Equations 41 and 44.

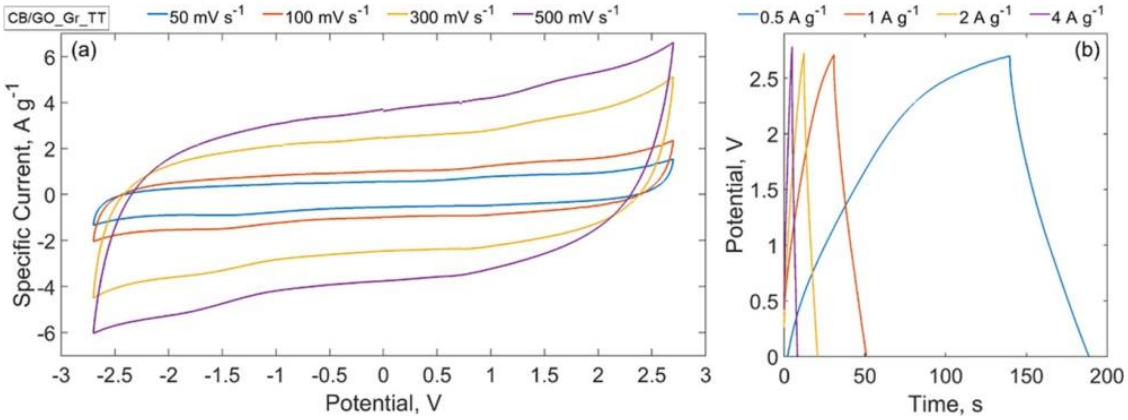


**Figure 62**: (a) CVs and (b) GCs of SCs made with CB/GO_Gr_TT at different scan rates, from 50 to 500 mV/s, between −2.7 and +2.7 V and different specific currents, from 0.5 to 4 A/g, in a 1.5 M solution of TEMA-TFB in ACN.

The specific capacitance values are lower than those in other available works in the literature because of the CB nature [39]. Even though the used CB powder (BP 2000®) is characterized by a high specific surface area (SSA) of 1216 $m^2/g$, its micropore volume is only 0.21 $cm^3/g$ [145]. For the more commonly used AC, in which the SSA ranges from 1000 to 2000 $m^2/g$, the micropore volume can reach 0.78 $cm^3/g$ [146]. We remind that a micropore is a pore that has a less than 20 Å diameter. So, there can be more electric charges in a micropore than in a larger pore with the same area because of the ions losing the solvation sphere of the solvent. In other words, CB's SSA is less efficiently exploited than that of AC. However, it should be noted that the coupling of rGO and CB allows the optimization of other aspects of an EDLC, as shown in this research work.

The linearity of the curve from 1 A/g and above is another sign of an almost purely electrostatic behaviour of this SC configuration. The only case in which there is a difference between the time of charge and discharge is at 0.5 A/g, due to leakage effects at low currents. In particular, at 1 A/g, a specific power of 32.1 kW/kg was obtained. Since this result is correlated with a specific energy of 8.8 Wh/kg, the SC under analysis is hence above the common limits of a commercial SC. In last case, a SC has a maximum of 10 kW/kg of power and less than 10 Wh/kg of energy [1]. The energy value derives from a combination of a specific capacitance of 31.1 F/g with a highly optimized electrolyte such as TEMA-TFB in ACN. This electrolyte uses an organic solvent with high working voltage and good conductivity in addition to TEMA-TFB ions that entail cycle stability. Unfortunately, this electrolyte is toxic and flammable [147].

Figure 63 shows a comparison of SCs in the Ragone plot, a plot of the specific power versus the specific energy. It shows that, while the specific energy ranges are superimposable, when the current collector is made with rGO, there is an improvement in specific power with the same electrode. A possible explanation of this improvement could be in a different interaction of rGO in the active material when coated on a current collector consisting of the same material, such as rGO paper. In the other cases, current collector is a metal sheet, such as Al foil. In the studied electrodes, the adhesion derives from interactions of the non-removed oxygen-containing groups of rGO with the substrate surface [27].

However, Al is a metal with an easy tendency to oxidize that often requires chemical etching to allow carbon coating. In contrast, rGO paper does not need etching to form this bonding since, chemically, it is almost pure carbon. This is particularly true for the used rGO paper collector, because it is characterized by a high degree of reduction of GO. A check of this degree is available in the XRD analysis on this material showed in Rapisarda and Meo's previous work [134].

Moreover, the rGO paper does not involve a discontinuity between two different materials (as for the Al-carbon interface) for the current flow during the charge/discharge process.

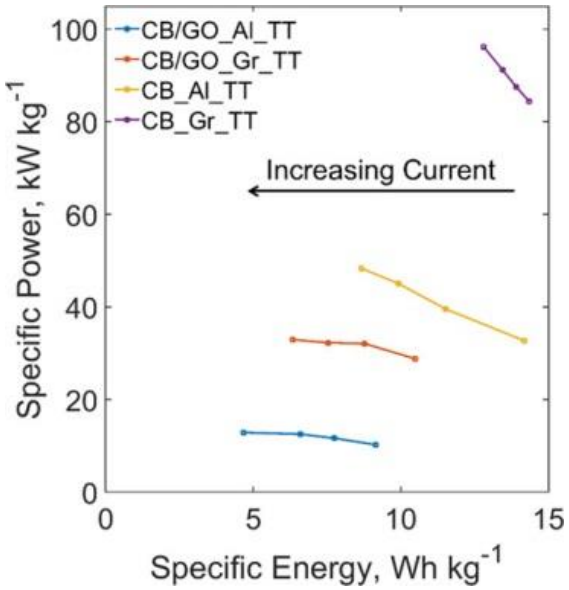


**Figure 63**: Ragone plot of specific power versus specific energy for SCs made with CB/GO_AL_TT, CB/GO_Gr_TT, CB_Al_TT, and CB_Gr_TT.

Surprisingly, Figure 63 shows also that the two analogous samples fabricated from the active material slurry prepared without the addition of GO perform better in both specific energy and power. These results are in ostensible contradiction with Galhena et al. [27]. It is however crucial to point out that this kind of active material has a very weak adhesion on both Al and rGO paper current collectors. CB-only electrodes had an extreme fragility and thus they tended to the ease of breaking when assembling SC samples (see Figure 61). Consequently, if anything, these electrodes could be adopted for the manufacture of very small devices with a delicate assembling process. In any case, they would unquestionably be not scalable.

Nevertheless, the CB_Al_TT and CB_Gr_TT samples show in a clearer way that the specific power of a SC with an rGO-based current collector surpasses that of an Al-based one by a factor of almost 2. More precisely, for the maximum recorded values, the specific powers are, respectively, 98.9 and 49.4 kW/kg, due to ESRs of 2.8 and 10.0 Ω. In addition, rGO paper mass density is less than 1/2 of Al mass density (1.2 against 2.7 g/cm$^3$). A device such as the sample CB/GO_Gr_TT could reach a 4-fold increase of the specific power when compared to a common SC, with a doubled specific energy. For the sake of clearness, this estimate omits the weight of the separator, the electrolyte, and of all the connectors of which a complete device is made.

# 3.4 Deepening about temperature

Thanks to a conference paper that I co-authored, the reasons behind the use of a temperature of 550 °C for GO reduction can be deepened. In fact, this other work deepens the effects of thermal treatments on our samples, regardless the performance of their SCs.

A further thermal treatment temperature was chosen, specifically of 200 °C, as intermediate value to compare with 550 °C. Thermal treatments at 200 and 550 °C were performed in a tubular furnace for 1 h under Argon atmosphere (respectively TT_200 and TT_550). Powdered samples of the

coatings were finally collected scratching the substrate and stored in a dry atmosphere before subsequent analysis, namely TEM imaging, RS, and XRD.
CB and GO were studied both separately and as the nanocomposite electrode (CB/GO), together with the adopted surfactant, TX100. Besides the analysis conducted at three different temperatures, this study also focused on the GO reduction process thanks to a Zeta Potential (ZP) test.

**TEM imaging**

The behaviour of CB particles subjected to different temperatures conditions, and the effects of their mixing with GO was initially studied with TEM imaging. According to ASTM definition [148], CB particles show a peculiar hierarchical morphology with spherical nodules, which are the fundamental building block. The nodules have sizes ranging from 10 to 300 nm. These form at first aggregates of 85-500 nm, held together by covalent bonds, and secondarily agglomerate of 1-100 µm thanks to van der Waals interactions. Figure 64a shows a TEM image of a large agglomerate from the CB_AD sample with a higher magnification in the onset. The size-scales of nodules, aggregates, and agglomerates are in good agreement with the previous definition. This structure is well maintained also for both the thermally treated samples, CB_TT_200 and CB_TT_550 (with the latter being pictured in Figure 64b). This analysis proves CB inertness at the tested conditions and thus simplifying the thermal treatment optimization.
When introduced into the slurry, GO interacts with CB leading to a 3D carbonaceous network aided by the TX100 presence. Particularly, it allows an initial dispersion of CB particles in water that are subsequently surrounded by GO sheets, as observable in TEM images in Figures 64c-e from,

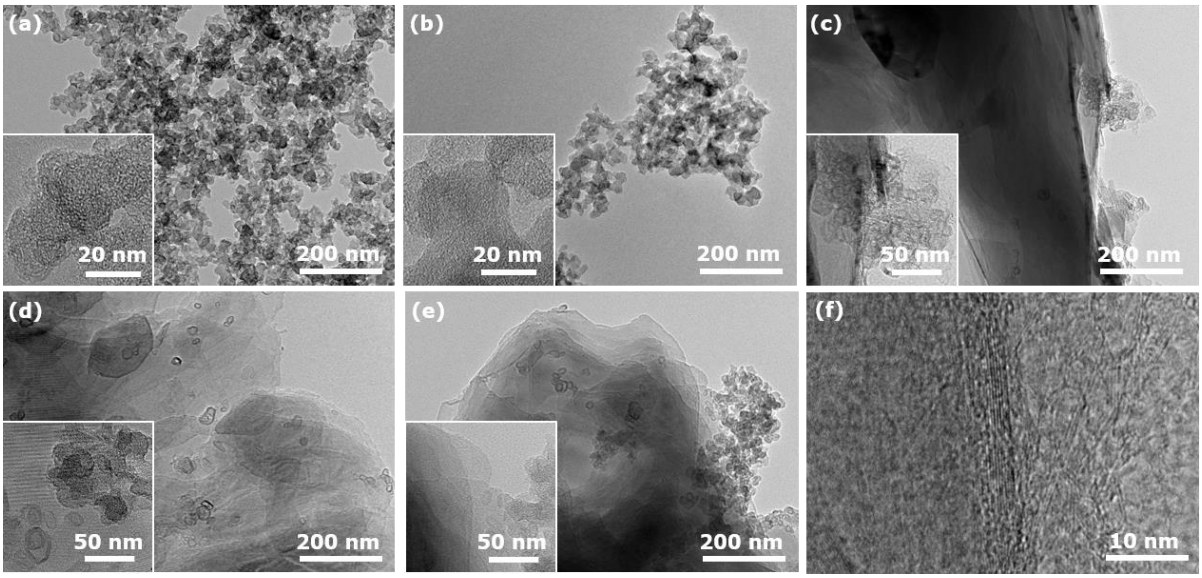


**Figure 64**: TEM images of (a) CB_AD, (b) CB_TT_550, (c) CB/GO_AD, (d) CB/GO_TT_200, and (e) CB/GO_TT_550 with higher magnification in the onset and (f) high magnification image of rGO sheets.

respectively, CB/GO_AD, CB/GO_TT_200 and CB/GO_TT_550 samples. Additionally, the reduction of GO to rGO is proved by the interference lines in the large sheets, as highlighted from the high magnification image of the CB/GO_TT_550 sample in Figure 64f.

**RS and XRD characterizations**

The resulting spectra from Raman characterization of CB and CB/GO samples are shown in Figure 65a. As evidenced from the values summarized in Table 7, the introduction of GO in the slurry leads to a reduction of $I_D/I_G$ from 1.07 of CB only to 0.96 for CB/GO, with both subjected to

ambient drying. This confirms the interaction of GO sheets with CB particles, which was previously observed with TEM imaging, and thus GO role as dispersing agent leading to a homogeneous carbonaceous nanocomposite.

Furthermore, also the effects of the thermal treatments on $I_D/I_G$ can be observed. For CB-only samples, no differences are shown, and it is explainable with CB inertness at the tested treatment conditions. In CB/GO samples, the $I_D/I_G$ value increases from 0.96 of the ambient dried sample to 1.05 and 1.04 of, respectively, the 200 and 550 °C treated samples. Such increase of disorder is a consequence of topological defects induced on graphene lattices after the release of $CO_2$, CO, and water vapor. Such release is driven by heat provision, which is the mechanism governing the reduction of GO [108].

The slightly lower value shown in CB/GO_TT_550 could be explained with a tendency of the structure to rearrange thanks to the higher amount of provided energy. Such behaviour has, however, an asymptotical trend, as it only manifested after an increment in temperature of 350 °C.

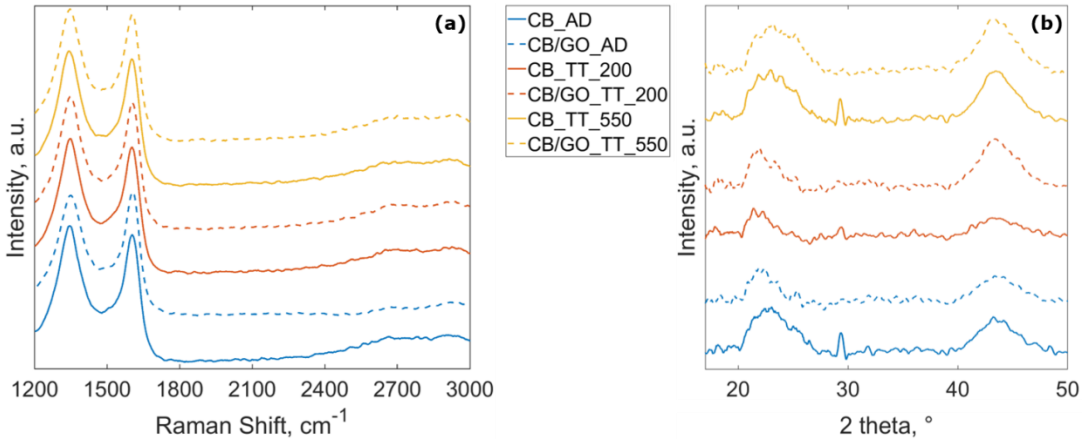


**Figure 65**: (a) Raman spectra and (b) XRD patterns.

| Sample | $I_D/I_G$ ratio | (002) $2\theta$ [°] | (10) $2\theta$ [°] | $d_{002}$ [Å] | $L_C$ [Å] | $L_A$ [Å] |
|---|---|---|---|---|---|---|
| CB_AD | 1.07 | 23.01 | 43.63 | 3.86 | 18.6 | 40.4 |
| CB/GO_AD | 0.97 | 22.23 | 43.70 | 4.00 | 27.3 | 36.3 |
| CB_TT_200 | 1.07 | 21.92 | 43.74 | 4.05 | 30.4 | 36.0 |
| CB/GO_TT_200 | 1.05 | 22.00 | 43.65 | 4.04 | 28.1 | 41.6 |
| CB_TT_550 | 1.07 | 23.09 | 43.63 | 3.85 | 18.1 | 42.1 |
| CB/GO_TT_550 | 1.04 | 23.55 | 43.60 | 3.77 | 17.8 | 41.0 |

**Table 7**: Raman D to G band ratios, XRD Peak Positions, Lattice Spacing, and Crystallite Sizes.

The XRD patterns of both the CB and CB/GO samples in all the examined temperature conditions are depicted in Figure 65b. The results from these further calculations of $d_{002}$, $L_C$ and $L_A$ are summarized in Table 7. From the latter it is possible to observe how $d_{002}$ in CB samples is similar when subjected to ambient drying and thermally treatment at 550 °C, while it is larger when thermally treated at 200 °C.

When GO is introduced, $d_{002}$ is larger for the AD sample, larger also when compared to CB only, comparable in size in CB/GO_TT_200 and highly contracted in CB/GO_TT_550, with a value that is even smaller than CB_TT_550. Accordingly, $L_C$ shows a similar trend. Regarding $L_A$, in CB samples it decreases from AD to the treatment at 200 °C and then it increases again in CB_TT_550. When GO is introduced, $L_A$ instead increases from CB/GO_AD to CB/GO_TT_200 and then

slightly decreases after the treatment at 550 °C. Such behaviour is explainable with the intercalation of GO sheets that initially leads to more expanded and disordered stacking. In contrast, when the complete reduction to rGO thanks to the treatment at 550 °C occurs, they promote instead higher compaction and order.
Summarizing, XRD shows a U-trend of the structure optimization for rising temperatures. In accordance with Mitsuda et al., a critical temperature of 310 °C for a minimum of 30 min under inert atmosphere is required for the complete evaporation of TX100. A non-complete evaporation and partial degradation of the latter could thus explain the results after the treatment at 200 °C and the trend previously described.

**Zeta Potential**

Analysing GO in water, ZP is -48.3 mV, meaning that GO flakes are rich of negative charges due to oxygen-containing groups, as predictable by its hydrophilicity and stability in water. After the thermal treatment at 550°C, ZP becomes -7.51 mV. This value indicates a strong reduction of the negative surface charge, accordingly with GO reduction.
Figure 66 shows the ZP Distributions (ZPD) of GO and of GO_TT_550. In particular, the GO ZPD has a wide feature formed by a main peak at -44.8 mV and by a second peak at -60.3 mV, with standard deviations of 6.42 and 4.45, respectively. GO_TT_550 ZPD has instead only one sharp peak with standard deviation of 3.68 mV. A comparison between the ZPDs remarks the GO reduction efficacy due to the thermal treatment considering its uniformity over the GO particles, regardless their initial level of oxidation.

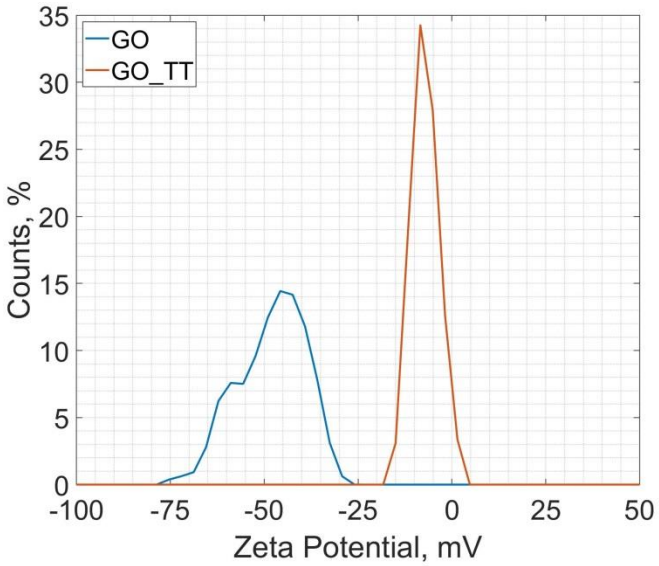


**Figure 66**: Zeta Potential Distribution (in terms of percentage of counts) of GO and GO_TT.

**Chemical kinetics hypothesis**

As previously shown in this work, the GO reduction reaction can be observed with different characterization techniques. However, in order to quantitatively evaluate it, additional hypotheses are required. The final purpose is an estimation of the reduction degree, i.e. the mole ratio of oxygen presence in the molecules before and after the thermal treatment. Particularly, the results from the ZP analysis can be used under the hypothesis of validity of the following formula, conceived by Ge and Wang for a similar purpose [149]:

$$\sigma_{eff} = \sqrt{8cN\varepsilon_r\varepsilon_0 k_B T}\sinh\left(\frac{e\zeta}{2k_B T}\right) \qquad (45)$$

In Equation 45, $\sigma_{eff}$ is the effective surface charge density, which is the sum of charge density on a flat surface and its surrounding ions enclosed by the slipping plane. $T$ is the absolute temperature (298.15 K, i.e., the 25 °C of the ζ-analysis), while all the other parameters refer to the slurry features. In our case, these parameters are constant, since both GO and GO_TT were dispersed in the same solvent at the same condition, so they disappear in the ratio in Equation 46. The following equation represents in fact the ratio of $\sigma_{eff}$ before and after the reaction. Indirectly, it gives an estimate of the remaining charges on GO after reduction, since ZP changed after the thermal treatment.

$$\frac{\sigma_{eff}^{GO\_TT}}{\sigma_{eff}^{GO}} = \frac{\sinh\left(\frac{e\zeta^{GO\_TT}}{2k_B T}\right)}{\sinh\left(\frac{e\zeta^{GO}}{2k_B T}\right)} \qquad (46)$$

Using data from the as performed ZP analysis, the resulting ratio is 0.135, meaning that GO_TT lost the 86.5 % of the initial oxygen-containing groups.
At this stage, it is then possible to proceed with a chemical kinetics evaluation. We assume that the GO reduction evolution can be described with the following law shown by Equation 47:

$$n_O(t) = n_O(0)e^{-\frac{t}{\tau}} \qquad (46)$$

$n_O(t)$ is the oxygen mole number at the time $t$, $n_O(0)$ is the initial mole number and $\tau$ is the time constant at fixed temperature. In fact, we can use the estimated ratio from the previous calculation and the inverse formula of Equation 47 to estimate $\tau$.

$$\tau = -\frac{t}{\ln\left(\frac{n_O(0)}{n_O(t)}\right)} \qquad (47)$$

At $t$ of 1,800 s, the value of 900 s can be derived for $\tau$. This means that the adopted 30 min treatment corresponds to a GO reduction after 2τ, while the 60 min one would correspond to a 4τ reduction. The latter is beyond 3.5τ, which is the time used as a practice for the phenomena governed by a negative exponential trend. Thermal treatments duration between 30 and 60 min are hence recommended for an efficient GO reduction during SCs electrode fabrication. In fact, higher temperatures (i.e. minor time) are too close to the melting point of aluminium, that is the most commonly used current collector. In contrast, at lower temperatures the required reaction time for an effective reduction grows exponentially due to the inherent dependence of τ from temperature (see Equation 30, copied from Chapter 2).

$$k = Ae^{-\frac{E_a}{RT}} \qquad (30)$$

In other word, the kinetic analysis evidenced a time optimization congruent with the temperature optimization.

# 3.5 Conclusion

In this study [4], a binder-free electrode was successfully manufactured using:

- water as the only cheap and ecological solvent
- GO as an alternative active binder that led to the formation of a homogeneous CB/GO nanocomposite.

The material was subjected to a high-temperature (550 °C) thermal treatment to reduce GO to rGO and thus unlock its ability to actively contribute to electrical energy storage performances. The reduction effectiveness was confirmed by the increase of the $I_D/I_G$ ratio from 0.96 to 1.04 before and after, respectively, the thermal treatment, as depicted by Raman studies. Reduction was also confirmed by the XRD analysis, with the reduction of the interlayer spacing $d_{002}$ from 4.00 to 3.77 Å.

Supplementary work performed during 2021 showed how the temperature can be a crucial parameter for a multifactorial optimization problem [5]. One factor is the aim of drying the described water-based slurry CB/GO for a direct electrode fabrication. In this case, the minimum temperature is the highest between the boiling points of the solvent (i.e., 100 °C for water) and the used non-conductive surfactant additives (i.e., 270 °C for TX100). A second factor is the GO reduction. However, at 550 °C, which is close to the maximum temperature that the electrode could withstand, the GO reduction takes place at its chemical-kinetic limits. With such temperature treatment, an improvement of the nanocomposite structure was evidenced by the chemical-physical analysis. Considering also process duration as a factor for an industrial scale-up, the analysis reaffirms to perform the thermal treatment at the limit temperature of 550 °C. Even though this value implies higher energy costs, it allows a better optimization of the manufacturing process.

The electrochemical characterization showed interesting results with a high specific power of 32.1 kW/kg and a corresponding specific energy of 8.8 Wh/kg at a specific current of 1 A/g. The latter demonstrates that the development of a cheap, environmental-friendly, and scalable manufacturing process represents a valuable path for future improvements of the SC industry. In fact, this process is unlocked by the complete removal of polymeric binders and organic solvents in the slurry preparation process. Moreover, it uses also an innovative lightweight and high-quality current collector based on rGO. In other words, it allows the fabrication of an “all-graphene based” device.

# Conclusions

In the first Chapter, we showed that there is an exponentially growing interest in scientific research on SCs. This interest is due to their technological usefulness in green energy, automotive, heavy machine, and improvement of battery-based systems. A consequence of the current researches is the wide range of possibilities about SCs improvement, beyond the main aims of higher specific capacity and specific energy. Even in this last case, also a "research about the use of graphene" is nowadays a generic statement for many kinds of specific applications.

Nonetheless, from the industrial point of view, nowadays there are rare alternatives to electrodes made with Activated Carbon (AC) and to organic electrolytes (acetonitrile and Propylene Carbonate). Even if many researches obtained experimental SCs that overcome commercial performances, to actually realize a new device, every step of the manufacturing process (from raw materials to final product) needs optimization in terms of scalability and environmental impact, regardless the electrochemical performance.

In the light of these considerations, we preferred to focus not on graphene, but on Graphene Oxide (GO). In fact, even if GO is an electric insulator, it is easily to disperse in water, easily to exfoliate from Graphite Oxide, and easily to transform in a graphene-like material. In the case of our experimental works, after a thermal reduction, GO assumes the triple function of electrode, coupled with a Carbon Black (CB), of conductive binder and current collector. Our SCs reaches almost the same energy density of a commercial SC with a huge improvement in power density. Moreover, its manufacturing process uses water in the slurry preparation and a purely physical GO reduction (without toxic reactants). Deepening the temperature role in the process, we discussed also its optimization, always in the viewpoint of a global improvement.

Of course, there is a wide space of improvement for our work. For example, instead of using a CB, we could repeat all the steps with an AC. Moreover, this AC could derive from waste material, as scraps of orange juice [58].

Even Ar, an expensive gas, could be replaced by under vacuum treatment, eventually using also a "thermal shock reduction", as described in the previous chapter [107]. This method makes shorter cooling time, too. This simpler chemical-physical mechanism would need "only" a suited industrial line, but it is not an impossible task.

Besides used materials, another optimization can involve exfoliation and mixing. Thanks to wide scientific literature about graphene production, we know that a mixing tool can be also an exfoliation tool [98]. Through this expertise, we can unify exfoliation and mixing in a single step, simplifying slurry preparation.

After slurry preparation, coating on a current collector has not to be necessary symmetric. On the contrary, the same procedure can be used to produce an AEDLC, in such a way to apply on a SC with the same electrolyte a higher working voltage.

Finally, the traditional electrolyte made with acetonitrile and TEMA-TFB should let greener electrolytes go ahead. Even though an alternative solvent with the same performance of sustainable voltage and conductivity is not yet industrially available, an ecological one is however strongly recommended. Such kind of electrolyte will make a SC produced by water-based techniques fully environmental-friendly, from its production till the end of its incredibly long life-cycle.

# Bibliography


[1] P. Simon and Y. Gogotsi, “Materials for electrochemical capacitors,” *Nat. Mater.,* vol. 7, p. 845–854, 2008.

[2] G. Abbate, E. Saraceno and A. Damasco, “Supercapacitor for Future Energy Storage,” in *Sustaining Resources for Tomorrow. Green Energy and Technology*, Springer, Cham, 2020, p. 205–243.

[3] M. Singh, C. Zannella, V. Folliero, R. Di Girolamo, F. Bajardi, A. Chianese, L. Altucci, A. Damasco, M. Del Sorbo, C. Imperatore, M. Rossi, M. Valadan, M. Varra, A. Vergara, G. Franci, M. Galdiero and C. Altucci, “Combating Actions of Green 2D-Materials on Gram Positive and Negative Bacteria and Enveloped Viruses,” *Front. Bioeng. Biotechnol.,* vol. 8, p. 569967, 2020.

[4] M. Rapisarda, A. Damasco, G. Abbate and M. Meo, “Carbon Black and Reduced Graphene Oxide Nanocomposite for Binder-Free Supercapacitors with Reduced Graphene Oxide Paper as Current Collector,” *ACS Omega,* vol. 5, p. 32426–32435, 2020.

[5] M. Rapisarda, A. Damasco, G. Abbate and M. Meo, “The temperature role in the manufacturing of an electrode for supercapacitors with Carbon Black and Graphene Oxide,” *Chem. Eng. Trans.,* vol. 84, p. 133–138, 2021.

[6] C. Abbey and G. Joos, “Supercapacitor Energy Storage for Wind Energy Applications,” *IEEE Trans. Ind. Appl.,* vol. 43, p. 769–776, 2007.

[7] M. Hassanalieragh, T. Soyata, A. Nadeau and G. Sharma, “UR-SolarCap: An Open Source Intelligent Auto-Wakeup Solar Energy Harvesting System for Supercapacitor-Based Energy Buffering,” *IEEE Access,* vol. 4, p. 542–557, 2016.

[8] N. Ghaviha, J. Campillo, M. Bohlin and E. Dahlquist, “Review of Application of Energy Storage Devices in Railway Transportation,” *Energy Procedia,* vol. 105, p. 4561–4568, 2017.

[9] Z. Song, J. Hou, H. Hofmann, J. Li and M. Ouyang, “Sliding-mode and Lyapunov function-based control for battery/supercapacitorhybrid energy storage system used in electric vehicles,” *Energy,* vol. 122, p. 601–612, 2017.

[10] M. G. Carignano, R. Costa-Castelló, V. Roda, N. M. Nigro, S. Junco and D. Feroldi, “Energy management strategy for fuel cell-supercapacitor hybrid vehicles based on prediction of energy demand,” *J. Power Sources,* vol. 360, p. 419–433, 2017.

[11] L. Stobinski, B. Lesiak, A. Malolepszy, M. Mazurkiewicz, B. Mierzwa, J. Zemek, P. Jiricek and I. Bieloshapka, “Graphene oxide and reduced graphene oxide studied by the XRD, TEM and electron

spectroscopy methods," *J. Electron Spectrosc. Relat. Phenom.,* vol. 195, p. 145–154, 2014.

[12] O. C. Compton and S. T. Nguyen, "Graphene oxide, highly reduced graphene oxide, and graphene: versatile building blocks for carbon-based materials," *Small,* vol. 6, p. 711–723, 2010.

[13] D. R. Dreyer, S. Park, C. W. Bielawski and R. S. Ruoff, "The chemistry of graphene oxide," *Chem. Soc. Rev.,* vol. 39, p. 228–240, 2010.

[14] A. A. Balandin, "Thermal properties of graphene and nanostructured carbon materials," *Nat. Mater.,* vol. 10, p. 569–581, 2011.

[15] S. Pei and H.-M. Cheng, "The reduction of graphene oxide," *Carbon,* vol. 50, p. 3210–3228, 2012.

[16] A. Bagri, C. Mattevi, M. Acik, Y. J. Chabal, M. Chhowalla and V. B. Shenoy, "Structural evolution during the reduction of chemically derived graphene oxide," *Nat. Chem.,* vol. 2, p. 581–587, 2010.

[17] H.-K. Jeong, Y. P. Lee, M. H. Jin, E. S. Kim, J. J. Bae and Y. H. Lee, "Thermal stability of graphite oxide," *Chem. Phys. Lett.,* vol. 470, p. 255–258, 2009.

[18] K. K. H. De Silva, H.-H. Huang, R. K. Joshi and M. Yoshimura, "Chemical reduction of graphene oxide using green reductants," *Carbon,* vol. 119, p. 190–199, 2017.

[19] B. C. Brodie, "XIII. On the atomic weight of graphite," *Philos. Trans. R. Soc. London,* vol. 149, p. 249–259, 1859.

[20] J. Chen, B. Yao, C. Li and G. Shi, "An improved Hummers method for eco-friendly synthesis of graphene oxide," *Carbon,* vol. 64, p. 225–229, 2013.

[21] M. F. El-Kady and R. B. Kaner, "Scalable fabrication of high-power graphene micro-supercapacitors for flexible and on-chip energy storage," *Nat. Commun.,* vol. 4, p. 1475, 2013.

[22] H. Yang, S. Kannappan, A. S. Pandian, J.-H. Jang, Y. S. Lee and W. Lu, "Nanoporous graphene materials by low-temperature vacuum-assisted thermal process for electrochemical energy storage," *J. Power Sources,* vol. 284, p. 146–153, 2015.

[23] D. R. Rolison and L. F. Nazar, "Electrochemical energy storage to power the 21st century," *MRS Bull.,* vol. 36, p. 486–493, 2011.

[24] Q. Abbas, D. Pajak, E. Frąckowiak and F. Béguin, "Effect of binder on the performance of carbon/carbon symmetric capacitors in salt aqueous electrolyte," *Electrochim. Acta,* vol. 140, p. 132–138, 2014.

[25] J. Chmiola, C. Largeot, P.-L. Taberna, P. Simon and Y. Gogotsi, "Desolvation of Ions in Subnanometer Pores and Its Effect on Capacitance and Double-Layer Theory," *Angew. Chem., Int. Ed.,* vol. 47, p. 3392–3395, 2008.

[26] S. K. Simotwo, C. DelRe and V. Kalra, " Supercapacitor electrodes based on high-purity electrospun,"

*ACS Appl. Mater. Interfaces,* vol. 8 (33), p. 21261–21269, 2016.

[27] D. T. L. Galhena, B. C. Baye, J. C. Meyer, S. Hofmann and G. A. J. Amaratunga, "Reduced Graphene Oxide as a Monolithic Multifunctional Conductive Binder for Activated Carbon Supercapacitors," *ACS Omega,* vol. 3 (8), p. 9246–9255, 2018.

[28] B. Xu, H. Wang, Q. Zhu, N. Sun, B. Anasori, L. Hu, F. Wang, Y. Guan and Y. Gogotsi, "Reduced graphene oxide as a multi-functional conductive binder for supercapacitor electrodes," *Energy Storage Mater.,* vol. 12, p. 128–136, 2018.

[29] J.-H. Choi, C. Lee, S. Cho, G. D. Moon, B.-S. Kim, H. Chang and H. D. Jang, "High capacitance and energy density supercapacitor based on biomass-derived activated carbons with reduced graphene oxide binder," *Carbon,* vol. 132, p. 16–24, 2018.

[30] S. Xu, R. Liu, X. Shi, Y. Ma, M. Hong, X. Chen, T. Wang, F. Li, N. Hu and Z. Yang, "A dual CoNi MOF nanosheet/nanotube assembled on carbon cloth for high performance hybrid supercapacitors," *Electrochim. Acta,* vol. 342, no. 136124, 2020.

[31] S. Xu, C. Su, T. Wang, Y. Ma, J. Hu, J. Hu, N. Hu, Y. Su, Y. Zhang and Z. Yang, "One-step electrodeposition of nickel cobalt sulfide nanosheets on Ni nanowire film for hybrid supercapacitor," *Electrochim. Acta,* vol. 259, p. 617–625, 2018.

[32] W. Raza, F. Ali, N. Raza, Y. Luo, K.-H. Kim, J. Yang, S. Kumar, A. Mehmood and E. E. Kwon, "Recent advancements in supercapacitor technology," *Nano Energy,* vol. 52, p. 441–473, 2018.

[33] I. Hadjipaschalis, A. Poullikkas and V. Efthimiou, "Overview of current and future energy storage technologies for electric power applications," *Renew. Sust. Energ. Rev.,* vol. 13, p. 1513–1522, 2009.

[34] S. M. Halper and J. C. Ellenbogen, "Supercapacitors: A brief overview.," *MITRE,* 2006.

[35] R. Lin, "Formulation of eletrolytes based onionic liquids for supercapacitors applications (Ph.D. thesis)," *University of Toulose,* Toulose, France, 2012.

[36] K. Nomura, H. Nishihara, N. Kobayashi, T. Asada and T. Kyotani, "4.4 V supercapacitors based on super-stable mesoporous carbon sheet made of edge-free graphene walls," *Energy Environ. Sci.,* vol. 12, p. 1542–1549, 2019.

[37] M. Lazzari, Electrode materials for Ionic liquid-based Supercapacitors. Ph. D. Thesis, Bologna: University of Bologna, 2010.

[38] J. W. Long, D. Belanger, T. Brousse, W. Sugimoto, M. B. Sassin and O. Crosnier, "Asymmetric electrochemical capacitors – stretching the limits of aqueous electrolytes," *MRS Bull.,* vol. 36, p. 513, 2011.

[39] K. Naoi and P. Simon, "New Materials and New Configurations for Advanced Electrochemical Capacitors," *J. Electrochem. Soc.,* vol. 17 (1), p. 34–37, 2008.

[40] B. E. Conway, Electrochemical supercapacitors - Scientific Fundamentals and Technological Applications, Ottawa (Canada): Springer Science, 1999.

[41] M. Mastragostino, C. Arbizzani and F. Soavi, “Conducting polymers as electrode materials in supercapacitors,” *Solid State Ion.,* vol. 148, p. 493–494, 2002.

[42] Y. Hou, Y. Cheng, T. Hobson and J. Liu, “Design and Synthesis of Hierarchical MnO2 Nanospheres/Carbon Nanotubes/Conducting Polymer Ternary Composite for High Performance Electrochemical Electrodes,” *Nano Lett.,* vol. 10, p. 2727–2733, 2010.

[43] Maxwell Technologies, “maxwell.com,” 2019. [Online]. Available: https://www.maxwell.com/images/documents/K2_2_7V_3400_ds_3001923_Datasheet.pdf.

[44] P. Kumar, E. D. Mauro, S. Zhang, A. Pezzella, F. Soavi, C. Santato and F. Cicoira, “Melanin-based flexible supercapacitors,” *J. Mater. Chem. C,* vol. 4, p. 9516, 2016.

[45] A. Burke, “R&D considerations for the performance and application of electrochemical capacitors,” *Electrochim. Acta,* vol. 53 (3), p. 1083–1091, 2007.

[46] M. D. Stoller and R. S. Ruoff, “Best practice methods for determining an electrode material's performance for ultracapacitors,” *Energy Environ. Sci.,* vol. 3 (9), p. 1294–1301, 2010.

[47] Z. Lei, L. Liu, H. Zhao, F. Liang, S. Chang, L. Li and Y. Zhang, “Nanoelectrode design from microminiaturized honeycomb monolith with ultrathin and stiff nanoscaffold for high-energy micro-supercapacitors,” *Nat. Commun.,* vol. 11, p. 299, 2020.

[48] V. Khomenko, E. Frackowiak and F. Béguin, “Determination of the specific capacitance of conducting polymer/nanotubes composite electrodes using different cell configurations,” *Electrochim. Acta,* vol. 50 (12), p. 2499–2506, 2005.

[49] X.-Z. Sun, X. Zhang, B. Huang and Y.-W. Ma, “Effects of Separator on the Electrochemical Performance of Electrical Double-Layer Capacitor and Hybrid Battery-Supercapacitor,” *Acta Phys.-Chim. Sin.,* vol. 30 (3), p. 485–491, 2014.

[50] P. Mandake and P. B. Karandika, “Significance of Separator Thickness for Supercapacitor,” *IJRASET,* vol. 4 (2), p. 214–218, 2016.

[51] Maxwell technologies, “maxwell.com,” 2007. [Online]. Available: https://www.maxwell.com/images/documents/applicationnote_1012839_1.pdf.

[52] S. Ratha and A. K. Samantara, Supercapacitor: instrumentation, measurement and performance evaluation techniques, Springer, 2018.

[53] A. Noori, M. F. El-Kady, M. S. Rahmanifar, R. B. Kaner and M. F. Mousavi, “Towards establishing standard performance metrics for batteries, supercapacitors and beyond,” *Chem. Soc. Rev.,* vol. 49, p. 1272, 2019.

[54] E. Frackowiak and F. Beguin, “Carbon materials for the electrochemical storage of energy in capacitors,” *Carbon,* vol. 39, p. 937–950, 2001.

[55] D. Qu and H. Shi, “Studies of activated carbons used in double-layer capacitors,” *J. Power Sources,* vol. 74, p. 99–107, 1998.

[56] K. Kierzek, E. Frackowiak, G. Lota, G. Gryglewicz and J. Machnikowski, “Electrochemical capacitors based on highly porous carbons prepared by KOH activation,” *Electrochim. Acta,* vol. 49, p. 515–523, 2004.

[57] E. Raymundo-Piñero, F. Leroux and F. Béguin, “A High-Performance Carbon for Supercapacitors Obtained by Carbonization of a Seaweed Biopolymer,” *Adv. Mater.,* vol. 18, p. 1877–1882, 2006.

[58] F. Veltri, F. Alessandro, A. Scarcello, A. Beneduci, M. Arias Polanco, D. Cid Perez, C. Vacacela Gomez, A. Tavolaro, G. Giordano and L. Caputi, “Porous Carbon Materials Obtained by the Hydrothermal Carbonization of Orange Juice,” *Nanomaterials,* vol. 10, p. 655, 2020.

[59] K. Koziol, J. Vilatela, A. Moisala, M. Motta, P. Cunniff, M. Sennett and A. Windle, “High-Performance Carbon Nanotube Fiber,” *Science,* vol. 318 (5858), p. 1892–1895, 2007.

[60] C. Xiong, T. Li, T. Zhao, A. Dang, H. Li, X. Ji, W. Jin, S. Jiao, Y. Shang and Y. Zhang, “Reduced graphene oxide-carbon nanotube grown on carbon fiber as binder-free electrode for flexible high-performance fiber supercapacitors,” *Compos. Part B: Eng.,* vol. 116, p. 7–15, 2017.

[61] J.-H. Chen, C. Jang, S. Xiao, M. Ishigami and M. S. Fuhrer, “Intrinsic and extrinsic performance limits of graphene devices on SiO2,” *Nat. Nanotechnol.,* vol. 3, p. 206–209, 2008.

[62] K. S. Novoselov and A. K. Geim, “The Rise of Graphene,” *Nat. Mater.,* vol. 6, p. 183–191, 2007.

[63] C. Liu, Z. Yu, D. Neff, A. Zhamu and B. Z. Jang, “Graphene-Based Supercapacitor with an Ultrahigh Energy Density,” *Nano Lett.,* vol. 10, p. 4863–4868, 2010.

[64] S. R. C. Vivekchand, C. S. Rout, K. S. Subrahmanyam, A. Govindaraj and C. N. R. Rao, “Graphene-based electrochemical supercapacitors,” *J. Chem. Sci.,* vol. 120, p. 9–13, 2008.

[65] M. D. Stoller, S. Park, Y. Zhu, J. An and R. S. Ruoff, “Graphene-based Ultracapacitors,” *Nano Lett.,* vol. 8, p. 3498–3502, 2008.

[66] Y. Wang, Z. Shi, Y. Huang, Y. Ma, C. Wang, M. Chen and Y. Chen, “Supercapacitor Devices Based on Graphene Materials,” *J. Phys. Chem. C,* vol. 113 (30), pp. 13103-13107, 2009.

[67] G. Yu, L. Hu, M. Vosgueritchian, H. Wang, X. Xie, J. R. McDonough, X. Cui, Y. Cui and Z. Bao, “Solution-Processed Graphene/MnO2 Nanostructured Textiles for High- Performance Electrochemical Capacitors,” *Nano Lett.,* vol. 11, p. 2905–2011, 2011.

[68] M. Sarno, E. Ponticorvo and C. Cirillo, “High surface area monodispersed Fe3O4 nanoparticles alone and on physical exfoliated graphite for improved supercapacitors,” *J. Phys. Chem. Solids,* vol. 99, p.

138–147, 2016.

[69] J. Kaur, A. Vergara, M. Rossi, A. M. Gravagnuolo, M. Valadan, F. Corrado, M. Conte, F. Gesuele, P. Giardina and C. Altucci, “Electrostatically driven scalable synthesis of MoS2–graphene hybrid films assisted by hydrophobins,” *RSC Adv.,* vol. 7, p. 50166–50175, 2017.

[70] W. Tian, Q. Gao, L. Zhang, C. Yang, Z. Li, Y. Tan, W. Qian and H. Zhang, “Renewable graphene-like nitrogen-doped carbon nanosheets as supercapacitor electrodes with integrated high energy–power properties,” *J. Mater. Chem. A,* vol. 4, p. 8690–8699, 2016.

[71] M. Carmo, A. R. dos Santos, J. G. R. Poco and M. Linardi, “Physical and electrochemical evaluation of commercial carbon black as electrocatalysts supports for DMFC applications,” *J. Power Sources,* vol. 173 (2), p. 860–866, 2007.

[72] E. Frackowiak, V. Khomenko, K. Jurewicz, K. Lota and F. Béguin, “Supercapacitors based on conducting polymers/nanotubes composites,” *J. Power Sources,* vol. 153 (2), p. 413–418, 2006.

[73] T. C. Girija and M. V. Sangaranarayanan, “Polyaniline-based nickel electrodes for electrochemical supercapacitors—Influence of Triton X-100,” *J. Power Sources,* vol. 159 (2), p. 1519–1526, 2006.

[74] X. Li, L. Yang, Y. Lei, L. Gu and D. Xiao, “Microwave-assisted chemical-vapor-induced in situ polymerization of polyaniline nanofibers on graphite electrode for high performance supercapacitor,” *ACS Appl. Mater. Interfaces,* vol. 6, p. 19978–19989, 2014.

[75] P. Asen and S. Shahrokhian, “A high performance supercapacitor based on graphene/polypyrrole/Cu2O–Cu(OH)2 ternary nanocomposite coated on nickel foam,” *Phys. Chem. C,* vol. 121, p. 6508–6519, 2017.

[76] Y. Wang, G. J., T. Wang, J. Shao, D. Wang and Y.-W. Yang, “Mesoporous transition metal oxides for supercapacitors,” *Nanomaterials,* vol. 5, p. 1667–1689, 2015.

[77] M. Zhi, X. Xiang, J. Li, M. Li and N. Wu, “Nanostructured carbon–metal oxide composite electrodes for supercapacitors: a review,” *Nanoscale,* vol. 5, p. 72–88, 2013.

[78] H. Bai, C. Li and G. Shi, “Functional Composite Materials Based on Chemically Converted Graphene,” *Adv. Mater.,* vol. 23 (9), p. 1089–1115, 2011.

[79] Q. Qu, P. Zhang, B. Wang, Y. Chen, S. Tian, Y. Wu and R. Holze, “Electrochemical Performance of MnO2 Nanorods in Neutral Aqueous Electrolytes as a Cathode for Asymmetric Supercapacitors,” *J. Phys. Chem. C.,* vol. 113, p. 14020–14027, 2009.

[80] Q. T. Qu, Y. Shi, S. Tian, Y. H. Chen, Y. P. Wu and R. Holze, “A new cheap asymmetric aqueous supercapacitor: Activated carbon//NaMnO2,” *J. Power Sources,* vol. 194 (2), p. 1222–1225, 2009.

[81] M. Ue, K. Ida and S. Mori, “Electrochemical Properties of Organic Liquid Electrolytes Based on Quaternary Onium Salts for Electrical Double-Layer Capacitors,” *J. Electrochem. Soc.,* vol. 141, p. 2989, 1994.

[82] E. Brandon, W. Smart and W. West, “Supercapacitor Electrolyte Solvents With Liquid Range below -80 °C,” *Nasa Tech. Briefs,* vol. 34, p. 21–22, 2010.

[83] M. Ue, “Chemical Capacitors and Quaternary Ammonium Salts,” *Electrochemistry,* vol. 75 (8), p. 565–572, 2007.

[84] K. Chiba, T. Ueda, Y. Yamaguchi, Y. Oki, F. Shimodate and K. Naoi, “Electrolyte Systems for High Withstand Voltage and Durability I. Linear Sulfones for Electric Double-Layer Capacitors,” *J. Electrochem. Soc.,* vol. 158, p. A872, 2011.

[85] K. Chiba, T. Ueda, Y. Yamaguchi, Y. Oki, F. Shimodate and K. Naoi, “Electrolyte Systems for High Withstand Voltage and Durability II. Alkylated Cyclic Carbonates for Electric Double-Layer Capacitors,” *J. Electrochem. Soc.,* vol. 158, p. A1320, 2011.

[86] A. Brandt, P. Isken, A. Lex-Balducci and A. Balducci, “Adiponitrile-based electrochemical double layer capacitor,” *J. Power Sources,* vol. 204, p. 213–219, 2012.

[87] S. Zhang, N. Sun, X. He, X. Lu and X. Zhang, “Physical Properties of Ionic Liquids: Database and Evaluation,” *J. Phys. Chem. Ref. Data,* vol. 35 (4), p. 1475, 2006.

[88] C. Arbizzani, M. Biso, D. Cericola, M. Lazzari, F. Soavi and M. Mastragostino, “Safe, high-energy supercapacitors based on solvent-free ionic liquid electrolytes,” *J. Power Sources,* vol. 185 (2), p. 1575–1579, 2008.

[89] A. Balducci, R. Dugas, P. L. Taberna, P. Simon, D. Plée, M. Mastragostino and S. Passerini, “High temperature carbon–carbon supercapacitor using ionic liquid as electrolyte,” *J. Power Sources,* vol. 165 (2), p. 922–927, 2007.

[90] R. Zarrougui, R. Hachicha, R. Rjab and O. Ghodbane, “1-Allyl-3-methylimidazolium-based ionic liquids employed as suitable electrolytes for high energy density supercapacitors based on graphene nanosheets electrodes,” *J. Mol. Liq.,* vol. 249, p. 795–804, 2018.

[91] P. Harrop, “Supercapacitor Markets, Technology Roadmap, Opportunities 2021-2041,” IDTechEx, 2020.

[92] A. Lerf, H. He, M. Forster and J. Klinowski, “Structure of Graphite Oxide Revisited,” *J. Phys. Chem. B,* vol. 102, p. 4477–4482, 1998.

[93] V. Strong, S. Dubin, M. F. El-Kady, A. Lech, Y. Wang, B. H. Weiller and R. B. Kaner, “Patterning and Electronic Tuning of Laser Scribed Graphene for Flexible All-Carbon Devices,” *ACS Nano,* vol. 6, p. 1395–1403, 2012.

[94] Y. Zhu, M. D. D. Stoller, W. Cai, A. Velamakanni, R. D. D. Piner, D. Chen and R. S. Ruoff, “Exfoliation of Graphite Oxide in Propylene Carbonate and Thermal Reduction of the Resulting Graphene Oxide Platelets,” *ACS Nano,* vol. 4, p. 1227–1233, 2010.

[95] R. S. Bhoria, “Enhancing Liquid Phase Exfoliation of Graphene in Organic Solvents with Additives,” in

*Graphene and Its Derivatives - Synthesis and Applications*, IntechOpen, 2019.

[96] R. J. Smith, M. Lotya and J. N. Coleman, "The importance of repulsive potential barriers for the dispersion of graphene using surfactants," *New J. Phys.,* vol. 12, p. 125008–125018, 2010.

[97] S. D. Gupta and S. S. Bhagwat, "Adsorption of Surfactants on Carbon Black-Water Interface," *J. Dispers. Sci. Technol.,* vol. 26 (1), p. 111–120, 2005.

[98] K. R. Paton and al., "Scalable production of large quantities of defect-free few-layer graphene by shear exfoliation in liquids," *Nat. Mater.,* vol. 13, p. 624–630, 2014.

[99] C. Gomez-Navarro, R. T. Weitz, A. M. Bittner, M. Scolari, A. Mews, M. Burghard and K. Kern, "Electronic Transport Properties of Individual Chemically Reduced Graphene Oxide Sheets," *Nano Lett.,* vol. 7 (11), p. 3499–3503, 2007.

[100] W. S. Hummers Jr. and R. E. Offeman, "Preparation of Graphitic Oxide," *J. Am. Chem. Soc.,* vol. 80 (6), p. 1339, 1958.

[101] N. I. Kovtyukhova, P. J. Ollivier, B. Martin, T. E. Mallouk, S. A. Chizhik, E. V. Buzaneva and A. D. Gorchinskiy, "Layer-by-Layer assembly of ultrathin composite films from micron-sized graphite oxide sheets and polycations," *Chem. Mater.,* vol. 11, p. 771–778, 1999.

[102] D. C. Marcano, D. V. Kosynkin, J. M. Berlin, A. Sinitskii, Z. Sun, A. Slesarev, L. B. Alemany, L. W. and J. M. Tour, "Improved Synthesis of Graphene Oxide," *ACS Nano,* vol. 4 (8), p. 4806–4814, 2010.

[103] L. Liu, Z. Shen, M. Yi, X. Zhanga and S. Ma, "A green, rapid and size-controlled production of high-quality graphene sheets by hydrodynamic forces," *RSC Adv.,* vol. 4, p. 36464–36470, 2014.

[104] Y.-P. Lin, "Functionalization of two-dimensional nanomaterials based on graphene. Condensed Matter," *Aix Marseille Université,* 2014.

[105] P. V. Kumar, N. M. Bardhan, G.-Y.-. Chen, Z. Li, A. M. Belcher and J. C. Grossman, "New insights into the thermal reduction of graphene oxide: Impact of oxygen clustering," *Carbon,* vol. 100, p. 90–98, 2016.

[106] E. J.-C. Amieva, J. López-Barroso, A. L. Martínez-Hernández and C. Velasco-Santos, "Graphene-Based Materials Functionalization with Natural Polymeric Biomolecules," in *Recent Advances in Graphene Research*, IntechOpen, 2016.

[107] Z. Li, S. Gadipelli, H. Li, C. A. Howard, D. J. L. Brett, P. R. Shearing, Z. Guo, I. P. Parkin and F. Li, "Tuning the interlayer spacing of graphene laminate films for efficient pore utilization towards compact capacitive energy storage," *Nat. Energy,* vol. 5, p. 160–168, 2020.

[108] H. C. Schniepp, J.-L. Li, M. J. McAllister, H. Sai, M. Herrera-Alonso, D. H. Adamson, R. K. Prud'homme, R. Car, D. A. Saville and I. A. Aksay, "Functionalized Single Graphene Sheets Derived from Splitting Graphite Oxide," *J. Phys. Chem. B.,* vol. 110 (17), p. 8535–8539, 2006.

[109] C. K. Chua and M. Pumera, “Chemical reduction of graphene oxide: a synthetic chemistry viewpoint,” *Chem. Soc. Rev.,* vol. 43, p. 291–312, 2014.

[110] S. Pei, J. Zhao, J. Du, W. Ren and H.-M. Cheng, “Direct reduction of graphene oxide films into highly conductive and flexible graphene films by hydrohalic acids,” *Carbon,* vol. 48 (15), p. 4466–4474, 2010.

[111] I. Jung, D. A. Field, N. J. Clark, Y. Zhu, D. Yang, R. D. Piner, S. Stankovich, D. A. Dikin, H. Geisler, C. A. Ventrice and R. S. J. Ruoff, “Reduction Kinetics of Graphene Oxide Determined by Electrical Transport Measurements and Temperature Programmed Desorption,” *J. Phys. Chem. C,* vol. 113 (43), p. 18480–18486, 2009.

[112] J. Borysiuk, J. Sołtys, J. Piechota, S. Krukowski, J. M. Baranowski and R. Stępniewski, “Structural defects in epitaxial graphene layers synthesized on C-terminated 4H-SiC (0001) surface— Transmission electron microscopy and density functional theory studies,” *J. Appl. Phys.,* vol. 115 (5), no. 054310, 2014.

[113] J. Theerthagiri, R. Sudha, K. Premnath, P. Arunachalam, J. Madhavan and A. M. Al-Mayouf, “Growth of iron diselenide nanorods on graphene oxide nanosheets as advanced electrocatalyst for hydrogen evolution reaction,” *Int. J. Hydrog. Energy,* vol. 42 (18), p. 13020–13030, 2017.

[114] A. H. Wazir and I. W. Kundi, “Synthesis of Graphene Nano Sheets by the Rapid Reduction of Electrochemically Exfoliated Graphene Oxide Induced by Microwaves,” *J. Chem. Soc. Pak.,* vol. 38 (1), p. 11–16, 2016.

[115] A. D. McNaught and A. Wilkinson, Compendium of Chemical Terminology, 2nd ed. (the "Gold Book"), Oxford: IUPAC, 1997.

[116] W. H. Bragg and W. L. Bragg, “The reflection of X-rays by crystals,” *Proc. R. Soc. London,* vol. 88, p. 246–248, 1913.

[117] P. Scherrer, “Bestimmung der Größe und der inneren Struktur von Kolloidteilchen mittels Röntgenstrahlen,” in *Kolloidchemie Ein Lehrbuch*, Berlin, Springer, 1912, p. 387−409.

[118] N. S. Saenko, “The X-ray diffraction study of three-dimensional disordered network of nanographites: Experiment and theory,” *Phys. Procedia,* vol. 23, p. 102–105, 2012.

[119] S. Drewniak, R. Muzyka, A. Stolarczyk, T. Pustelny, M. Kotyczka-Morańska and M. Setkiewicz, “Studies of Reduced Graphene Oxide and Graphite Oxide in the Aspect of Their Possible Application in Gas Sensors,” *Sensors,* vol. 16, p. 103–118, 2016.

[120] H. Saleem, M. Haneef and H. Y. Abbasi, “Synthesis route of reduced graphene oxide via thermal reduction of chemically exfoliated graphene oxide,” *Mater. Chem. Phys.,* vol. 204, p. 1–7, 2018.

[121] K. Bustos-Ramírez, C. E. Barrera-Díaz, M. De Icaza-Herrera, A. L. Martínez-Hernández, R. Natividad-Rangel and C. Velasco-Santos, “4-chlorophenol removal from water using graphite and graphene oxides as photocatalysts,” *J. Environ. Health Sci. Engineer.,* vol. 13, p. 33–42, 2015.

[122] K. Krishnamoorthy, M. Veerapandian, K. Yun and S.-J. Kim, “The chemical and structural analysis of graphene oxide with different degrees of oxidation,” *Carbon,* vol. 53, p. 38–49, 2013.

[123] H. Yang, H. Hu, Y. Wang and T. Yu, “Rapid and non-destructive identification of graphene oxide thickness using white light contrast spectroscopy,” *Carbon,* vol. 52, p. 528–534, 2013.

[124] G. T. S. How, A. Pandikumar, H. N. Ming and L. H. Ngee, “Highly exposed {001} facets of titanium dioxide modified with reduced graphene oxide for dopamine sensing,” *Sci. Rep.,* vol. 4, no. 5044, 2014.

[125] J.-B. Wu, M.-L. Lin, X. Cong, H.-N. Liu and P.-H. Tan, “Raman spectroscopy of graphene-based materials and its applications in related devices,” *Chem. Soc. Rev.,* vol. 47, p. 1822–1873, 2018.

[126] H. Wang, Y. Wang, X. Cao, M. Fenga and G. Lana, “Vibrational properties of graphene and graphene layers,” *J. Raman Spectrosc.,* vol. 40, p. 1791–1796, 2009.

[127] A. Gupta, G. Chen, P. Joshi, S. Tadigadapa and P. C. Eklund, “Raman Scattering from High-Frequency Phonons in Supported n-Graphene Layer Films,” *Nano Lett.,* vol. 6 (12), p. 2667–2673, 2006.

[128] “Wikipedia.org,” 2012 February 1. [Online]. Available: http://en.wikipedia.org/wiki/File:Zeta_Potential_for_a_particle_in_dispersion_medium.png.

[129] D. C. Henry, “The cataphoresis of suspended particles. Part I. – The equation of cataphoresis,” *Proc. R. Soc. A,* vol. 133, p. 106–129, 1931.

[130] A. V. Delgado, F. González-Caballero, R. J. Hunter, L. K. Koopal and J. Lyklema, “Measurement and interpretation of electrokinetic phenomena,” *J. Colloid Interface Sci.,* vol. 309 (2), p. 194–224, 2007.

[131] A. Kumar and C. K. Dixit, “Methods for characterization of nanoparticles,” in *Advances in Nanomedicine for the Delivery of Therapeutic Nucleic Acids*, Duxford (UK), Woodhead Publishing (Elsevier), 2017, p. 43–58.

[132] J. M. Thwala, M. Li, M. C. Y. Wong, S. Kang, E. M. V. Hoek and B. B. Mamba, “Bacteria-polymeric membrane interactions: atomic force microscopy and XDLVO predictions,” *Langmuir,* vol. 29, p. 13773–13782, 2013.

[133] L. J. F. Klukova, S. Belicky, A. Vikartovska and J. Tkac, “Graphene oxide-based electrochemical label-free detection of glycoproteins down to aM level using a lectin biosensor,” *Analyst,* vol. 141, p. 4278–4282, 2016.

[134] R. Rapisarda and M. Meo, “Multifunctional reduced graphene oxide coating on laminated composites,” *Mater. Today: Proc.,* no. DOI: 10.1016/j.matpr.2020.01.612, 2020.

[135] I. C. B. A., “Carbon Black User’s Guide: Safety, Health & Environmental Information,” *International carbon black association,* 2016.

[136] D. Weingarth, R. Drumm, A. Foelske-Schmitz, R. Kötz and V. Presser, “An electrochemical in situ study

of freezing and thawing of ionic liquids in carbon nanopores," *Phys. Chem. Chem. Phys.,* vol. 16, p. 21219−21224, 2014.

[137] C. M. González-García, M. L. González-Martín, V. Gómez-Serrano, J. M. Bruque and L. Labajos-Broncano, "Determination of the Free Energy of Adsorption on Carbon Blacks of a Nonionic Surfactant from Aqueous Solutions," *Langmuir,* vol. 16, p. 3950–3956, 2000.

[138] J. I. Paredes, S. Villar-Rodil, A. Martínez-Alonso and J. M. D. Tascón, "Graphene Oxide Dispersions in Organic Solvents," *Langmuir,* vol. 24, p. 10560–10564, 2008.

[139] K. Mitsuda, H. Kimura and T. Murahashi, "Evaporation and decomposition of Triton X-100 under various gases and temperatures," *J. Mater. Sci.,* vol. 24, p. 413–419, 1989.

[140] M. A. Pimenta, G. Dresselhaus, M. S. Dresselhaus, L. G. Cançado, A. Jorio and R. Saito, "Studying disorder in graphite-based systems by Raman spectroscopy," *Phys. Chem. Chem. Phys.,* vol. 9, p. 1276–1290, 2007.

[141] A. C. Ferrari, "Raman spectroscopy of graphene and graphite: Disorder, electron−phonon coupling, doping and nonadiabatic effects," *Solid State Commun.,* vol. 143, p. 47–57, 2007.

[142] A. C. Ferrari, J. C. Meyer, V. Scardaci, C. Casiraghi, M. Lazzeri, F. Mauri, S. Piscanec, D. Jiang, K. S. Novoselov, S. Roth and A. K. Geim, "Raman Spectrum of Graphene and Graphene Layers," *Phys. Rev. Lett.,* vol. 97, no. 187401, 2006.

[143] N. Krishnankutty and M. A. Vannice, "Effect of Pretreatment on Surface Area, Porosity, and Adsorption Properties of a Carbon Black," *Chem. Mater.,* vol. 7, p. 754–763, 1995.

[144] J. Biscoe and B. E. Warren, "An X-Ray Study of Carbon Black," *J. Appl. Phys.,* vol. 13, p. 364–371, 1942.

[145] A. K. M. Mydul Islam, J.-I. Hwang, S.-E. Lee and J.-E. Kim, "Comparative study of carbon black and activated carbon adsorbents for removal of carbofuran from aqueous solution," *Desalin. Water Treat.,* vol. 57, p. 21512–21523, 2016.

[146] S. Shiraishi, "Highly-Durable Carbon Electrode for Electro-chemical Capacitors," *Boletín del Grupo Español del Carbón,* vol. 28, p. 18–24, 2013.

[147] L. Xia, L. Yu, D. Hu and G. Z. Chen, "Electrolytes for electrochemical energy storage," *Mater. Chem. Front.,* vol. 1, p. 584–618, 2017.

[148] ASTM International, "Standard Terminology Relating to Carbon Black," *www.astm.org,* no. D3053-20a, 2020.

[149] Z. Ge and Y. Wang, "Estimation of Nanodiamond Surface Charge Density from Zeta Potential and Molecular Dynamics Simulations," *J. Phys. Chem. B,* vol. 121, p. 3394–3402, 2017.

[150] A. J. Bard and L. R. Faulkner, Eelctrochemical Methods - Fundamentals and applications, Austin (Texas, USA): John Wiley & Sons, Inc., 2001.

[151] D. Gatti, “Potential Stationary Energy Storage Technologies to Monitor,” IDTechEx, 2020.